UNDERSTANDING VISUAL APPEARANCE ON THE WEB USING LARGE-SCALE CROWDSOURCING AND DEEP LEARNING

A Dissertation

Presented to the Faculty of the Graduate School

of Cornell University

in Partial Fulfillment of the Requirements for the Degree of

Doctor of Philosophy

by

Sean Cameron Bell

August 2016

© 2016 Sean Cameron Bell

ALL RIGHTS RESERVED

UNDERSTANDING VISUAL APPEARANCE ON THE WEB USING LARGE-SCALE CROWDSOURCING AND DEEP LEARNING

Sean Cameron Bell, Ph.D.

Cornell University 2016

Automatically understanding scenes is the holy grail of computer vision. Real-world scenes have a vast array of interesting objects, materials, textures, and surfaces. With scenes, people want to edit photographs, search by object and material properties, visualize changes to rooms and buildings, browse collections by visual similarity, and explain images to the visually impaired. However, the tools and data that we have for recognizing, editing, and exploring the application of scene properties for everyday problems are still quite limited. We cannot easily understand, search, and aggregate visual concepts in the billions of photos that are uploaded every day to the web.

Recently, large data collections combined with machine learning have opened new frontiers in scene understanding. In this thesis, we introduce new large-scale crowdsourced datasets for material and visual understanding in the wild. Using these new datasets, we develop new state-of-the-art algorithms for scene understanding of materials, objects, shapes, and style.

We propose multiple new large-scale, first-of-their-kind datasets in the wild. OpenSurfaces contains thousands of segmented surfaces annotated with material, texture, and contextual information. MINC (Materials in Context) includes millions of points annotated with materials. Both are at least an order of magnitude larger than prior datasets. The Intrinsic Images in the Wild (IIW) dataset includes millions of crowdsourced annotations of relative comparisons of ma-

terial properties at pairs of points in each scene. These datasets all require careful crowdsourcing and use the ability of humans to judge materials despite variations in illumination, viewpoint, imaging conditions, and context.

Using these large-scale datasets we demonstrate state-of-the-art algorithms for material recognition using OpenSurfaces and MINC, and intrinsic image decomposition using IIW. We also develop state-of-the-art algorithms for object detection (Inside-Outside Network, ION) and visual search for style similarity (ProductNet).

In this thesis we have demonstrated how the combination of crowdsourcing at scale and new deep learning architectures can create new tools to let consumers understand and edit images, scenes, materials and objects.

BIOGRAPHICAL SKETCH

Sean Bell was born in Toronto, Canada. When first asked "what do you want to be when you grow up?", he would answer "computer programmer!", not even knowing what they did—he just loved computers. In early high school, he would spend his spare time in the computer lab, working on making graphical effects and animations with Java Applets. From 2007 to 2011, he studied Engineering Science at the University of Toronto. In his second year, his team won first place in the AER201 Engineering Design Project, programming the micro-controller for a robot that dispenses an exact number of candies at high speed (a very useful device). In his last year, he built a ray-tracer that "borrowed" unused computers across campus to render his scenes, one scanline at a time.

During his undergrad, Sean spent five summers working at Hill & Schumacher, a patent law firm, and almost went into patent law as a possible career. However, he was more interested in writing software to help draft patents than the patents themselves. This turned into his undergraduate thesis, which was a real-time system to detect inconsistencies in patents as they were being drafted.

Since 2011, Sean has been studying for his doctorate degree in Computer Science at Cornell University. When he first arrived, he wasn't sure whether to work on natural language processing, computer graphics, or machine learning. He quickly found his place in the boundary between graphics and vision, and has since enjoyed five wonderful years studying at Cornell. Upon graduation in 2016, he is co-founding a deep learning company, GrokStyle, based on his work in visual search and style similarity.

This thesis is dedicated to my parents, for their love and support,
and to Stephanie Sang, for putting up with so much.

ACKNOWLEDGEMENTS

This thesis would not have been possible without the support, guidance, and mentorship of my advisor Prof. Kavita Bala. Kavita has always encouraged me to strive for the best possible version of anything that I work on, and has been central to learning how to do research. I would like to thank Prof. Noah Snavely, as my close collaborator and committee member; his ideas and feedback have been invaluable to research meetings. I would also like to thank collaborators Paul Upchurch, Larry Zitnick, and Ross Girshick, and my other PhD committee member, Prof. Charles Van Loan, as well as Profs. David Bindel and Serge Belongie for serving as proxies on my committee.

I thank my friends and colleagues in the Graphics and Vision Lab, for their camaraderie, willingness to discuss research ideas and read paper drafts, and for making it such a great place to work: Kevin Matzen, Tim Langlois, Balázs Kovács, and Paul Upchurch, as well as Albert Liu, Pramook Khungurn, Daniel Hauagge, Kyle Wilson, Nicolas Savva, Scott Wehrwein, Eston Schweikart, Jui-hsien Wang, Wenzel Jakob, and Steven An. I would also like to thank computer graphics professors Steve Marschner and Doug James, as well as the entire Cornell Computer Science department, for always attending my talks with great feedback.

At the University of Toronto, I would like to thank my colleagues and friends for making undergrad so enjoyable, and for cultivating friendly competition: Trevor Campbell, Konstantine Tsotsos, Jamie Liu, Rick Zhang, Manan Arya, Sanae Rosen, Catherine Chen, Amy Chen, Angela Yoo, Zoya Gavrilov, Mark Harfouche, Adam Pan, and Casey Scott-Songin. I thank Prof. Kyros Kutulakos for inspiring me to consider research in computer graphics.

I would like to thank the collaborators and colleagues that I meet at conferences and internships, all those who attended my talks and posters, and those who emailed me about my work, with exciting ideas, questions, and discussions about research, in particular Abhinav Shrivastava, Ishan Misra, Jon Barron, Andrej Karpathy, Peter Gehler.

I owe everything to my family, including my grandparents, cousins, aunts, uncles, my siblings Ian and Robyn, and especially my parents Sally and Graydon, for creating such a wonderful and supportive environment, helping me at every stage in life, and for putting up with me being away for so long. I am grateful to my grandpa Scotty Bell for funding my undergraduate education.

To my girlfriend Stephanie Sang, who supported me through the crunch times, kept me company, listened to my research struggles, sent me hand-drawn comics, brought me home-cooked meals to the lab, and helped give my life meaning outside the lab. You put up with so much, and I am eternally grateful.

Finally, I would like to thank the Zabs sandwich from Collegetown Bagels, and the latte from Gimme Coffee, for being so delicious.

TABLE OF CONTENTS

Biographical Sketch . . . iii
Dedication . . . iv
Acknowledgements . . . v
Table of Contents . . . vii
List of Tables . . . x
List of Figures . . . xiii

1 Introduction **1**

2 OpenSurfaces: A Richly Annotated Catalog of Surface Appearance **7**
2.1 Introduction . . . 7
2.2 Related work . . . 10
2.3 Overview . . . 12
2.3.1 Community photo collections . . . 13
2.3.2 Human annotation . . . 13
2.3.3 OpenSurfaces data representation . . . 15
2.3.4 Annotation stages . . . 16
2.4 The OpenSurfaces annotation pipeline . . . 17
2.4.1 Stage 1: Filtering images by scene category . . . 18
2.4.2 Stage 2: Flag images with improper white balance . . . 19
2.4.3 Stage 3: Material segmentation . . . 20
2.4.4 Stages 4 and 5: Naming materials and objects . . . 23
2.4.5 Stage 6: Planarity voting . . . 24
2.4.6 Stage 7: Rectified textures . . . 25
2.4.7 Stage 8: Appearance matching . . . 26
2.5 Results . . . 30
2.5.1 OpenSurfaces statistics . . . 30
2.5.2 Task analytics . . . 34
2.6 Proof-of-Concept Applications . . . 37
2.6.1 Texturing . . . 37
2.6.2 Informed scene similarity . . . 38
2.6.3 Future applications . . . 38
2.7 Conclusions and future work . . . 40
2.8 Impact . . . 41

3 Material Recognition in the Wild with the Materials in Context Database **47**
3.1 Introduction . . . 47
3.2 Prior Work . . . 50
3.3 The **Materials in Context Database** (MINC) . . . 52
3.3.1 Sources of data . . . 53
3.3.2 Segments, Clicks, and Patches . . . 54

3.4 Material recognition in real-world images . . . 58
3.4.1 Training procedure . . . 58
3.4.2 Full scene material classification . . . 59
3.5 Experiments and Results . . . 61
3.5.1 Patch material classification . . . 61
3.5.2 Full scene material segmentation . . . 64
3.5.3 Comparing MINC to FMD . . . 67
3.5.4 Comparing CNNs with prior methods . . . 68
3.6 Conclusion . . . 69
3.7 Impact . . . 70

4 Intrinsic Images in the Wild 71
4.1 Introduction . . . 71
4.2 Related work . . . 74
4.3 Database . . . 76
4.3.1 What judgements should we collect? . . . 76
4.3.2 Which images and which pairs of points? . . . 78
4.3.3 Annotation interface . . . 81
4.3.4 Data verification . . . 83
4.3.5 Error metric: WHDR . . . 86
4.3.6 Discussion and results . . . 87
4.4 Intrinsic Images Algorithm . . . 89
4.4.1 Initialization . . . 92
4.4.2 Stage 1: Optimize reflectance . . . 93
4.4.3 Stage 2: Optimize for shading . . . 99
4.5 Results . . . 102
4.5.1 Training . . . 102
4.5.2 Ranking . . . 103
4.5.3 MIT Intrinsic Images dataset . . . 108
4.6 Limitations and future work . . . 108
4.7 Conclusion . . . 110
4.8 Impact . . . 111

5 Inside-Outside Net: Detecting Objects in Context with Skip Pooling and Recurrent Neural Networks 112
5.1 Introduction . . . 112
5.2 Prior work . . . 115
5.3 Architecture: Inside-Outside Net (ION) . . . 117
5.3.1 Pooling from multiple layers . . . 118
5.3.2 Context features with IRNNs . . . 119
5.4 Results . . . 122
5.4.1 Experimental setup . . . 122
5.4.2 PASCAL VOC 2007 . . . 127
5.4.3 PASCAL VOC 2012 . . . 128

5.4.4 MS COCO . . . 129
5.4.5 Improvement for small objects . . . 130
5.5 Design evaluation . . . 131
5.5.1 Pool from which layers? . . . 131
5.5.2 How should we normalize feature amplitude? . . . 132
5.5.3 How much does segmentation loss help? . . . 133
5.5.4 How should we incorporate context? . . . 134
5.5.5 Which IRNN architecture? . . . 135
5.5.6 Other variations . . . 136
5.6 Conclusion . . . 137
5.7 Impact . . . 137

6 Learning visual similarity for product design with convolutional neural networks 138
6.1 Introduction . . . 138
6.2 Related Work . . . 141
6.3 Background: learning a distance metric with siamese networks . 144
6.4 Our approach . . . 146
6.5 Learning our visual similarity metric . . . 147
6.5.1 Collecting Training Data . . . 147
6.5.2 Learning a distance metric . . . 152
6.6 Results and applications . . . 156
6.6.1 Visual search . . . 158
6.6.2 Evaluating the metric . . . 159
6.6.3 Discussion, limitations, and future work . . . 164
6.7 Conclusion . . . 166
6.8 Impact . . . 166

7 Conclusion 168
7.1 Impact . . . 168
7.2 Future work . . . 170

Bibliography 171

LIST OF TABLES

2.1 *Summary statistics.* For each task we present: the average cost per item in USD (includes MTurk commission), the average time, the number of items assigned to labelers (**N in**). For naming tasks, **N out** is the number of shapes that had at least 3/5 agreement. For voting and quality tasks, **N out** is the number of items classified as "good" as a result of performing that task. As discussed in Section 2.4.3, we stopped measuring segmentation quality after limiting to the 26 best workers. 33

3.1 **MINC patch counts by category.** Patches were created from both OpenSurfaces segments and our newly collected *clicks*. See Section 3.3.2 for details. 57

3.2 **Patch material classification results.** Mean class accuracy for different CNNs trained on MINC. See Section 3.5.1. 61

3.3 **Patch test accuracy by category.** CNN: GoogLeNet. See the supplemental material (http://www.cs.cornell.edu/\protect\unhbox\voidb@x\penalty\@M\{}sbell/pdf/cvpr2015-minc-supp.pdf) for a full confusion matrix. 62

3.4 **Full scene material classification results.** Mean class and total accuracy on the test set. When training, we optimize the CRF parameters for mean class accuracy, but report both mean class and total accuracy (mean accuracy across all examples). In one experiment **(a)**, we train and test only on segments; in a separate experiment **(b)**, we train and test only on clicks. Accuracies for segments are averaged across all pixels that fall in that segment. 66

3.5 **Cross-dataset experiments.** We train on one dataset and test on another dataset. Since MINC contains 23 categories, we limit MINC to the 10 categories in common. CNN: AlexNet. 68

3.6 **FMD experiments.** By replacing DeCAF features with oversampled AlexNet features we improve on the best FMD result. . . . 68

4.1 *Algorithm variants.* To illustrate the effect of each term, we take the parameter settings found from training and remove different terms. The WHDR errors for each variant increase from left to right, and are listed in Table 4.2. Top left: input and judgements. Other 6: columns: reflectance (top) and shading (bottom) for each variant. 100

4.2 To justify our design choices, we show that many variants produce higher error. Variants (a) through (f) are shown in Table 4.1. The variants are described in more detail in the supplemental (http://www.cs.cornell.edu/\protect\unhbox\voidb@x\penalty\@M\{}sbell/pdf/siggraph2014-intrinsic.pdf). 103

4.3 Visual comparison of our algorithm against several recent open-source algorithms. Each algorithm uses the best parameters found from training (i.e., minimizes mean $\text{WHDR}_{10\%}$ across all photos). Top left: input and judgements. Other 6: columns: reflectance (top) and shading (bottom) for each algorithm. 104

5.1 **Detection results on VOC 2007 test.** Legend: **07+12:** 07 trainval + 12 trainval, **07+12+S:** 07+12 plus SBD segmentation labels [72], **R:** include 2x stacked 4-dir IRNN (context features), **W:** two rounds of box regression and weighted voting [60], **D:** remove all dropout, **SS:** SelectiveSearch [177], **EB:** EdgeBoxes [205], **RPN:** region proposal net. [146], **Time:** per image, excluding proposal generation. 123

5.2 **Detection results on VOC 2012 test.** Legend: **07+12:** 07 trainval + 12 trainval, **07++12:** 07 trainvaltest + 12 trainval, **07+12+S:** 07+12 plus SBD segmentation labels [72], **R:** include 2x stacked 4-dir IRNN (context features), **W:** two rounds of bounding box regression and weighted voting [60], **D:** remove all dropout, **SS:** SelectiveSearch [177], **EB:** EdgeBoxes [205], **RPN:** region proposal network [146]. 124

5.3 **Detection results on COCO 2015 test-dev.** Legend: **R:** include 2x stacked 4-dir IRNN (context features), **W:** two rounds of bounding box regression and weighted voting [60], **D:** remove all dropout, **+S:** train with segmentation labels, **SS:** SelectiveSearch [177], **MCG:** MCG proposals [138], **RPN:** region proposal net [146]. †Our submission to the 2015 MS COCO Detection Competition, and post-competition improvements, described in the Supplemental (`http://www.cs.cornell.edu/\protect\unhbox\voidb@x\penalty\@M\{}sbell/`). *These scores are higher than [65] due to our improved hyperparameters. 125

5.4 **Combining features from different layers.** Metric: Detection mAP on VOC07 test. Training set: 07 trainval + 12 trainval. **1x1**: combine features from different layers using a 1x1 convolution. **L2+Scale+1x1**: use L2 normalization, scaling (initialized to 1000), and 1x1 convolution, as described in section 5.3.1. These results do not include "context features." *This entry is the same as Fast R-CNN [65], but trained with our hyperparameters. 131

5.5 **Approaches to normalizing feature amplitude.** Metric: VOC07 test mAP. All items regularized with segmentation labels. 132

5.6 **Effect of segmentation loss.** Metric: detection mAP on VOC07 test. Adding segmentation loss tends to improve detection performance by about 1 mAP, with no test-time penalty. 133

5.7 **Comparing approaches to adding context.** All rows also pool out of conv3, conv4, and conv5. Metric: detection mAP on VOC07 test. **Seg:** if checked, the top layer received extra supervision from semantic segmentation labels. 134
5.8 **Varying the hidden transition.** We vary the number of units and try either learning recurrent transition $\mathbf{W}_{hh}$ initialized to the identity, or entirely removing it (same as setting $\mathbf{W}_{hh} = I$). 136
5.9 **Other variations.** Metric: VOC07 test mAP. We list some other variations that all perform about the same. 137

6.1 *Product search: uncurated random queries from the test set*. For each query I_q, we show the top 3 retrievals using our method as well as the tagged canonical image I_p from Houzz.com. Object categories are not known at test time. Note that sometimes the retrieved results are closer to the query than I_p. 157
6.2 *Style search: example cross-category queries.* For each object category ("armchairs", "rugs", etc.), we show the closest product of that category to the input I_q, even though the input (usually) does not belong to that category. We show this for 12 different object categories. Note that object category is not used to compute the descriptor x_q; it is only used at retrieval time to filter the set of products. 161

LIST OF FIGURES

2.1 We present OpenSurfaces, a large database of annotated surfaces created from real-world consumer photographs. Our annotation pipeline draws on crowdsourcing to segment surfaces from photos, and then annotates them with rich surface appearance properties, including material, texture, and contextual information. 8

2.2 OpenSurfaces annotation pipeline. Each stage contains a typical example. 17

2.3 (a) Stage 7: Rectifying planar textures interface. This figure shows a successfully completed task, where the perspective grid on the left appears to lie flat against the surface, and the texture, shown on the right, is correctly rectified. (b) Stage 8: Interface for appearance matching to recover material parameters. 43

2.4 Example segmented surfaces labeled "wood" (top row) and "carpet" (bottom row). Each item shows the number of vertices and the time spent. 43

2.5 Statistics over shapes in our database. Left: Histogram of vertex counts, Center: Histogram of CUBAM scores from voting on shape quality, Right: Average CUBAM score for each vertex count. 44

2.6 *Example rectified textures.* Left: original photographs with segmented surface highlighted and user-specified surface normal. Right: rectified texture with provided surface normal. 44

2.7 *Example rectified textures.* Each row: textures rectified using normals from our database, sorted by decreasing vertex count. Each row contains a single type of material: wood, tile, marble, and granite. 44

2.8 *Example reflectance parameters.* First and third rows: material segmentations from our database. Second and fourth rows: blobs rendered with user-specified perceptual Ward parameters. . . . 45

2.9 *Example reflectance parameters.* Left: original photograph. Center: region to be annotated. Right: blob rendered with the user-specified perceptual Ward parameters. 45

2.10 *Better exemplars for texture synthesis.* (a) Synthesis using an unrectified exemplar, showing artifacts of foreshortening. (b) A texture synthesized from a rectified exemplar from our database. 45

2.11 *Retexturing example.* The input target is a segmented photo. A rectified granite countertop surface from OpenSurfaces is synthesized and applied to the input using the correct perspective. . . . 46

2.12 *Informed scene similarity.* Left: query object. Right: photos containing objects of the same name and material, sorted by diffuse color similarity to the query object. 46

3.1 **Overview. (a)** We construct a new dataset by combining OpenSurfaces [12] with a novel three-stage Amazon Mechanical Turk (AMT) pipeline. **(b)** We train various CNNs on patches from MINC to predict material labels. **(c)** We transfer the weights to a fully convolutional CNN to efficiently generate a probability map across the image; we then use a fully connected CRF to predict the material at every pixel. 48
3.2 Example patches from all 23 categories of the **Materials in Context Database** (MINC). Note that we sample patches so that the patch center is the material in question (and not necessarily the entire patch). See Table 3.1 for the size of each category. 50
3.3 **AMT pipeline schematic for collecting clicks. (a)** Workers filter by images that contain a certain material, **(b)** workers click on materials, and **(c)** workers validate click locations by re-labeling each point. Example responses are shown in orange. 55
3.4 **Pipeline for full scene material classification.** An image **(a)** is resized to multiple scales $[1/\sqrt{2}, 1, \sqrt{2}]$. The same sliding CNN predicts a probability map **(b)** across the image for each scale; the results are upsampled and averaged. A fully connected CRF predicts a final label for each pixel **(c)**. This example shows predictions from a single GoogLeNet converted into a sliding CNN (no average pooling). 57
3.5 **Varying patch scale**. We train/test patches of different scales (the patch locations do not vary). The optimum is a trade-off between context and spatial resolution. CNN: AlexNet. 61
3.6 **Varying database size.** Patch accuracy when trained on random subsets of MINC. *Equal size* is using equal samples per category (size determined by smallest category). CNN: AlexNet. 63
3.7 **Accuracy vs patch scale by category**. Dots: peak accuracy for each category; colored lines: *sky*, *wallpaper*, *mirror*; gray lines: other categories. CNN: AlexNet. While most materials are optimally recognized at 23.3% or 32% patch scale, recognition of *sky*, *wallpaper* and *mirror* improve with increasing context. 63
3.8 **Full-scene material classification examples:** high-accuracy test set predictions by our method. CNN: GoogLeNet (with the average pooling layer removed). Right: legend for material colors. See Table 3.4 for quantitative evaluation. 64
3.9 **Optimizing for click accuracy leads to sloppy boundaries.** In **(a)**, we optimize for mean class accuracy across segments, resulting in high quality boundaries. In **(b)**, we optimize for mean class accuracy at click locations. Since the clicks are not necessarily close to object boundaries, there is no penalty for sloppy boundaries. CNN: GoogLeNet (without average pooling). . . . 65

3.10 **High confidence predictions.** Top two rows: correct predictions. Bottom row: incorrect predictions (**T**: true, **P**: predicted). Percentages indicate confidence (the predictions shown are at least this confident). CNN: GoogLeNet. 67

4.1 We introduce a public dataset of indoor scenes for intrinsic images in the wild (a). (b) Our crowdsourcing pipeline lets users annotate pairs of points in each image with relative reflectance judgements. (c) Our intrinsic image decomposition algorithm performs well in respecting the human judgements and is based on a fully-connected conditional random field (CRF) that incorporates long-range interactions in the reflectance layer while simultaneously maintaining local detail. All source images are licensed under Creative Commons (©). 71

4.2 *Our data collection pipeline.* (a) We sample points and edges from over 5,000 photographs, (b) workers flag points on mirrors and transparent surfaces, (c) users judge pairs of points and indicate which point has a darker surface reflectance (or if they are equal), and (d) we aggregate judgements from 5 users for each pair of points (each edge is styled according to the aggregate results, as described in Figure 4.3). 77

4.3 *Aggregated human judgements for an example scene.* The edges connecting points indicate the aggregated reflectance judgement comparing the two points. We sample points at two different densities: (a) sparsely, at 7% of the image width and (b) densely, at 3%. . . 80

4.4 *Histograms of worker performance (left) and time spent (right).* Vertical axis on both plots: number of users. Left: percentage of sentinel data answered correctly. Right: time spent and effective wage (pay per task / time spent). 83

4.5 Points on a fabric surface with a cast shadow. 85

4.6 Example decompositions using our algorithm for a variety of scenes. All outputs are rescaled and mapped to sRGB for display. 96

4.7 Quantitative comparison of our algorithm against several recent open-source algorithms, using mean weighted human disagreement rate ($\text{WHDR}_{10\%}$). For (c), only the 397 densely sampled photos are considered (about 900 judgements per photo with a minimum separation of 3% of the image diameter). All values are computed using leave-one-out cross validation. See Section 4.5.2 for details. 105

4.8 Challenging scenes that violate our assumptions. Using the parameters from Sec. 4.5.1, we obtain WHDR = $67\%, 45\%, 43\%$. . . . 110

5.1 **Inside-Outside Net (ION).** In a single pass, we extract VGG16 [166] features and evaluate 2000 proposed regions of interest (ROI). For each proposal, we extract a fixed-size descriptor from several layers using ROI pooling [65]. Each descriptor is L2-normalized, concatenated, scaled, and dimension-reduced (1x1 convolution) to produce a fixed-length feature descriptor for each proposal of size 512x7x7. Two fully-connected (fc) layers process each descriptor and produce two outputs: a one-of-K class prediction ("softmax"), and an adjustment to the bounding box ("bbox"). 113
5.2 **Four-directional IRNN architecture.** We use "IRNN" units [105] which are RNNs with ReLU recurrent transitions, initialized to the identity. All transitions to/from the hidden state are computed with 1x1 convolutions, which allows us to compute the recurrence more efficiently (Eq. 5.1). When computing the context features, the spatial resolution remains the same throughout (same as conv5). The semantic segmentation regularizer has a 16x higher resolution; it is optional and gives a small improvement of around +1 mAP point. 117
5.3 Interpretation of the first IRNN output. Each cell in the output summarizes the features to the left/right/top/bottom. 121
5.4 **VOC 2007 normalized AP by size.** Left to right: increasing complexity. Left-most bar in each group: Fast R-CNN; right-most bar: our best model that achieves 79.2% mAP on VOC 2007 test. Our detector has a particularly large improvement for small objects. See Hoiem [79] for details on these metrics. 127
5.5 **Receptive field of different layer types.** When considering a single cell in the input, what output cells depend on it? **(a)** If we add two stacked 3x3 convolutions on top of conv5, then a cell in the input influences a 5x5 window in the output. **(b)** Similarly, for a 5x5 convolution, one cell influences a 9x9 window in the output. **(c)** For global average pooling, every cell in the output depends on the entire input, but the output is the same value repeated. **(d)** For IRNNs, every cell in the output depends on the entire input, but also varies spatially. 135

6.1 *Visual search using a learned embedding.* Query 1: given an input box in a photo **(a)**, we crop and project into an embedding **(b)** using a trained convolutional neural network (CNN) and return the most visually similar products **(c)**. Query 2: we apply the same method to search for in-situ examples of a product in designer photographs. The CNN is trained from pairs of internet images, and the boxes are collected using crowdsourcing. The 256D embedding is visualized in 2D with t-SNE. Photo credit: Crisp Architects and Rob Karosis (photographer). 138
6.2 *CNN architectures:* **(a)** GoogLeNet and **(b)** AlexNet. Either CNN consists of a series of simple operations that processes the input I and produces a descriptor x. Operations are performed left to right; vertically stacked operations can be computed in parallel. This is only meant to give a visual overview; see [167] and [99] for details including kernel sizes, layer depths, added nonlinearities, and dropout regularization. Note that there is no "softmax" layer; it has been removed so that the output is the D-dimensional vector x. 141
6.3 Our goal is to learn an embedding such that the object in-situ **(a)** and an iconic view of an object **(b)** map to the same point. We also want different objects **(c)** to be separated by at least a margin m, even if they are similar. Photo credit: Austin Rooke. 143
6.4 Siamese network abstraction. 145
6.5 *Training architectures.* We study the effect of several training architectures: (**A**) a CNN that is used for classification and then re-purposed as an embedding, (**B**) directly training an embedding, (**C**) also predicting the object categories C_q, C_p, and (**D**) also normalizing the embedding vectors to have unit L2 length (since Euclidean distance on normalized vectors is cosine distance). Loss for classification: softmax loss (softmax followed by cross-entropy); loss for embedding: contrastive loss. 147
6.6 Example product tags from in-situ objects to their products (Houzz.com), highlighted with blue circles. Two of the five tags contain iconic photos of the product. Photo credit: Fiorella Design. 149
6.7 *MTurk interface.* A video of the interface and instructions are included in the supplemental (`http://www.seanbell.ca/tmp/siggraph2015-supplemental-bell-bala.zip`). Photo credit: Austin Rooke. 149
6.8 *Example sentinel*. Left: product image shown to workers. Center: ground truth box (red) and product tag location (blue circle). Right: 172 worker responses with bounding box (black) and circle (red), rendered with 20% opacity. Photo credit: Increation Interiors. 150

6.9 *Training procedure.* In each mini-batch, we include a mix of **(a)** positive and **(b)** negative examples. In each iteration, we take a step to decrease the loss function; this can be viewed as "forces" on the points (red arrows). Photo credit: Austin Rooke. 154
6.10 *2D embedding visualization using t-SNE [179].* This embedding was trained using architecture **D** and is 256D before being non-linearly projected to 2D. To reduce visual clutter, each photo is snapped to a grid (overlapping photos are selected arbitrarily). Full embeddings are in the supplemental (http://www.seanbell.ca/tmp/siggraph2015-supplemental-bell-bala.zip), including those for a single object category. Best viewed on a monitor. 156
6.11 *Quantitative evaluation (log scale).* Recall (whether or not the single tagged item was returned) as a function of the number of items returned (k). Recall for each query is either 0 or 1, and is averaged across 10,000 items. "GN": GoogLeNet, "AN": AlexNet, "Euc": Euclidean distance, "Cos" cosine distance, "Siam": trained with a Siamese network, "Cat": trained with object categories, "IN": ImageNet weights (not trained at all), "P=16": the box is expanded so that after warping to a square, there are 16 pixels of padding. Random guessing is flat along the bottom. 160
6.12 *User study for cross-category searches.* Number of times that a user clicked on the prediction from a given algorithm. Error bars: 95% confidence interval (bootstrap sampling). Naming conventions are explained in Figure 6.11. 160
6.13 *In-situ product search: random uncurated queries searching the test set*. Here, the query is a product, and the retrievals are examples of where that product was used in designer images on the web. The boxes were drawn by mturk workers, for use in testing product search; we are assuming that the localization problem is solved. Also note that the product images (queries) were seen during training, but the scenes being searched over were not (since they are from the test set). When sampling random rows to display, we only consider items that are tagged at least 7 times (since we are showing the top 7 retrievals). We show many more in the supplemental (http://www.seanbell.ca/tmp/siggraph2015-supplemental-bell-bala.zip). . 167

CHAPTER 1

INTRODUCTION

Automatically understanding scenes is the holy grail of computer vision. Real-world scenes have a vast array of interesting objects, materials, textures, and surfaces. With scenes, people want to edit photographs, search by object and material properties, visualize changes to rooms and buildings, browse collections by visual similarity, and explain images to the visually impaired. Scenes also play a key role in robotics—agents need to understand the materials and properties of objects in its environment in order to interact with the physical world. Materials and objects are at the core of all of these tasks. However, the tools and data that we have for recognizing, editing, and exploring applying scene properties for everyday problems are still quite limited. We cannot easily understand, search, and aggregate visual concepts in the billions of photos that are uploaded every day to the web.

Scene recognition is a long-standing, challenging problem due to the totally unknown relationship between the input image (an array of pixel intensities), and the semantic properties represented in that image. Pixels contain an unknown combination of objects, materials, geometry, lighting, occlusions, and camera intrinsics, so that separating these properties is nearly impossible in a fully general algorithmic way. Despite these difficulties, humans are adept at recognizing all of these concepts in images. There is the potential to ask people to provide millions of examples of answers, allowing computer vision researchers to pose recognition as a learning problem. Posed this way, the challenge is decoupled into two new problems: (1) how to get people to efficiently, cheaply, and accurately label the properties you want in images, and (2) how to learn a

model that matches the answers provided by people. To obtain labels at scale, we turn to crowdsourcing online, which introduces new challenges—workers are unreliable, inconsistent, and do not have the expertise to directly label the properties we need. Once we have these labels, the final challenge is using the right learning algorithm. For that, we use deep learning and convolutional neural networks.

In this thesis we further our understanding of scenes along many facets—we develop new crowdsourcing methods as well as new state-of-the-art algorithms that learn from data. Further, we model scenes at many levels of abstraction. At the lowest levels of abstraction, one can study the physics and interaction of light as it bounces around the scene—light traveling from light sources in the scene, absorbed by surfaces, transmitted through media, and ultimately absorbed by cameras and projected onto an image sensor. At an intermediate level of abstraction, we can consider the human-centric semantics imposed on the world, and group them into distinct surfaces, materials, and objects. At the highest level of visual abstraction, we consider which objects are visually and stylistically compatible together—which ensembles of items go well together in a scene.

Our first contributions are to collect appearance information at a large-scale, which has not been done before for materials (Chapter 2). We use this to inform and drive new algorithms to understand materials at pixel-level material categories (Chapter 3) and pixel-level reflectance (Chapter 4). We then develop higher level algorithms to detect objects in images (Chapter 5), and recognize objects at a fine-grained per-object level (Chapter 6). Together, these contributions significantly advance our knowledge of what information can be extracted from

an image.

Chapter 2 presents our first major contribution, *OpenSurfaces*, a rich, labeled database consisting of thousands of examples of surfaces segmented from consumer photographs of interiors. These surfaces are annotated with material parameters (reflectance, material names), texture information (surface normals, rectified textures), and contextual information (scene category, and object names). We use human annotations and present a new methodology for segmenting and annotating materials in Internet photo collections suitable for crowdsourcing (e.g., through Amazon's Mechanical Turk). Because of the noise and variability inherent in Internet photos and novice annotators, designing this annotation engine was a key challenge; we present a multi-stage set of annotation tasks with quality checks and validation. We demonstrate the use of this database in proof-of-concept applications including surface retexturing and material and image browsing, and discuss future uses. OpenSurfaces is a public resource available at `http://opensurfaces.cs.cornell.edu/`. Since releasing our interface, researchers from Microsoft have used our segmentation interface to power the Microsoft Commons Objects in Context (MS COCO) project which labeled over 2.5 million objects; this data has significantly advanced the state-of-the-art in object detection.

Chapter 3 considers the mid-level visual problem of recognizing materials in an image, building on the dataset from Chapter 2. We present the *Materials in Context Database* (MINC), a new, large-scale, open dataset of materials in the wild, and combine this dataset with deep learning to achieve state-of-the-art material recognition and segmentation of images in the wild. MINC is an order of magnitude larger than previous material databases, while being

more diverse and well-sampled across its 23 categories. Using MINC, we train convolutional neural networks (CNNs) for two tasks: classifying materials from patches, and simultaneous material recognition and segmentation in full images. For patch-based classification on MINC we found that the best performing CNN architectures can achieve 85.2% mean class accuracy. We convert these trained CNN classifiers into an efficient fully convolutional framework combined with a fully connected conditional random field (CRF) to predict the material at every pixel in an image, achieving state-of-the-art accuracy. Our experiments demonstrate that having a large, well-sampled dataset such as MINC is crucial for real-world material recognition and segmentation. Since releasing MINC, new semantic segmentation algorithms have been proposed that were trained on our data to further advance the state of the art.

Chapter 4 considers a related problem of a challenging low-level visual property: surface reflectance. This problem is usually posed as the "intrinsic images" problem, the separation of an image into a reflectance layer and a shading layer. In this chapter, we present *Intrinsic Images in the Wild* (IIW), a large-scale, public dataset for evaluating intrinsic image decompositions of indoor scenes. We create this benchmark through millions of crowdsourced annotations of relative comparisons of material properties at pairs of points in each scene. Crowdsourcing enables a scalable approach to acquiring a large database, and uses the ability of humans to judge material comparisons, despite variations in illumination. Given our database, we develop a dense CRF-based intrinsic image algorithm for images in the wild that outperforms a range of state-of-the-art intrinsic image algorithms. Intrinsic image decomposition remains a challenging problem; we release our code and database publicly to support future research on this problem, available online at `http://intrinsic.cs.cornell.edu/`.

Since releasing our dataset, others have used our data to further advance the state-of-the-art by training deep learning models and expanding on our CRF-based algorithm.

Chapter 5 develops a new object detection algorithm that is significantly more accurate than the previous state-of-the-art for this problem. Specifically, we present the *Inside-Outside Net* (ION), an object detector that exploits information both inside and outside the region of interest. In the chapter, we will explain our new architecture that uses contextual information with recurrent neural networks and skip pooling. Through extensive experiments we evaluate the design space and provide readers with an overview of what tricks of the trade are important. ION improves state-of-the-art on object detection by a significant margin. In the 2015 MS COCO Detection Challenge, our ION model won "Best Student Entry" and finished 3rd place overall. As intuition suggests, our detection results provide strong evidence that context and multi-scale representations improve small object detection.

Chapter 6 explores the highest level of visual abstraction—visual similarity. In this chapter we learn an embedding for visual search in interior design. Our embedding contains two different domains of product images: products cropped from internet scenes, and products in their *iconic* form. With such a multi-domain embedding, we demonstrate several applications of visual search including identifying products in scenes and finding stylistically similar products. To obtain the embedding, we train a convolutional neural network on pairs of images. We explore several training architectures including re-purposing object classifiers, using siamese networks, and using multitask learning. We evaluate our search quantitatively and qualitatively and demonstrate high quality results for search

across multiple visual domains, enabling new applications in interior design. Since releasing our paper, other researchers have shown that this approach also works for 3D shapes, clothing, and sketches.

In this thesis we have introduced first-of-their-kind large scale datasets for material and reflectance annotation of images in the wild. We combine these datasets with innovative techniques in learning to create state-of-the-art algorithms in material recognition, intrinsic image decomposition, object detection, and visual and style similarity.

CHAPTER 2

OPENSURFACES: A RICHLY ANNOTATED CATALOG OF SURFACE APPEARANCE

2.1 Introduction

In this chapter, we address the first challenge in scene understanding—efficiently collecting large-scale visual data from photographs. While there has been work on collecting object categories and scene labels [176, 43, 195, 152], materials, reflectances, and textures are largely unexplored. While this kind of visual data is immensely valuable for training deep learning algorithms (as used in Chapter 3), in this chapter we also show its direct use: exploring photo collections by materials, visualizing changes to scenes, visualizing what materials go together, and others. We release our data as a public resource available at http://opensurfaces.cs.cornell.edu/.

The tools and data that we have for exploring and applying materials and textures for everyday problems are currently quite limited. For instance, consider a homeowner planning a kitchen renovation, who would like to create a scrapbook of kitchen photographs from which to draw inspiration for materials, find appliances with a certain look, visualize paint samples, etc. Even simply finding a set of good kitchen photos to look at can be a time-consuming process. Interior design websites, such as Houzz, are starting to provide forums where people share photos of interior scenes, tag elements such as countertops with brand names, and ask and answer questions about material design. Their popularity indicates the demand and need for better tools. For example, people want to:

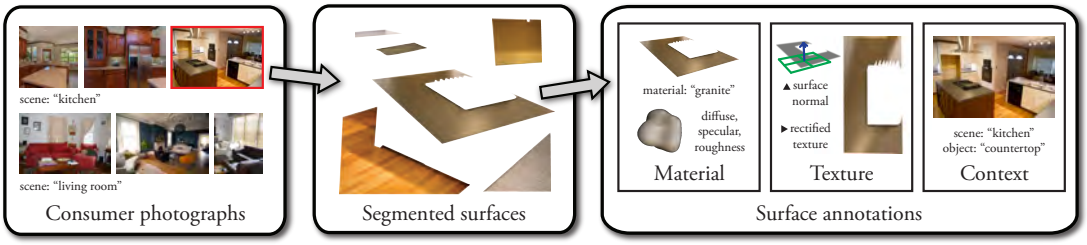

Figure 2.1: We present OpenSurfaces, a large database of annotated surfaces created from real-world consumer photographs. Our annotation pipeline draws on crowdsourcing to segment surfaces from photos, and then annotates them with rich surface appearance properties, including material, texture, and contextual information.

- Search for examples of materials or textures that meet certain criteria (e.g. "show me kitchens that use light-colored, shiny wood floors")
- Find materials that go well with a given material ("what do people with black granite countertops tend to use for their kitchen cabinets?")
- Retexture a surface in a photo with a new material ("what would my tiled kitchen look like with a hardwood floor?")
- Edit the material parameters of a surface in a photograph, ("how would my wood table look with fresh varnish?")
- Automatically recognize materials in a photograph, or find where one could buy the materials online (search-by-texture).

To support these kinds of tasks, we present OpenSurfaces, a large, rich database of annotated surfaces (including material, texture and context information), collected from real-world photographs via crowdsourcing. As shown in Figure 2.1, each surface is segmented from an input Internet photograph and labeled with material information (a named category, e.g., "wood" or "metal", and reflectance parameters), texture information (a surface normal and rectified texture), and context information (scene category and object name). Compared to existing material databases, ours takes a "big data" approach, collecting large

numbers of example materials captured *in situ* in their surrounding context. Just as massive databases of images and objects have led to new advances in image editing [76, 103] and object recognition [152], we believe that a large and comprehensive catalog of *contextual surface appearance properties* is critical for everyday applications involving exploring, editing, and recognizing materials and textures. To our knowledge, ours is the first large-scale database of rich, annotated surface appearance information of its kind.

A central challenge in creating such a catalog is that automatically recovering material properties from images is a notoriously difficult inverse problem that requires careful calibration [193] or strong assumptions about the image formation model [147]. Our images are scraped from Flickr, so objects appear under a wide range of uncontrolled lighting conditions, with unknown scene geometry. These properties raise the question of whether it is possible to recover *any* usable material information from such images. This drives a key aspect of our system: we ask humans to judge these properties in uncalibrated settings, leveraging the fact that people are good at recognizing and categorizing materials across a range of lighting conditions and image quality. To scale to the large numbers of images, materials, and textures we want, we use crowdsourcing on Amazon's Mechanical Turk (MTurk).

Even with humans in the loop, creating a useful surface catalog is very challenging. Internet photos are noisy, the quality of results from MTurk labelers can vary widely, and interfaces involving material parameters can be difficult for novice users to understand. To get usable results, we designed a multi-stage annotation pipeline, involving multiple types of tasks, to collect and verify surface annotations, including material, texture, and contextual information.

We evaluate the quality of this approach and demonstrate the utility of this database in proof-of-concept applications including surface retexturing and appearance browsing. We believe that the availability of such a database can be helpful to many applications in graphics and vision, beyond the ones we demonstrate.

This chapter makes the following contributions:

- A new, large-scale open source database of surface appearance (with thousands of entries and growing) annotated with material, texture, and contextual information available at http://opensurfaces.cs.cornell.edu/.
- A methodology for creating such a database through crowdsourcing annotations of Internet photo collections.
- A publicly available annotation pipeline to spur further exploration and use of such data in graphics and vision applications.
- A demonstration of proof-of-concept uses of such richly annotated surface information.

2.2 Related work

Image databases. Over the past few years, researchers have shown the utility of "big data"—in the form of large, annotated image databases—for addressing difficult problems in graphics and vision. These databases include 80 Million Tiny Images [176], ImageNet [43], the SUN scene database [195], and the LabelMe dataset [152]. LabelMe has similar goals to ours and uses a significant amount of user annotation, but their focus is on labeling objects, rather than materials. Other

work has extended systems such as LabelMe to material name annotations [47].

While the work described above comprises very large databases of images, objects, and scenes, existing databases of natural images of *materials* are relatively small. This category includes the Flickr Materials Database (FMD) [114] and the datasets of Hu, et al. [81]. These datasets are largely made up of close-up photos of objects made of a single substance, such as wood or glass, and have primarily been used for the problem of material categorization. The PSU Near-Regular Texture Database consists of closeups of textured patterns, including material textures [118].

In contrast, our aim is to build a database of materials *in context* in photos of everyday scenes, so that we can support applications like interior design that involve whole scenes, rather than single objects or materials. Moreover, prior databases annotate each image with a single category label (e.g. "wood," "glass"), while we collect a much richer set of annotations that include reflectance parameters and surface normals, enabling a wider class of potential applications.

Crowdsourcing. The use of crowdsourcing to collect data is gaining adoption, and has been used in recent approaches to a range of problems, including understanding shape through gauge figures [38], creating a mesh segmentation database [32], devising a retargeting evaluation framework [148], and for integrating humans into the loop for microtasks [61]. The experiences from this body of prior work has informed our design process.

Material acquisition and databases. Material acquisition is an active area of research (for a recent survey, see [193]). A few public databases exist with

carefully calibrated measurements, including the MERL database [121] with 4D BRDF measurements for 105 materials, fit to various BRDF models [124], and CUReT [39], with 6D measured BTFs (bidirectional texture functions) for 61 samples with various lighting and illumination conditions. The complexity of acquisition and quality of these databases has typically limited their size. To help address these issues, appearance acquisition research has focused on hardware solutions [145], but large databases of measured materials are still difficult to acquire.

Rather than capture detailed, high-quality reflectance information for a small number of materials under controlled conditions, our goal is complementary; we aim to gather large numbers of surface annotations, *in situ*, from photographs taken under a wide variety of uncontrolled settings. Since humans provide annotations, we aim for perceptually plausible appearance data.

2.3 Overview

We present an overview of OpenSurfaces, and discuss some of our key design decisions. Our annotation pipeline takes as input a set of consumer photos depicting one or more surfaces, in context, in an interior scene, such as a kitchen. Each photo is processed in multiple stages, resulting in segmented surface regions (e.g., countertops, floors, cabinets, drawer handles, etc.), where each segment is annotated with material, texture and contextual information.

Creating this database involves several challenges:

- How can we create a high-quality database from consumer photographs?

What kinds of photos should we use?

- How can we help novice labelers annotate surfaces? How can we scale this annotation to build a very large database?
- What information is represented in the database?
- What tasks are needed to build this database?

2.3.1 Community photo collections

One important motivation of our work is to collect a large range of everyday surfaces *in context* from everyday imagery. By "in context," we mean that we want to capture the settings in which various surfaces appear—for instance, where a given type of material tends to appear in an image, what kinds of objects it belongs to, and what other materials it appears in combination with. We chose to focus on indoor locations such as kitchens, living rooms, and dining rooms, which contain indoor materials of practical use, though it is easy to generalize our approach to broader categories.

We use Creative-Commons-licensed Flickr photos as the main source for our images, as we found that Flickr contains a vast range of real, everyday materials in context in high-quality photos. Images from the SUN database [195] were not usable for our purposes because they are typically not of high enough resolution.

2.3.2 Human annotation

Online consumer photos are far removed from the carefully calibrated, high-dynamic range images typical of material acquisition. Our photos contain mul-

tiple materials on surfaces of unknown geometry, are captured under widely varying and unknown lighting conditions, lack radiometric calibration, and may have been post-processed. Hence, extracting meaningful surface properties from these images is well beyond the state-of-the-art of automatic inverse rendering algorithms. Optimization [147] and machine learning approaches [46, 114] to inferring materials have been studied recently, but do not yet demonstrate the performance necessary to annotate materials in noisy, real-world images. These considerations motivate another major design choice in our approach: using humans to annotate our images via crowdsourcing. Humans are reasonably good at identifying materials and their properties over a range of lighting conditions [53], and the availability of crowdsourcing lets us collect annotations at scale for large image collections.

In this chapter we focus on an annotation pipeline we deployed on Amazon's Mechanical Turk (MTurk), as MTurk provides a platform for annotating many images in a short amount of time and at low cost. However, our system can also be run as a stand-alone interface hosted on our servers, so that new photos can continue to be annotated (similar to [152] for object labeling).

We faced two main challenges in getting useful annotations from labelers. First, annotating surface properties in a photo is not a familiar task to most people, and even communicating what we mean by a "surface," "material," or "texture" to a novice is difficult. Second, MTurk annotators can be unreliable—users can ignore instructions or intentionally provide bad labels. To deal with these sources of noise, we split our material annotation tasks into several subtasks, with the goal of making each subtask as simple, modular, and intuitive as possible. We also use techniques to account for noise, and to verify the results of each subtask.

To improve robustness to noise, we use the CUBAM machine learning algorithm of Welinder, et al. [191] which uses a model of noisy user behavior for binary tasks (e.g., voting for the quality of a surface) to extract better results. In part, it models the competence and bias of each user based on how often they are in agreement with other users.

2.3.3 OpenSurfaces data representation

Real-world surfaces can be characterized in many ways, including (in increasing order of complexity): names of material categories (e.g., "wood" vs. "metal" vs. "paper"), image exemplars, simple diffuse reflectance models, parametric BRDF models, 4D BRDF measurements, and 6D BTDF measurements. In choosing a surface representation for our database, we considered several factors. First, different representations are suitable for different tasks. For a material recognition task, one might want a database with segmented materials labeled with a category name ("wood" vs. "plastic"), for use in training classifiers. Other applications, such as interior design ("replace the wood floor in this photo with a shinier one"), might warrant a richer description of materials in terms of their reflectance. Hence, we collect multiple types of annotations for each surface, including material names and reflectance parameters.

Surface normals and rectified textures. While some types of surfaces we consider have a uniform BRDF, many, such as granite or wood, are highly textured. Thus, we chose to store texture information to describe surfaces as well. Because textures in photos can be significantly foreshortened by perspective, we create a subtask where labelers mark regions as planar or non-planar, and indicate the

surface normal of planar regions using a 3D perspective grid; this allows us to create and store *rectified* textures.

Reflectance. We ask labelers to annotate material parameters for segmented surfaces. Ideally, we would collect the most detailed BRDF information possible; we especially want to move beyond simple Lambertian models, because specular and glossy materials are extremely common in indoor scenes. On the other hand, there is only so much information that can be recovered from a single, uncalibrated image; moreover, our tasks should not be too difficult for human labelers. Thus, we chose to represent the materials using a simple parametric BRDF model (Section 2.4.7).

Data representation. Our final surface representation includes the following information for each surface (illustrated in Figure 3.2): material data (a material name, and reflectance parameters including diffuse albedo, gloss contrast, and gloss roughness), texture data (a surface normal and rectified texture (if planar)), and context data (an object name for the surface, and a scene category in which the surface occurs). Each surface also stores quality information, including a segmentation quality score and a planarity score.

2.3.4 Annotation stages

To build this representation for surfaces, our labelers perform a series of tasks in an annotation pipeline consisting of the following stages (Stage 0 is automatic, and the rest involve humans in the loop):

0. Download images of various scene categories from Flickr.
1. Filter out images that depict the wrong scene category.
2. Flag images that are improperly white balanced.
3. Segment regions of a single material/texture from each image.
4. Name the material for each region.
5. Name the object associated with each region.
6. Label each region as planar or non-planar.
7. Rectify each planar region by specifying a surface normal.
8. Match reflectance parameters for each white balanced region.

Every stage is carefully validated, with at least five labelers contributing to each decision, with some tasks (such as validating reflectance parameters) shown to up to ten.

2.4 The OpenSurfaces annotation pipeline

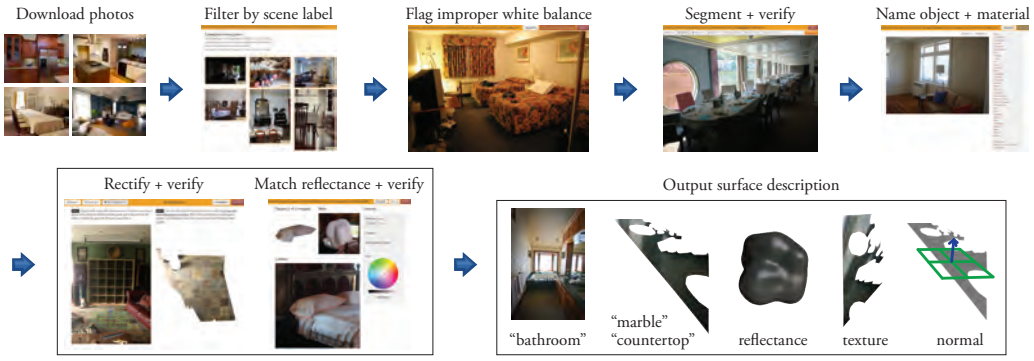

Figure 2.2: OpenSurfaces annotation pipeline. Each stage contains a typical example.

We now describe our annotation pipeline in detail. We first discuss how we obtain an initial set of input images, then describe the pipeline of tasks

performed on each image and segmented region. We ran several pilot studies for each of these tasks; we describe how these studies guided the design of our final interfaces and tasks. More details on each task are available in the supplementary document.[1] Figure 4.2 shows a block diagram of the annotation pipeline.

Stage 0: Collecting images. First, we needed to gather a set of high-quality images of indoor scenes. We obtain our images from Flickr, using search terms for each room type, such as "kitchen" and "living room" (see supplementary[2] for full list). Since our goal is to recover realistic parameters, we exclude images with the tag "hdr," which are typically highly stylized. We also limit our search to Creative Commons photos that allow "sharing" and "remixing," to ensure that our database can be used in a variety of applications.

We then group the remaining images by scene type. In total, we downloaded 1,099,277 images. We further pruned the list keeping only those photos that are: (a) color JPEG high-resolution ($\geq$ 6 megapixels), (b) at most 32MB in size (to control our disk footprint), and (c) have focal length information in their Exif headers (which we use for the rectification in Section 2.4.6). After this filtering step, we were left with a final set of approximately 207K images; we picked a few scene categories to focus on, giving us about 92K images.

2.4.1 Stage 1: Filtering images by scene category

Though we use the text tags associated with Flickr photos to download an initial set of photos, in practice these tags are quite noisy. For example, an image tagged

[1] http://www.cs.cornell.edu/~sbell/pdf/siggraph2013-opensurfaces-supp.pdf

[2] http://www.cs.cornell.edu/~sbell/pdf/siggraph2013-opensurfaces-supp.pdf

"kitchen" may depict a bar named "The Kitchen," or something else entirely. As in previous work on obtaining images of categories [43], we must curate the images of each scene category to find the relevant ones. In this task a labeler is shown a grid of 50 images drawn from a given category (e.g., "dining room"), and is asked to select all the images that belong to that category.

Each image was shown to five labelers. We found that labelers are very fast and reliable at this task, and pruned the image list down to about 25K images. Our database mostly contains scenes from the following categories: kitchen, living room, bedroom, bathroom, staircase, dining room, hallway, family room, and foyer.

2.4.2 Stage 2: Flag images with improper white balance

While human beings are able to judge material properties in a range of lighting conditions due to color constancy, there are limits to this ability [21], and the lighting conditions in online consumer photographs can be poor and highly variable from photo to photo. So that our labelers can reason about the true color of a surface as accurately and reliably as possible, we filter images that are significantly distorted in color space. To do so, we designed a task where labelers click on objects that they believe are white, and use this feedback to reject images that appear to be improperly white balanced. Users are prevented from clicking on pixels that are close to saturated ($R, G, B \geq 253$), or within 70 pixels of another point.

Each selected pixel is converted to $L^*a^*b^*$ color space. If the median value of $||(a^*, b^*)||$ is ≤ 15, then that user's submission counts as one vote towards the

photo being white balanced. Each photo is seen by five labelers; we run CUBAM on the full set of resulting votes, which yields a score (positive or negative) for each photo. If a photo receives a positive CUBAM score, then we consider it white balanced. We opted for this stringent rule because of the large size of our image collection; we can eliminate many images, and still have a large pool of remaining images to label. Compared to majority (3 out of 5) voting, CUBAM changed 14% of labels from good (white balanced) to bad (not white balanced), and 0.8% from bad to good.

Since material recognition is still possible in distorted color spaces [161], we only use white balancing to filter inputs for appearance matching (Stage 8).

2.4.3 Stage 3: Material segmentation

The next task is to segment regions of constant material or texture from each image. These regions will become the surfaces that are annotated in later tasks.

Pilot study. This task is related to the object segmentation task in LabelMe, but when we tried adapting LabelMe for our task, the interface proved to be cumbersome. We created a new interface with features (smooth zoom, undo/redo, automatic pan) designed to encourage better material segmentations; user feedback was very positive. The smooth zoom and automatic pan features were especially important, yielding segmentations with greater accuracy and more vertices. Without automatic pan (scrolling the view when users click near the edge), users often submitted clipped polygons.

For this task, a labeler is presented with an image and instructed to segment

six regions based on material and texture, and *not* object boundaries. The user is shown several examples of good and bad segmentations. An ideal segmentation contains a single material or texture, and tightly hugs the boundary of that material region. The user creates polygons by clicking in the image, or entering a mode where they can adjust an existing polygon (the interface zooms in for fine-scale adjustments; the user can also zoom in or out). The interface saves a full undo/redo stack, and logs all actions with a timestamp for later replay. The interface disallows self-intersecting polygons, but separate polygons can be nested or overlapping.

Once a labeler has segmented regions from the image, we post-process the polygons to create a set of disjoint shapes. This step is to address common cases that arise in these kinds of tasks where a large region of a single material contains a smaller region of a second material (e.g., a door with a handle, or a shower stall with a drain). The easiest way to label these kinds of surfaces is to provide the boundary of the outer shape, and separately the boundary of the inner shapes. Our post-processing stage detects such intersections and yields new shapes as follows: if one shape contains another shape, the inner shape is unchanged, and the outer shape has a hole corresponding to the inner shape; if two shapes partially intersect, three regions are generated to capture cases where the foreground partially intersects the background. The output is stored as a 2D mesh triangulated by [26]. The supplementary material[3] describes this process in more detail. While this technique can occasionally over-segment overlapping regions, we found it to be very useful in addressing common configurations.

[3] http://www.cs.cornell.edu/~sbell/pdf/siggraph2013-opensurfaces-supp.pdf

Voting for material segmentation quality

The quality of segmentations from this task varies widely; while many regions were surprisingly well-segmented, some were too small, or had sloppy boundaries, and others were good object (but not material) segmentations. We created an additional task where users vote on the quality of each segmentation; these votes are used to determine a quality score for each segmented surface region.

This voting task is somewhat subjective, since it is not always clear what constitutes a "single material" or how labelers interpret the word "texture". Thus, we accept shapes as high quality only if there is a certain amount of consensus. We asked five voters to vote on the quality of each segmentation, and ran CUBAM on the resulting votes. Compared to majority (3 out of 5) voting, CUBAM changed about 7.0% of the bad examples to good, and about 8.38% of the good examples to bad. By default, we discard shapes with a CUBAM-computed quality score below a threshold, but this threshold can be adjusted for applications that need higher-quality segmentations, or which can tolerate lower-quality segmentations.

As we ran the material segmentation task, we noticed that a few users produced exceptionally detailed segmentations, with an accuracy higher than the output of the above voting step. After collecting about 30,000 segmentations, we restricted the task to the best 26 workers (out of 530, using MTurk qualifications) and removed the voting step. This doubled the average detail from 11.6 to 20.3 vertices while reducing our total effective cost from \$0.035 to \$0.025/shape (including bonuses), since we were no longer paying for voting or for shapes that we later rejected. Even with the smaller set of workers, submission rates remained above 4,000 shapes/day.

2.4.4 Stages 4 and 5: Naming materials and objects

Finally, we want semantic information for each material segmentation: a **material** name, such as granite or wood, and an **object** name, such as wall, floor, or countertop. These kinds of labels can enable better searching of the database, interesting analytics ("what materials do countertops tend to be made of?"), and category labels for recognition and search.

Material names. The material name is meant to indicate the "stuff" [2] that gives the surface its appearance. In a pilot study, we designed an interface, inspired by LabelMe [152], where a user is presented with a material segment and asked to enter a freeform text label, with an "auto complete" feature to suggest material names from a database. However, we found a huge amount of noise in the labels that users entered—multiple different words for the same substance, and misspelled or non-English terms were common. Based on this study, we moved to an interface where a user chooses a material name from a discrete set of choices. We selected the potential names from the results of our pilot study, and taxonomies in interior design [87]. In total, we selected 34 possible material names. After observing that labelers struggled with painted surfaces (walls and ceilings), we introduced the category "painted" to include all surfaces with an outer layer of opaque paint. Without this label, users would guess the underlying surface, causing a split between "wallboard", "wood", "plaster", and "concrete". Users also struggled with laminate surfaces designed to resemble wood or granite. This was resolved by instructing workers to place fake granite and real granite into the same "granite" category (similarly for wood). Users were also given the option of selecting "not on list," "more than

one material," and "I can't tell." As the task progressed, we added 6 items to the list by observing items consistently labeled "not on list". The full list of 34 material names is provided in the supplementary material.[4]

Object names. We also create a separate task in which we collect object names, such as "floor" and "countertop," for each segmented surface region. Because we are most interested in categories of objects involved in material design, such as structural elements or worktops, we also limit users to a discrete set of object labels, where the list of labels depends on the material (e.g., "clothing" for fabric, "handles" for metal). We otherwise use the same interface as in the material naming task above. The full list of object names is provided in the supplementary material.[5]

To handle noise, we only keep a semantic label if 3 out of 5 labelers agree, which we found to be reliable. For both types of labels, labelers agreed on a label for about 80% of the segmentations.

2.4.5 Stage 6: Planarity voting

To rectify each surface region, or transfer that region to a new photo, we need to know the geometry of that surface. For many regions (e.g., a chandelier), the geometry can be quite complex; hence, we chose to identify regions with simple, planar geometry and treat these specially in our database. Planar regions are very common and account for an interesting class of objects that one might want to transfer between images (such as floors and countertops). Thus, we

[4] http://www.cs.cornell.edu/~sbell/pdf/siggraph2013-opensurfaces-supp.pdf

[5] http://www.cs.cornell.edu/~sbell/pdf/siggraph2013-opensurfaces-supp.pdf

created a task in which workers vote for whether a given segment lies on a single plane. For this task, we use an interface similar to that of the quality voting task, presenting workers with a grid of images zoomed into segments and instructing them to click on all segments that are planar. Each segment is shown to five users, and the results are aggregated using CUBAM.

2.4.6 Stage 7: Rectified textures

For each planar surface, we seek to create a rectified texture that appears to look "head on" at that surface. For this task, labelers are shown a photo with a planar region annotated in red, with a small grid and surface normal inside the region. They are instructed to "drag the blue arrow to point away from the surface." As they drag the grid, the surface is transformed in real time, via a homography computed from the normal and the image's Exif focal length, and shown to the right of the photo (see Figure 2.3(a)). The user adjusts the grid until the normal looks correct and the texture looks rectified. Users can also adjust the rectified result directly by dragging on it. We instruct users "tiles and wood patterns should appear parallel, and rectangles inside the shape should have 90 degree right angles." We also provide many examples of good and bad rectifications, and found that users produced higher quality results when shown negative examples featuring rectifications that are only slightly incorrect.

The grid and surface normal are rendered in perspective according to the image focal length. We set the 3D depth so that the grid projects to a constant width when facing forward. The live rectification is performed by constructing a WebGL scene and encoding the desired homography into the camera projection

matrix. Since the scaling within the texture plane is arbitrary, we apply a scaling transform to the homography so that the bounding box of the rectified shape fits exactly within the view.

While prior work typically uses a gauge figure to represent a surface normal figure [93, 38], we found a 3D perspective grid to be much more effective. We collected 10,000 normals of each type, and found that the RMS error between the submitted normals and final selected normals was 32.1 degrees for gauge figures and 14.9 degrees for planar grids.

When given a continuous space to explore, we found that users did not provide surface normals of sufficient accuracy to rectify surfaces, and so there was often some skew left in the rectified texture. We address this by detecting vanishing points (VPs) and snapping normals to the closest VP. We obtain VPs by finding line segments with LSD [185], then clustering the segments with J-Linkage [174], and solving for the optimal VP for each cluster [171, 52]. We then have five users vote on both the original and snapped normals. If both are voted "correct", we use the snapped normal.

2.4.7 Stage 8: Appearance matching

Our final task is to find reflectance parameters that match the appearance of each segmented surface (Figure 2.3(b)). In this task, a synthetic object is rendered alongside the surface to be matched (and with the photo as a backdrop). The design of this task involved several considerations, especially (1) the choice of synthetic scene to render (so as to give effective, accurate visual feedback to labelers with the goal of good appearance matching) and (2) the generality of the

material representation and ease of use of the interface.

Choice of synthetic scene. To create a synthetic scene for effective appearance matching, we had to choose a shape, material, and lighting to be rendered with the current user-selected parameters to give the labeler feedback. We ran several pilot studies before we settled on a set of design choices for our scene and interface.

Shape. Vangorp et al. [181] recommend the use of a blob shape for improved perception of material reflectances. We ran a study with an interface that included both a sphere and a blob, but found that the blob shape was preferred; our final interface uses just the blob (see Figure 2.3(b)).

Lighting. Initially, we hypothesized that matching the lighting of the input photo in our synthetic scene would provide the most effective cues to the user in this task. Because automatically inferring lighting is difficult, we ran a pilot study where we asked labelers to adjust spherical harmonic coefficients of an environment map to roughly match the lighting of the input photo—for instance, making the left or right side brighter based on windows present in the real scene. However, we found that users were not skilled at recreating lighting [140], especially in the low-dynamic range input images we provide. Fleming et al. [54] recommend the use of environment maps with natural lighting statistics to improve material perception. We selected the high dynamic range environment map of the Ennis-Brown House [42] (a high-quality environment map of an indoor scene). Other techniques for recreating lighting with user annotation (e.g. [90]) would be worth considering in the future.

Material choice. The choice of material representation was a tradeoff between accuracy and ease of labeling. Common choices in graphics are Ward-based models and microfacet-based models (e.g., Cook-Torrance and variants). We made our choice based on pilot studies as well as the material design study of Kerr and Pellacini [91], which found no preference between three broad classes of models: Ward [188], perceptual Ward [135], and a microfacet-based model. In our pilot studies with these models, we found that the intuitive explanation of the perceptual Ward parameters (contrast gloss (c), and distinctness of image (d) respectively) worked well in the MTurk setting, so we selected the perceptual Ward with a balanced optimization for grazing angles [59] as our model of choice. Note that because the intensity of the input illumination is unknown for our photos, the user-specified diffuse albedo is only correct up to a scale factor; however, the roughness values are absolute.

In another preliminary study we found that matching the color to the real object was the hardest part of the task (as also reported in [91]). To assist labelers with color matching, we modified our interface in three ways. First, we simplified our model to avoid having two separate color wheels for diffuse and specular color. Instead, we let the user select either: (a) a diffuse color, with uncolored specularity and specular roughness (shown in Figure 2.3(b)); or (b) a colored specular material with roughness, but no diffuse component for colored gloss. Second, to start our users off on the right track, we initialize the diffuse color based on an analysis of the photo. We perform a k-means clustering (with 4 clusters), on the pixels of the segmented surface, and use the mean of the largest cluster to initialize the color widget. Third, users may click on pixels in the segmented surface to set the color. These three modifications significantly improved the quality of our appearance matches, as users spent less time hunting

for matching colors; users stopped reporting that they had trouble finding colors, and 85% of submissions were voted to have a perceptual match for color.

Figure 2.3(b) shows our interface, including a target image region to be matched cropped from the photo, the surrounding context with the region highlighted in red, the rendered 3D blob, and a series of perceptual sliders to edit blob appearance. To specify color, we use a HSV (hue, saturation, value) widget, as in [91].

Rendering and precomputation. Since the task runs in the browser, we made minimal assumptions about users' graphics cards and bandwidth capabilities. This precluded the use of sophisticated precomputation-based methods [16] with high compute and memory requirements. To achieve interactive performance, we ignore inter-reflections in the blob. Instead, we prefilter environment maps to obtain a diffuse map and 16 gloss maps at different roughnesses sampled according to the d axis from the perceptual Ward model, with $\alpha \in [0, 0.2]$. The HDR prefiltered maps are packed into RGBE textures and encoded as PNG files (1.6MB). At render time, the blob normal is rasterized, and two texture lookups are performed for the diffuse and gloss components from the prefiltered maps; the result is tone-mapped using Reinhard [144]. We assume that the log-average luminance (required by [144]) is approximately constant, so it can be stored offline.

Quality. To filter out low quality submissions, we show every match to ten users: five evaluate the color, and five evaluate the gloss if the color matches. We found that evaluating both properties at once causes users to ignore gloss and focus only on color. As with the other voting tasks, we aggregate the results with

CUBAM.

2.5 Results

In this section, we analyze the OpenSurfaces data collected to date (these statistics reflect a snapshot in time, and will change as the database continues to grow). We also discuss the cost and effectiveness of each task (see Table 2.1).

2.5.1 OpenSurfaces statistics

We present statistics on the surface data (segmentations, textures, reflectances, and contextual data) collected using our methodology.

Images. Our database currently contains 25,357 curated images, from an initial set of 91,868 sent through the curation task. From our large set of downloaded photos, we prioritized room categories with the largest number of images: kitchens, bathrooms, and living rooms; these have the greatest representation in our database.

Material segmentations. Our database consists of 70,005 segmentations deemed to be good by CUBAM out of 103,513 user-submitted polygons. Figure 2.5 summarizes the shapes in our database, as well as their quality, as determined by user voting and the CUBAM outputs. Figure 2.4 shows examples of our segmented surfaces (see the website (`http://opensurfaces.cs.cornell.edu/`)) for many more). Figure 2.5 (left) shows a histogram of vertex counts over

all submitted polygons. Users were required to create polygons with at least four sides, though there are a considerable number of polygons (over 12,000) with more than 30 vertices (the most complex polygon to date has 2,191 vertices). Figure 2.5 (center) shows a histogram of CUBAM-computed quality scores for all shapes after quality voting. The peak near 0 corresponds to shapes with high disagreement among labelers. This accords well with user feedback about ambiguous cases.

We observed that the amount of disagreement between labelers varies considerably depending on the task. Image curation (Stage 1) had the most agreement, with the fewest number of items with small CUBAM scores. Finally, Figure 2.5 (right) shows the average CUBAM quality score for shapes as a function of their vertex count. Not surprisingly, more detailed shapes also tend to be of higher quality (as observed anecdotally in other work, including LabelMe).

Material and object names. In total, we have 58,928 surfaces annotated with a material name, and 33,378 annotated with object names. These labels allow for interesting analytics, such as: What distributions of materials tend to appear in each type of room? What kinds of objects tend to appear in each material category? Our website includes up-to-date statistics for typical material distributions. Because our dataset has a few forms of bias (see Section 6.6), these numbers are not necessarily representative of rooms or objects in general, but still reveal interesting trends in our data.

Planarity. Surprisingly, many users struggled with the idea of planarity. For validation, we manually reviewed 35,000 planar outputs and observed a precision of 96.5%. Almost all of the mistakes were from users conflating piecewise-planar

with planar, selecting surfaces such as two walls, despite specific instructions and examples to avoid this case. While it only took a few hours to find and remove the 3.5% of the outputs, we could add a follow-up stage that specifically filters out piecewise-planar regions.

Rectified textures. Compared to the earlier tasks, rectifying a planar surface (by specifying a surface normal in the image) is evidently much more difficult. Out of 21,808 shapes that were input to our rectification task, about 16,882 (77.4%) shapes had a surface normal (or snapped surface normal) that was voted as "correct". While individual users were generally poor at the rectification task, even lazy labelers were accurate enough that snapping to the nearest vanishing point often produced the correct normal.

When voting on submissions, labelers were reasonably capable of judging "correct" normals, but struggled to interpret the resulting rectified texture. On average, incorrect normals that were judged to be "correct" were 12 degrees away from the correct normal. For some reason, we found a particularly high number of malicious users for this task; it was necessary to separately detect and block users who selected "yes" for every proposed match. Examples of the final rectifications are in Figures 2.6 and 2.7 (see website for more).

Reflectance parameters. Appearance matching (by specifying reflectance parameters) was also a challenging task; out of 40,148 surfaces annotated with reflectance parameters, about 27,648 (69%) were accepted as having sufficient quality. Figures 2.8 and 2.9 show examples of high-quality appearance matches (see website for more).

Task	Pay/item	Time	N in	N out	% out
Scene curation	$0.0004	1.8 s	91,868	25,357	27.6%
White balance	$0.0036	16.4 s	24,771	17,839	72.0%
Segmentation	$0.0160	25.8 s	16,282	103,513	N/A
Seg. Quality	$0.0009	3.1 s	54,963	29,467	53.6%
Material name	$0.0033	7.6 s	70,376	58,928	83.7%
Object name	$0.0028	7.2 s	43,058	33,378	77.5%
Planarity	$0.0010	2.7 s	60,800	38,446	63.2%
Rectification	$0.0200	35.6 s	21,808	21,808	N/A
Rect. Quality	$0.0020	3.6 s	21,808	16,882	77.4%
Reflectance	$0.0138	20.0 s	40,148	40,148	N/A
Color Quality	$0.0015	2.9 s	40,148	33,935	84.5%
Gloss Quality	$0.0014	2.9 s	33,791	27,648	81.8%

Table 2.1: *Summary statistics.* For each task we present: the average cost per item in USD (includes MTurk commission), the average time, the number of items assigned to labelers (**N in**). For naming tasks, **N out** is the number of shapes that had at least 3/5 agreement. For voting and quality tasks, **N out** is the number of items classified as "good" as a result of performing that task. As discussed in Section 2.4.3, we stopped measuring segmentation quality after limiting to the 26 best workers.

As one would expect, users were much more skilled at judging the correctness of matches compared to providing new matches. For each shape, the variance of the perceptual Ward parameters (c and d), decreased from 0.00714 to 0.00452 (34%) and from 0.00297 to 0.00287 (3%) respectively as a result of the two quality voting stages. To further explore the effect of d, and further validate the quality of this pipeline, we added a synthetically rendered image rendered with a state-of-art global illumination algorithm [186]. Compared to ground truth, the recovered roughness parameter (d) had an RMS error of 0.057 (28% of the range). Fleming et al. [53] found an RMS error of 16% for roughness (d) when matching identical spheres across varying illumination. When comparing materials across different geometries (same illumination), Vangorp et al. [181] found that users can correctly decide if two different objects have the same material 62% of the time. Our images with varying shape and lighting are more challenging, and our matches appear in line with these perceptual studies.

2.5.2 Task analytics

We now present statistics about our set of tasks, as well as additional observations about the results. Table 2.1 shows summary statistics for each type of task, including (1) the average payment for each item per task, (2) the average amount of time spent per item, (3) the number of input items processed, and (4) the fraction of output items that were rated as "good". A total of 1,770 MTurk labelers contributed to the database. As shown in the table, we observe a large disparity in the time and cost required across the set of tasks (by up to two orders of magnitude, in terms of cost). The fastest and least expensive task was curating the initial photo set, where each processed photo cost a fraction of a cent. The other voting tasks were also relatively inexpensive and fast, each taking less than 4 seconds. Interestingly, it required more pay to get labelers to quickly name materials compared to objects; labelers seemed to prefer thinking about objects instead of materials. The task which took the most time per item was rectification, which took more than 30 seconds per shape, on average. In our experience with this task, it often takes a significant amount of fine adjustment of the surface normal to achieve a good rectification. Perhaps unsurprisingly, rectification and appearance matching were the two most expensive tasks.

An important metric for evaluating MTurk use in collecting a large database is the rate of data collection at a particular price point. We found that submission rate was strongly correlated with price, the speed at which we approve tasks, and the reputation we built with workers. Our submission rate continued to improve as we built trust and communicated with workers. With a cost of about 13 cents per surface (10 cents if non-planar), our initial submission rates improved from a few hundred per day to rates of 4,200 segmentations, 4,500 reflectances, and

15,000 semantic labels per day.

Observations. In developing our tasks and working with labelers on MTurk, we made a number of interesting observations. Many users told us they really enjoyed the segmentation task, and produced beautifully detailed segmented surfaces. We found that our best segmentations were produced by a handful of people, some of whom created thousands of surfaces. On the other hand, some people created good *object* segmentations. In the future, these shapes could be sent back into the pipeline for further segmentation.

The two most difficult tasks were rectification and appearance matching. For appearance matching, users especially struggled with matching near-mirror materials. While they were skilled at selecting color using our interface, many labelers seemed hesitant to select low roughness (high d). This could be due to the fact that at low roughness, users can see the difference between the reflected environment map and the true scene. In the future, we plan to test specialized reflectance models for objects labeled as "mirror" or "glass". On the other hand, we observed that users often correctly used contextual information, such as the appearance of a different object in the image, to aid in appearance matching. This was especially helpful for matching gloss, where highlights suggesting appearance may only appear in other parts of the scene. For example, labelers might use the gloss on nearby cabinet doors to attribute roughness parameters to the similar surface being annotated, despite no discernible gloss being visible on it. Finally, some surfaces in our database are multicolored; we found that in such cases, users consistently matched the dominant color as initialized by k-means clustering.

Feedback and quality incentives. Rather than raising the pay for all tasks uniformly, which did not result in higher quality (as has been observed by others [120]), we targeted good users for bonuses and feedback on the quality of their work. For segmentation, we paid up to 10 times the base rate depending on the complexity of the submission. On average, we paid an extra 25% in bonuses. Since users are paid a fixed rate by default, there is otherwise no incentive to spend extra time producing detailed submissions. One user replied "It's difficult but I appreciate your positive feedback when you approve/reject the HITs, so I'm motivated to please you!" In addition to providing positive feedback, we found it was necessary to prevent 159 users from doing our tasks because they were either malicious or had an accuracy below 50%. The use of sentinels is recommended by [61] to check labeler quality. However, we found that our tasks are not amenable to this approach since our surfaces occur in distinctive photographs, and repetition tips off the labeler. We would like to revisit this in future work.

Sources of bias. In terms of representing places and surfaces, our dataset is biased in a few ways. First, our photos are from Flickr, which is biased towards higher-quality imagery (compared to other sites, such as Facebook), and geographically (Flickr is more widely used in the U.S. and Europe). Second, the keywords we use when searching for photos (intentionally) bias our data towards clean, uncluttered rooms. Third, our users are likely biased towards segmenting certain types of surfaces (as we require that they segment a fixed number of surfaces per image, not the entire photo). Factors such as saliency or ease of labeling likely play a role in a user's decision about what surfaces to label. Finally, since our environment map is fixed, differences in lighting between

the true scene and our proxy environment map could affect the reflectance judgement of users and introduce small color shifts. Our pipeline reduces this effect by rejecting improperly white balanced photos. However, further study is needed to understand the extent of these errors. In Chapter 3, we discuss an alternate method of collecting material labels that has a reduced bias against complex boundaries: individual point clicks.

2.6 Proof-of-Concept Applications

Our surface catalog can both assist and enhance existing and new applications in material search, browsing, editing, and classification. Here we describe a few such supporting proof-of-concept uses of the database, and discuss future applications.

2.6.1 Texturing

Richer texture exemplars. OpenSurfaces provides a large set of rectified real-world textures for use as texture exemplars. These improve over the corresponding unrectified and foreshortened textures, letting users of the catalog to expand their access to interesting real-world textures. Figure 2.10 illustrates this advantage.

Retexturing. Consider a user with a photograph containing a segmented surface (e.g., a countertop) who wants to visualize a home remodeling change to that surface. The user can browse OpenSurfaces for a suitable replacement using

the rich annotated data to search on color, material properties, object name, or substance type. The rectified textures found in our catalog can be used as the input to a texture synthesis algorithm (see Figure 2.11 for a synthesized granite texture drawn from our database to retexture a kitchen counter, with minor touch-ups applied as a post-process). While texture synthesis requires a clean example, and most of our shapes contain shadows or lighting, we did not find it difficult to select suitable shapes, since many shapes with undesired effects contain a clean inner region.

2.6.2 Informed scene similarity

Our database can be used to enhance image and material search (e.g., to generate ideas for interior design projects), by allowing for more targeted queries. With our rich annotations, we can explore interior scenes in ways previously not possible. For example, Figure 2.12 shows a search for wood flooring in kitchens and a search for fabric sofas in living rooms. Using our user-annotated reflectance parameters, we can further refine and sort the results by diffuse color similarity to the input query. While the input query is a segmented material from our database, the query can also be constructed by searching for a phrase (e.g. "kitchen wood floor") and selecting photos that have the desired color.

2.6.3 Future applications

There are many potential applications of a database of materials and surfaces beyond the proofs-of-concept we describe.

Search. Searching for photos that contain shiny or rough materials, or particular colors, can aid people interested in material design (e.g., interior decorating or home remodeling). Another search problem, search-by-material, could identify which paint or fabric can be bought from a store to best match an object in a photo. Further, our large database of community-gathered photos can be analyzed to discover common co-occurrences or relationships between certain materials. For example, we could tell what materials, objects or colors are often found above, below or nearby a given object. Similarly, we could offer suggestions to homeowners, answering such questions as: "for kitchens with black granite countertops, what kinds of materials are often used for cabinets?" We could also use existing materials to automatically recognize that the query contained black granite countertops, thus requiring the user to only submit an input photo. As our database grows, we could discover geographic or temporal trends in material design, given suitably tagged imagery.

Editing. Aside from search, material editing and transfer is also useful. Synthetic object insertion into photographs [42, 90] could use our material parameters for accurate compositing. Alternatively, one can imagine extending Photo Clip Art [103] to the domain of material compositing, where rather than attempting to accurately simulate lighting and shadows, one could search for a surface that contains the desired effects. The presence of surface normals can also aid reasoning about perspective or scene geometry. Finally, surfaces such as wood may appear very different depending on how the surfaces are treated (e.g., painted, or unfinished). Our database can potentially be combined with image editing software to visualize such effects.

Classification. We believe that one of the strongest applications of our database is enabling the automatic classification of materials and material properties. Our materials can form useful training data and priors for estimating the category, reflectance, and roughness of materials. Our database and photos are completely open, serving as a useful resource for these and other applications. Using this data, in Chapter 3, we build classifiers to predict the material of every pixel in an image. Others have also trained texture recognition and segmentation algorithms [37] that generalize to new in-the-wild images.

2.7 Conclusions and future work

This paper takes the first steps towards building a "big data" catalog of surface properties of everyday materials in our world, with reflectance, texture and contextual information for these surfaces. While the current data collected, with thousands of surfaces (and growing), can immediately be useful to many graphics and vision applications, many promising research directions remain.

Labelers often are faced with difficult questions; what is the reflectance of a mirror reflecting a pink wall, pink or glass? Developing better guidelines and interfaces for difficult surfaces like transparent and translucent materials is an interesting avenue of future work.

To further increase scalability, we plan to explore more automation to help users, especially for difficult tasks like rectification and appearance matching—it is often easier to improve on a good answer, or accept or reject an automatically generated result, than to create an answer from scratch. For example, our use of clustering of surface colors significantly improved labeler speed and accuracy

in appearance matching. Similarly, detecting vanishing points assisted in the rectification task. Indeed, our database can effectively bootstrap itself, by creating large amounts of training data useful for improving algorithms for tasks like material recognition [114] and reflectance estimation [46]. In Chapter 3, we build on our dataset and train per-pixel material classifiers.

Further, we would like to address the sources of bias in our input collections, by expanding to include more categories, and develop incentive systems to get a more complete annotation of images.

While we include quality controls at every stage of the pipeline, we are interested in further evaluating the quality of our data in comparison to controlled, in-lab methodologies. For reflectance, we plan to physically insert known objects into scenes and compare the reflectance returned by the pipeline to the measured material properties for those known objects. In addition, we plan to render and annotate a larger collection of synthetic scenes to validate surface normals, reflectances, and segmentations.

2.8 Impact

Our work was published at SIGGRAPH 2013 [12]. Our annotations from OpenSurfaces have enabled others to train texture recognition and segmentation algorithms [37, 36], and to redecorate rooms by automatically suggesting materials for indoor digital scenes [29]. Our dataset has also been expanded with new "describable texture attributes" and re-released as an augmented dataset [36]. Researchers from Microsoft have used our segmentation interface to power the Microsoft Commons Objects in Context (MS COCO) project [113] which labeled

over 2.5 million objects; this data has significantly advanced the state-of-the-art in object detection as part of the yearly MS COCO object detection challenge.

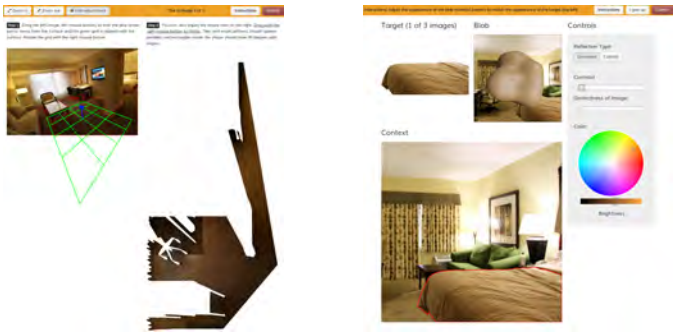

(a) Texture rectification (b) Appearance matching

Figure 2.3: (a) Stage 7: Rectifying planar textures interface. This figure shows a successfully completed task, where the perspective grid on the left appears to lie flat against the surface, and the texture, shown on the right, is correctly rectified. (b) Stage 8: Interface for appearance matching to recover material parameters.

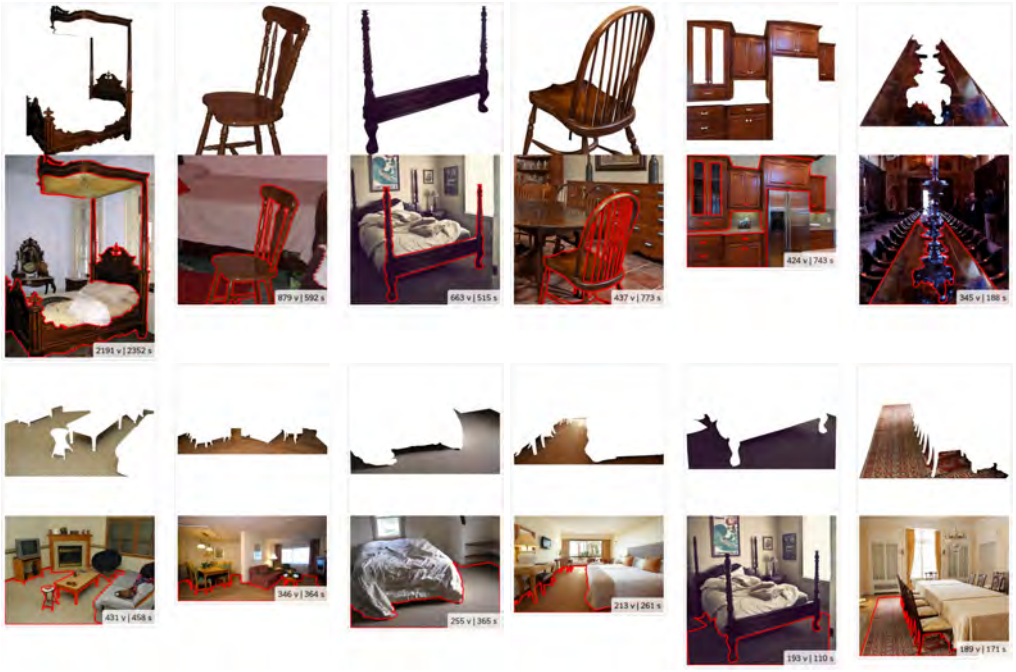

Figure 2.4: Example segmented surfaces labeled “wood” (top row) and “carpet” (bottom row). Each item shows the number of vertices and the time spent.

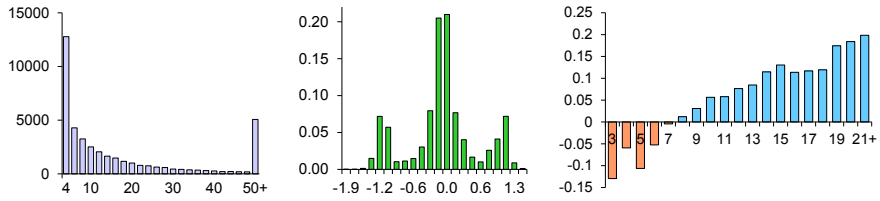

Figure 2.5: Statistics over shapes in our database. Left: Histogram of vertex counts, Center: Histogram of CUBAM scores from voting on shape quality, Right: Average CUBAM score for each vertex count.

Figure 2.6: *Example rectified textures.* Left: original photographs with segmented surface highlighted and user-specified surface normal. Right: rectified texture with provided surface normal.

Figure 2.7: *Example rectified textures.* Each row: textures rectified using normals from our database, sorted by decreasing vertex count. Each row contains a single type of material: wood, tile, marble, and granite.

Figure 2.8: *Example reflectance parameters.* First and third rows: material segmentations from our database. Second and fourth rows: blobs rendered with user-specified perceptual Ward parameters.

Figure 2.9: *Example reflectance parameters.* Left: original photograph. Center: region to be annotated. Right: blob rendered with the user-specified perceptual Ward parameters.

(a) Unrectified synthesis (b) Rectified synthesis

Figure 2.10: *Better exemplars for texture synthesis.* (a) Synthesis using an unrectified exemplar, showing artifacts of foreshortening. (b) A texture synthesized from a rectified exemplar from our database.

(a) Target photo (b) Retextured

Figure 2.11: *Retexturing example.* The input target is a segmented photo. A rectified granite countertop surface from OpenSurfaces is synthesized and applied to the input using the correct perspective.

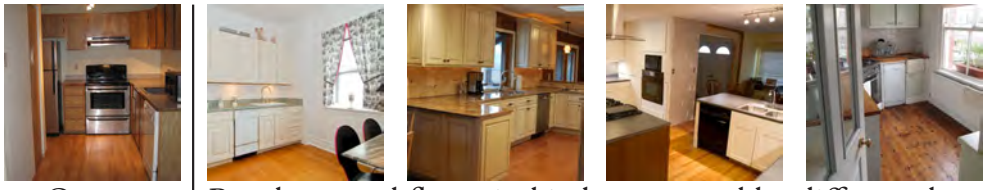

Query Results: wood floors in kitchens, sorted by diffuse color

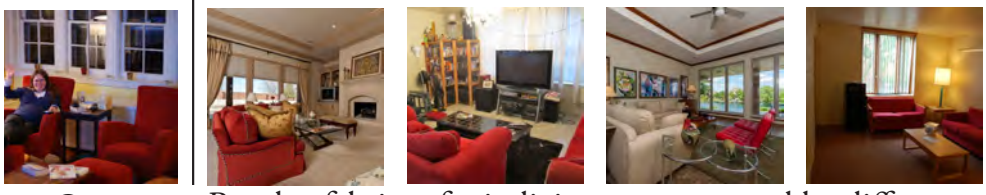

Query Results: fabric sofas in living rooms, sorted by diffuse color similarity

Figure 2.12: *Informed scene similarity.* Left: query object. Right: photos containing objects of the same name and material, sorted by diffuse color similarity to the query object.

CHAPTER 3

MATERIAL RECOGNITION IN THE WILD WITH THE MATERIALS IN CONTEXT DATABASE

3.1 Introduction

In this chapter, we leverage the OpenSurfaces platform (Chapter 2) to perform material recognition. We present a new method for collecting data that uses individual clicks to reduce the cost of acquisition. Using this data, we train a deep neural network combined with a conditional random field, to predict the material at every point in an image.

Material recognition plays a critical role in our understanding of and interactions with the world. To tell whether a surface is easy to walk on, or what kind of grip to use to pick up an object, we must recognize the materials that make up our surroundings. Automatic material recognition can be useful in a variety of applications, including robotics, product search, and image editing for interior design. But recognizing materials in real-world images is very challenging. Many categories of materials, such as fabric or wood, are visually very rich and span a diverse range of appearances. Materials can further vary in appearance due to lighting and shape. Some categories, such as plastic and ceramic, are often smooth and featureless, requiring reasoning about subtle cues or context to differentiate between them.

Large-scale datasets (e.g., ImageNet [150], SUN [194, 134] and Places [202]) combined with convolutional neural networks (CNNs) have been key to recent breakthroughs in object recognition and scene classification. Material recognition

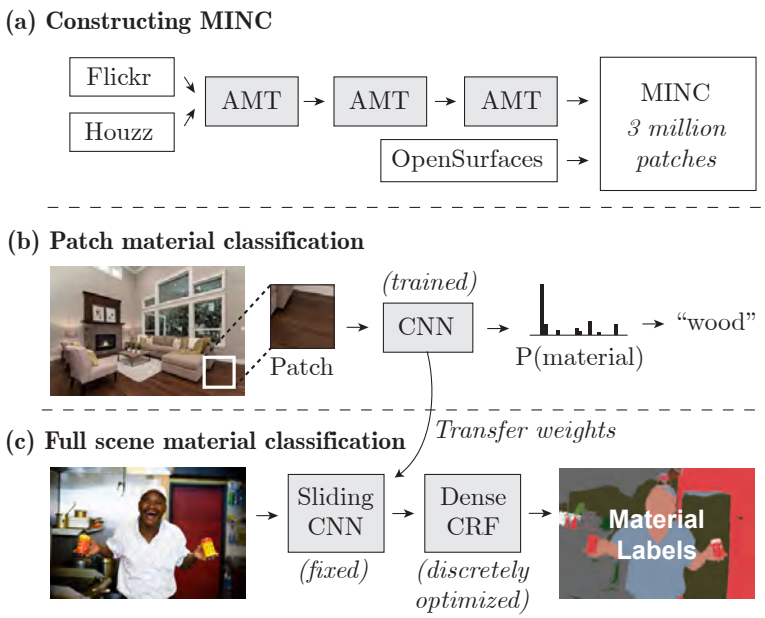

Figure 3.1: **Overview. (a)** We construct a new dataset by combining OpenSurfaces [12] with a novel three-stage Amazon Mechanical Turk (AMT) pipeline. **(b)** We train various CNNs on patches from MINC to predict material labels. **(c)** We transfer the weights to a fully convolutional CNN to efficiently generate a probability map across the image; we then use a fully connected CRF to predict the material at every pixel.

is similarly poised for advancement through large-scale data and learning. To date, progress in material recognition has been facilitated by moderate-sized datasets like the Flickr Material Database (FMD) [160]. FMD contains ten material categories, each with 100 samples drawn from Flickr photos. These images were carefully selected to illustrate a wide range of appearances for these categories. FMD has been used in research on new features and learning methods for material perception and recognition [115, 82, 139, 159]. While FMD was an important step towards material recognition, it is not sufficient for classifying materials in real-world imagery. This is due to the relatively small set of categories, the relatively small number of images per category, and also because the dataset has been designed around hand-picked iconic images of materials. The OpenSurfaces dataset [12] addresses some of these problems by introducing 105,000

material segmentations from real-world images, and is significantly larger than FMD. However, in OpenSurfaces many material categories are under-sampled, with only tens of images.

In this chapter we introduce a new, well-sampled material dataset, called the **Materials in Context Database** (MINC), with **3 million** material samples. MINC is more diverse, has more examples in less common categories, and is much larger than existing datasets. MINC draws data from both Flickr images, which include many "regular" scenes, as well as Houzz images from professional photographers of staged interiors. These sources of images each have different characteristics that together increase the range of materials that can be recognized. See Figure 3.2 for examples of our data. We make our full dataset available online at `http://minc.cs.cornell.edu/`.

We use this data for material recognition by training different CNN architectures on this new dataset. We perform experiments that illustrate the effect of network architecture, image context, and training data size on subregions (i.e., patches) of a full scene image. Further, we build on our patch classification results and demonstrate simultaneous material recognition and segmentation of an image by performing dense classification over the image with a fully connected conditional random field (CRF) model [97]. By replacing the fully connected layers of the CNN with convolutional layers [157], the computational burden is significantly lower than a naive sliding window approach.

In summary, we make two new contributions:

- We introduce a new material dataset, MINC, and 3-stage crowdsourcing pipeline for efficiently collecting millions of click labels (Section 3.3.2).

Figure 3.2: Example patches from all 23 categories of the **Materials in Context Database** (MINC). Note that we sample patches so that the patch center is the material in question (and not necessarily the entire patch). See Table 3.1 for the size of each category.

- Our new semantic segmentation method combines a fully-connected CRF with unary predictions based on CNN learned features (Section 3.4.2) for simultaneous material recognition and segmentation.

Our work in this chapter was published at CVPR 2015 [14]. The idea of solving simultaneous classification and semantic segmentation with a CNN combined with a fully-connected CRF was presented in parallel and developed independently by two other groups [30, 201]. We were the first groups to introduce this approach which is now the mainstay of most algorithms trying to solve these problems.

3.2 Prior Work

Material Databases. Much of the early work on material recognition focused on classifying specific instances of textures or material samples. For instance,

the CUReT [40] database contains 61 material samples, each captured under 205 different lighting and viewing conditions. This led to research on the task of instance-level texture or material classification [107, 182], and an appreciation of the challenges of building features that are invariant to pose and illumination. Later, databases with more diverse examples from each material category began to appear, such as KTH-TIPS [75, 24], and led explorations of how to generalize from one example of a material to another—from one sample of wood to a completely different sample, for instance. Real-world texture attributes have also recently been explored [35].

In the domain of categorical material databases, Sharan et al. released FMD [160] (described above). Subsequently, Bell et al. released OpenSurfaces [12] which contains over 20,000 real-world scenes labeled with both materials and objects, using a multi-stage crowdsourcing pipeline. Because OpenSurfaces images are drawn from consumer photos on Flickr, material samples have real-world context, in contrast to prior databases (CUReT, KTH-TIPS, FMD) which feature cropped stand-alone samples. While OpenSurfaces is a good starting point for a material database, we substantially expand it with millions of new labels.

Material recognition. Much prior work on material recognition has focused on the classification problem (categorizing an image patch into a set of material categories), often using hand-designed image features. For FMD, Liu et al. [115] introduced reflectance-based edge features in conjunction with other general image features. Hu et al. [82] proposed features based on variances of oriented gradients. Qi et al. [139] introduced a pairwise local binary pattern (LBP) feature. Li et al. [108] synthesized a dataset based on KTH-TIPS2 and built a classifier from LBP and dense SIFT. Timofte et al. [173] proposed a classification framework

with minimal parameter optimization. Schwartz and Nishino [156] introduced material traits that incorporate learned convolutional auto-encoder features. Recently, Cimpoi et al. [35] developed a CNN and improved Fisher vector (IFV) classifier that achieves state-of-the-art results on FMD and KTH-TIPS2. Finally, it has been shown that jointly predicting objects and materials can improve performance [82, 200].

Convolutional neural networks. While CNNs have been around for a few decades, with early successes such as LeNet [106], they have only recently led to state-of-the-art results in object classification and detection, leading to enormous progress. Driven by the ILSVRC challenge [150], we have seen many successful CNN architectures [197, 157, 167, 165], led by the work of Krizhevsky et al.on their SuperVision (a.k.a. AlexNet) network [99], with more recent architectures including GoogLeNet [167]. In addition to image classification, CNNs are the state-of-the-art for detection and localization of objects, with recent work including R-CNNs [66], Overfeat [157], and VGG [165]. Finally, relevant to our goal of per-pixel material segmentation, Farabet et al. [50] use a multi-scale CNN to predict the class at every pixel in a segmentation. Oquab et al. [129] employ a sliding window approach to localize patch classification of objects. We build on this body of work in deep learning to solve our problem of material recognition and segmentation.

3.3 The Materials in Context Database (MINC)

We now describe the methodology that went into building our new material database. Why a new database? We needed a dataset with the following proper-

ties:

- **Size**: It should be sufficiently large that learning methods can generalize beyond the training set.
- **Well-sampled**: Rare categories should be represented with a large number of examples.
- **Diversity**: Images should span a wide range of appearances of each material in real-world settings.
- **Number of categories**: It should contain many different materials found in the real world.

3.3.1 Sources of data

We decided to start with the public, crowdsourced OpenSurfaces dataset [12] as the seed for MINC since it is drawn from Flickr imagery of everyday, real-world scenes with reasonable diversity. Furthermore, it has a large number of categories and the most samples of all prior databases.

While OpenSurfaces data is a good start, it has a few limitations. Many categories in OpenSurfaces are not well sampled. While the largest category, *wood*, has nearly 20K samples, smaller categories, such as *water*, have only tens of examples. This imbalance is due to the way the OpenSurfaces dataset was annotated; workers on Amazon Mechanical Turk (AMT) were free to choose any material subregion to segment. Workers often gravitated towards certain common types of materials or salient objects, rather than being encouraged to label a diverse set of materials. Further, the images come from a single source (Flickr).

We decided to augment OpenSurfaces with substantially more data, especially for underrepresented material categories, with the initial goal of gathering at least 10K samples per material category. We decided to gather this data from another source of imagery, professional photos on the interior design website Houzz (`houzz.com`). Our motivation for using this different source of data was that, despite Houzz photos being more "staged" (relative to Flickr photos), they actually represent a larger variety of materials. For instance, Houzz photos contain a wide range of types of polished stone. With these sources of image data, we now describe how we gather material annotations.

3.3.2 Segments, Clicks, and Patches

What specific kinds of material annotations make for a good database? How should we collect these annotations? The type of annotations to collect is guided in large part by the tasks we wish to generate training data for. For some tasks such as scene recognition, whole-image labels can suffice [194, 202]. For object detection, labeled bounding boxes as in PASCAL are often used [49]. For segmentation or scene parsing tasks, per-pixel segmentations are required [153, 67]. Each style of annotation comes with a cost proportional to its complexity. For materials, we decided to focus on two problems, guided by prior work:

- **Patch material classification.** Given an image patch, what kind of material is it at the center?
- **Full scene material classification.** Given a full image, produce a full per-pixel segmentation and labeling. Also known as *semantic segmentation* or *scene parsing* (but in our case, focused on materials). Note that classification

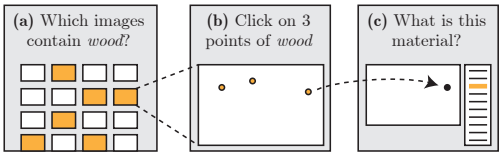

Figure 3.3: **AMT pipeline schematic for collecting clicks. (a)** Workers filter by images that contain a certain material, **(b)** workers click on materials, and **(c)** workers validate click locations by re-labeling each point. Example responses are shown in orange.

can be a component of segmentation, e.g., with sliding window approaches.

Segments. OpenSurfaces contains material segmentations—carefully drawn polygons that enclose same-material regions. To form the basis of MINC, we selected OpenSurfaces segments with high confidence (inter-worker agreement) and manually curated segments with low confidence, giving a total of 72K shapes. To better balance the categories, we manually segmented a few hundred extra samples for *sky*, *foliage* and *water*.

Since some of the OpenSurfaces categories are difficult for humans, we consolidated these categories. We found that many AMT workers could not disambiguate *stone* from *concrete*, *clear plastic* from *opaque plastic*, and *granite* from *marble*. Therefore, we merged these into *stone*, *plastic*, and *polished stone* respectively. Without this merging, many ground truth examples in these categories would be incorrect. The final list of 23 categories is shown in Table 3.1. The category *other* is different in that it was created by combining various smaller categories.

Clicks. Since we want to expand our dataset to millions of samples, we decided to augment OpenSurfaces segments by collecting *clicks*: single points in an image along with a material label, which are much cheaper and faster to collect. Figure 3.3 shows our pipeline for collecting clicks.

Initially, we tried asking workers to click on examples of a given material in a photo. However, we found that workers would get frustrated if the material was absent in too many of the photos. Thus, we added an initial first stage where workers filter out such photos. To increase the accuracy of our labels, we verify the click labels by asking different workers to specify the material for each click without providing them with the label from the previous stage.

To ensure that we obtain high quality annotations and avoid collecting labels from workers who are not making an effort, we include secret known answers (sentinels) in the first and third stages, and block workers with an accuracy below 50% and 85% respectively. We do not use sentinels in the second stage since it would require per-pixel ground truth labels, and it turned out not to be necessary. Workers generally performed all three tasks so we could identify bad workers in the first or third task.

Material clicks were collected for both OpenSurfaces images and the new Houzz images. This allowed us to use labels from OpenSurfaces to generate the sentinel data; we included 4 sentinels per task. With this streamlined pipeline we collected 2,341,473 annotations at an average cost of $0.00306 per annotation (stage 1: $0.02 / 40 images, stage 2: $0.10 / 50 images, 2, stage 3: $0.10 / 50 points).

Patches. Labeled segments and clicks form the core of MINC. For training CNNs and other types of classifiers, it is useful to have data in the form of fixed-sized patches. We convert both forms of data into a unified dataset format: square image patches. We use a *patch center* and *patch scale* (a multiplier of the smaller image dimension) to define the image subregion that makes a patch. For our patch classification experiments, we use 23.3% of the smaller image

Patches	Category	Patches	Category	Patches	Category
564,891	Wood	114,085	Polished stone	35,246	Skin
465,076	Painted	98,891	Carpet	29,616	Stone
397,982	Fabric	83,644	Leather	28,108	Ceramic
216,368	Glass	75,084	Mirror	26,103	Hair
188,491	Metal	64,454	Brick	25,498	Food
147,346	Tile	55,364	Water	23,779	Paper
142,150	Sky	39,612	Other	14,954	Wallpaper
120,957	Foliage	38,975	Plastic		

Table 3.1: **MINC patch counts by category.** Patches were created from both OpenSurfaces segments and our newly collected *clicks*. See Section 3.3.2 for details.

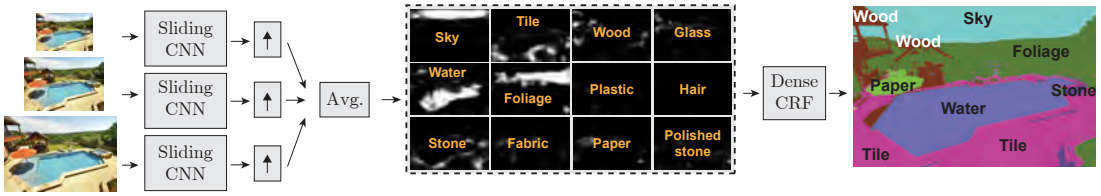

(a) Multiscale input **(b)** Probability map (12 of 23 shown) **(c)** Predicted labels

Figure 3.4: **Pipeline for full scene material classification.** An image **(a)** is resized to multiple scales $[1/\sqrt{2}, 1, \sqrt{2}]$. The same sliding CNN predicts a probability map **(b)** across the image for each scale; the results are upsampled and averaged. A fully connected CRF predicts a final label for each pixel **(c)**. This example shows predictions from a single GoogLeNet converted into a sliding CNN (no average pooling).

dimension. Increasing the patch scale provides more context but reduces the spatial resolution. Later in Section 6.6 we justify our choice with experiments that vary the patch scale for AlexNet.

We place a patch centered around each click label. For each segment, if we were to place a patch at every interior pixel then we would have a very large and redundant dataset. Therefore, we Poisson-disk subsample each segment, separating patch centers by at least 9.1% of the smaller image dimension. These segments generated 655,201 patches (an average of 9.05 patches per segment). In total, we generated 2,996,674 labeled patches from 436,749 images. Patch counts are shown in Table 3.1, and example patches from various categories are illustrated in Figure 3.2.

3.4 Material recognition in real-world images

Our goal is to train a system that recognizes the material at every pixel in an image. We split our training procedure into multiple stages and analyze the performance of the network at each stage. First, we train a CNN that produces a single prediction for a given input patch. Then, we convert the CNN into a sliding window and predict materials on a dense grid across the image. We do this at multiple scales and average to obtain a unary term. Finally, a dense CRF [97] combines the unary term with fully connected pairwise reasoning to output per-pixel material predictions. The entire system is depicted in Figure 3.1, and described more below.

3.4.1 Training procedure

MINC contains 3 million patches that we split into training, validation and test sets. Randomly splitting would result in nearly identical patches (e.g., from the same OpenSurfaces segment) being put in training and test, thus inflating the test score. To prevent correlation, we group photos into clusters of near-duplicates, then assign each cluster to one of train, validate or test. We make sure that there are at least 75 segments of each category in the test set to ensure there are enough segments to evaluate segmentation accuracy. To detect near-duplicates, we compare AlexNet CNN features computed from each photo (see the supplemental[1] for details). For exact duplicates, we discard all but one of the copies.

We train all of our CNNs by fine-tuning the network starting from the weights

[1] http://www.cs.cornell.edu/~sbell/pdf/cvpr2015-minc-supp.pdf

obtained by training on 1.2 million images from ImageNet (ILSVRC2012). When training AlexNet, we use stochastic gradient descent with batchsize 128, dropout rate 0.5, momentum 0.9, and a base learning rate of 10^{-3} that decreases by a factor of 0.25 every 50,000 iterations. For GoogLeNet, we use batchsize 69, dropout 0.4, and learning rate $\alpha_t = 10^{-4}\sqrt{1 - t/250000}$ for iteration t.

Our training set has a different number of examples per class, so we cycle through the classes and randomly sample an example from each class. Failing to properly balance the examples results in a 5.7% drop in mean class accuracy (on the validation set). Further, since it has been shown to reduce overfitting, we randomly augment samples by taking crops (227×227 out of 256×256), horizontal mirror flips, spatial scales in the range $[1/\sqrt{2}, \sqrt{2}]$, aspect ratios from 3:4 to 4:3, and amplitude shifts in $[0.95, 1.05]$. Since we are looking at local regions, we subtract a per-channel mean (R: 124, G: 117, B: 104) rather than a mean image [99].

3.4.2 Full scene material classification

Figure 3.4 shows an overview of our method for simultaneously segmenting and recognizing materials. Given a CNN that can classify individual points in the image, we convert it to a sliding window detector and densely classify a grid across the image. Specifically, we replace the last fully connected layers with convolutional layers, so that the network is fully convolutional and can classify images of any shape. After conversion, the weights are fixed and not fine-tuned. With our converted network, the strides of each layer cause the network to output a prediction every 32 pixels. We obtain predictions every 16

pixels by shifting the input image by half-strides (16 pixels). While this appears to require 4x the computation, Sermanet et al. [157] showed that the convolutions can be reused and only the pool5 through fc8 layers need to be recomputed for the half-stride shifts. Adding half-strides resulted in a minor 0.2% improvement in mean class accuracy across segments (after applying the dense CRF, described below), and about the same mean class accuracy at click locations.

The input image is resized so that a patch maps to a 256x256 square. Thus, for a network trained at patch scale s, the resized input has smaller dimension $d = 256/s$. Note that d is inversely proportional to scale, so increased context leads to lower spatial resolution. We then add padding so that the output probability map is aligned with the input when upsampled. We repeat this at 3 different scales (smaller dimension $d/\sqrt{2}$, d, $d\sqrt{2}$), upsample each output probability map with bilinear interpolation, and average the predictions. To make the next step more efficient, we upsample the output to a fixed smaller dimension of 550.

We then use the dense CRF of Krähenbühlet al. [97] to predict a label at every pixel, using the following energy:

$$E(x \mid \mathbf{I}) = \sum_i \psi_i(x_i) + \sum_{i<j} \psi_{ij}(x_i, x_j) \tag{3.1}$$

$$\psi_i(x_i) = -\log p_i(x_i) \tag{3.2}$$

$$\psi_{ij}(x_i, x_j) = w_p \, \delta(x_i \neq x_j) \, k(\mathbf{f}_i - \mathbf{f}_j) \tag{3.3}$$

where ψ_i is the unary energy (negative log of the aggregated softmax probabilities) and ψ_{ij} is the pairwise term that connects every pair of pixels in the image. We use a single pairwise term with a Potts label compatibility term δ weighted by w_p and unit Gaussian kernel k. For the features $\mathbf{f}_i$, we convert the RGB image to

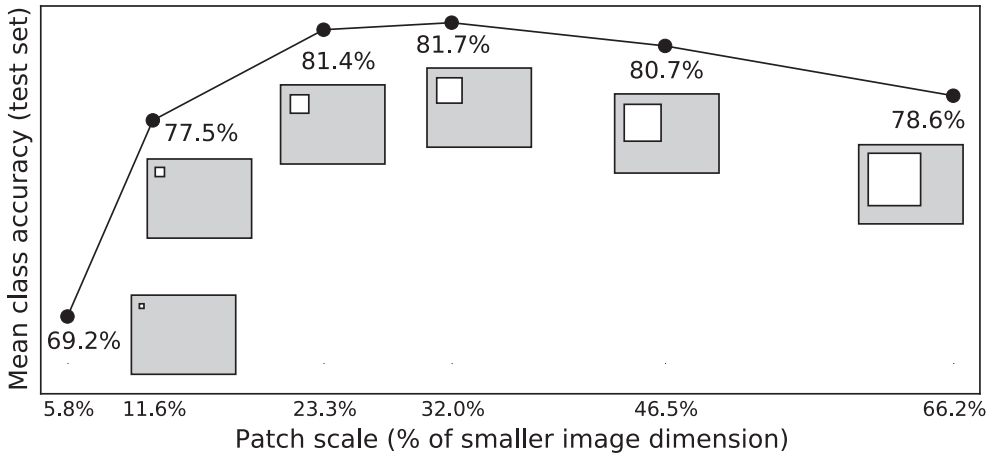

Figure 3.5: **Varying patch scale**. We train/test patches of different scales (the patch locations do not vary). The optimum is a trade-off between context and spatial resolution. CNN: AlexNet.

Architecture	Validation	Test
AlexNet [99]	82.2%	81.4%
GoogLeNet [167]	**85.9%**	**85.2%**
VGG-16 [165]	85.6%	84.8%

Table 3.2: **Patch material classification results.** Mean class accuracy for different CNNs trained on MINC. See Section 3.5.1.

$L^*a^*b^*$ and use color (I_i^L, I_i^a, I_i^b) and position (p^x, p^y) as pairwise features for each pixel: $\mathbf{f}_i = \left[\frac{p_i^x}{\theta_p d}, \frac{p_i^y}{\theta_p d}, \frac{I_i^L}{\theta_L}, \frac{I_i^a}{\theta_{ab}}, \frac{I_i^b}{\theta_{ab}}\right]$, where d is the smaller image dimension. Figure 3.4 shows an example unary term p_i and the resulting segmentation x.

3.5 Experiments and Results

3.5.1 Patch material classification

In this section, we evaluate the effect of many different design decisions for training methods for material classification and segmentation, including various CNN architectures, patch sizes, and amounts of data.

Sky	97.3%	Food	90.4%	Wallpaper	83.4%	Glass	78.5%
Hair	95.3%	Leather	88.2%	Tile	82.7%	Fabric	77.8%
Foliage	95.1%	Other	87.9%	Ceramic	82.7%	Metal	77.7%
Skin	93.9%	Pol. stone	85.8%	Stone	82.7%	Mirror	72.0%
Water	93.6%	Brick	85.1%	Paper	81.8%	Plastic	70.9%
Carpet	91.6%	Painted	84.2%	Wood	81.3%		

Table 3.3: **Patch test accuracy by category.** CNN: GoogLeNet. See the supplemental material (http://www.cs.cornell.edu/~sbell/pdf/cvpr2015-minc-supp.pdf) for a full confusion matrix.

CNN Architectures. Our ultimate goal is full material segmentation, but we are also interested in exploring which CNN architectures give the best results for classifying single patches. Among the networks and parameter variations we tried we found the best performing networks were AlexNet [99], VGG-16 [165] and GoogLeNet [167]. AlexNet and GoogLeNet are re-implementations by BVLC [85], and VGG-16 is configuration D (a 16 layer network) of [165]. All models were obtained from the Caffe Model Zoo [85]. Our experiments use AlexNet for evaluating material classification design decisions and combinations of AlexNet and GoogLeNet for evaluating material segmentation. Tables 3.2 and 3.3 summarize patch material classification results on our dataset. Figure 3.10 shows correct and incorrect predictions made with high confidence.

Input patch scale. To classify a point in an image we must decide how much context to include around it. The context, expressed as a fraction of image size, is the patch scale. A priori, it is not clear which scale is best since small patches have better spatial resolution, but large patches have more contextual information. Holding patch centers fixed we varied scale and evaluated classification accuracy with AlexNet. Results and a visualization of patch scales are shown in Figure 3.5. Scale 32% performs the best. Individual categories had peaks at middle scale with some exceptions; we find that *mirror*, *wallpaper* and *sky* improve with increasing context (Figure 3.7). We used 23.3% (which has nearly the same accuracy but

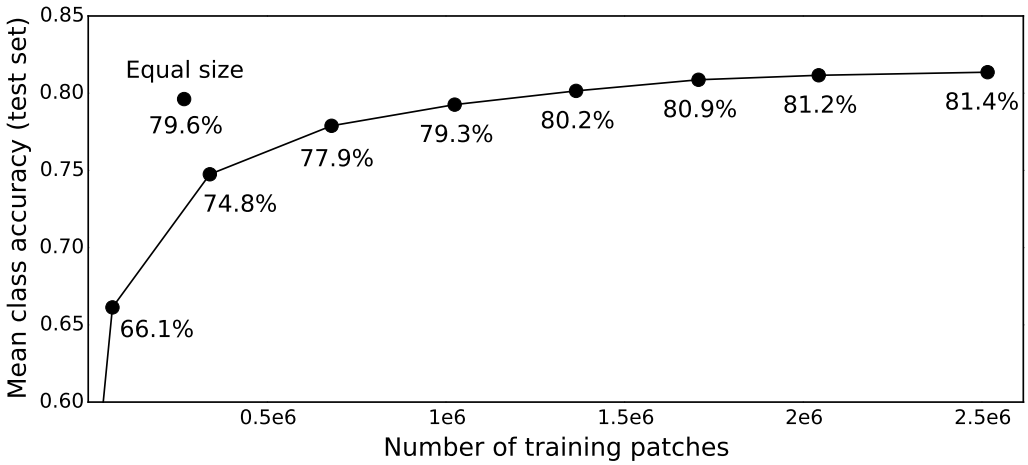

Figure 3.6: **Varying database size.** Patch accuracy when trained on random subsets of MINC. *Equal size* is using equal samples per category (size determined by smallest category). CNN: AlexNet.

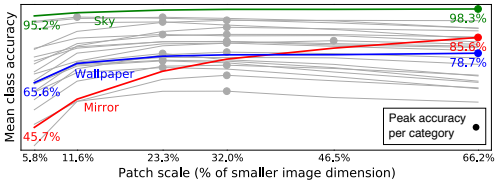

Figure 3.7: **Accuracy vs patch scale by category**. Dots: peak accuracy for each category; colored lines: *sky*, *wallpaper*, *mirror*; gray lines: other categories. CNN: AlexNet. While most materials are optimally recognized at 23.3% or 32% patch scale, recognition of *sky*, *wallpaper* and *mirror* improve with increasing context.

higher spatial resolution) for our experiments.

Dataset size. To measure the effect of size on patch classification accuracy we trained AlexNet with patches from randomly sampled subsets of all 369,104 training images and tested on our full test set (Figure 3.6). As expected, using more data improved performance. In addition, we still have not saturated performance with 2.5 million training patches; even higher accuracies may be possible with more training data (though with diminishing returns).

Dataset balance. Although we've shown that more data is better we also find that a balanced dataset is more effective. We trained AlexNet with all patches of

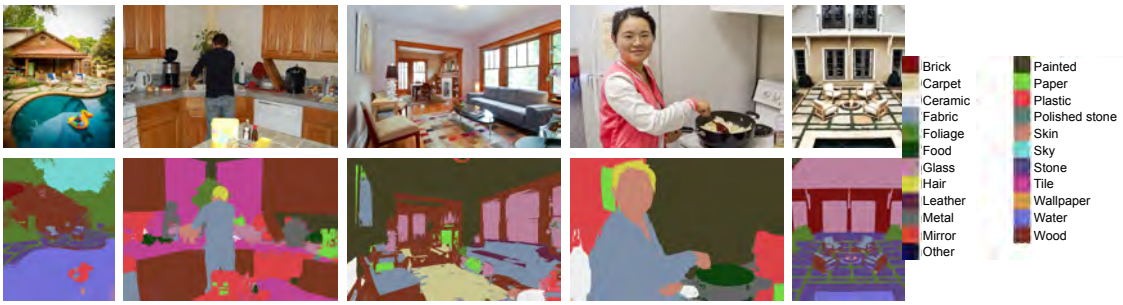

Figure 3.8: **Full-scene material classification examples:** high-accuracy test set predictions by our method. CNN: GoogLeNet (with the average pooling layer removed). Right: legend for material colors. See Table 3.4 for quantitative evaluation.

our smallest category (*wallpaper*) and randomly sampled the larger categories (the largest, *wood*, being 40x larger) to be equal size. We then measured mean class accuracy on the same full test set. As shown in Figure 3.6, "Equal size" is more accurate than a dataset of the same size and just 1.7% lower than the full training set (which is 9x larger). This result further demonstrates the value of building up datasets in a balanced manner, focusing on expanding the smallest, least common categories.

3.5.2 Full scene material segmentation

The full test set for our patch dataset contains 41,801 photos, but most of them contain only a few labels. Since we want to evaluate the per-pixel classification performance, we select a subset of 5,000 test photos such that each photo contains a large number of segments and clicks, and small categories are well sampled. We greedily solve for the best such set of photos. We similarly select 2,500 of 25,844 validation photos. Our splits for all experiments are included online with the dataset. To train the CRF for our model, we try various parameter settings (θ_p, θ_{ab}, θ_L, w_p) and select the model that performs best on the validation set. In

Input image (test set) | **(a)** Labels from CRF trained on segments | **(b)** Labels from CRF trained on clicks

Figure 3.9: **Optimizing for click accuracy leads to sloppy boundaries.** In **(a)**, we optimize for mean class accuracy across segments, resulting in high quality boundaries. In **(b)**, we optimize for mean class accuracy at click locations. Since the clicks are not necessarily close to object boundaries, there is no penalty for sloppy boundaries. CNN: GoogLeNet (without average pooling).

total, we evaluate 1799 combinations of CNNs and CRF parameters. See the supplemental material[2] for a detailed breakdown.

We evaluate multiple versions of GoogLeNet: both the original architecture and a version with the average pooling layer (at the end) changed to 5x5, 3x3, and 1x1 (i.e. no average pooling). We evaluate AlexNet trained at multiple patch scales (Figure 3.5). When using an AlexNet trained at a different scale, we keep the same scale for testing. We also experiment with ensembles of GoogLeNet and AlexNet, combined with either arithmetic or geometric mean.

Since we have two types of data, *clicks* and *segments*, we run two sets of experiments: (a) we train and test only on segments, and in a separate experiment (b) we train and test only on clicks. These two training objectives result in very

[2] http://www.cs.cornell.edu/~sbell/pdf/cvpr2015-minc-supp.pdf

Architecture		**(a)** Segments only		**(b)** Clicks only	
		Class	Total	Class	Total
AlexNet	Scale: 11.6%	64.3%	72.6%	79.9%	77.2%
AlexNet	Scale: 23.3%	69.6%	76.6%	**83.3%**	**81.1%**
AlexNet	Scale: 32.0%	**70.1%**	**77.1%**	83.2%	80.7%
AlexNet	Scale: 46.5%	69.6%	75.4%	80.8%	77.7%
AlexNet	Scale: 66.2%	67.7%	72.0%	77.2%	72.6%
GoogLeNet	7x7 avg. pool	64.4%	71.6%	63.6%	63.4%
GoogLeNet	5x5 avg. pool	67.6%	74.6%	70.9%	69.8%
GoogLeNet	3x3 avg. pool	**70.4%**	77.7%	76.1%	74.7%
GoogLeNet	No avg. pool	**70.4%**	**78.8%**	**79.1%**	**77.4%**
Ensemble	2 CNNs	**73.1%**	**79.8%**	84.5%	83.1%
Ensemble	3 CNNs	**73.1%**	79.3%	**85.9%**	**83.5%**
Ensemble	4 CNNs	72.1%	78.4%	85.8%	83.2%
Ensemble	5 CNNs	71.7%	78.3%	85.5%	83.2%

Table 3.4: **Full scene material classification results.** Mean class and total accuracy on the test set. When training, we optimize the CRF parameters for mean class accuracy, but report both mean class and total accuracy (mean accuracy across all examples). In one experiment **(a)**, we train and test only on segments; in a separate experiment **(b)**, we train and test only on clicks. Accuracies for segments are averaged across all pixels that fall in that segment.

different behavior, as illustrated in Figure 3.9. In experiment (a), the accuracy across segments are optimized, producing clean boundaries. In experiment (b), the CRF maximizes accuracy only at click locations, thus resulting in sloppy boundaries. As shown in Table 3.4, the numerical scores for the two experiments are also very different: segments are more challenging than clicks. While clicks are sufficient to train a CNN, they are not sufficient to train a CRF.

Focusing on segmentation accuracy, we see from Table 3.4(a) that our best single model is GoogLeNet without average pooling (6% better than with pooling). The best ensemble is 2 CNNs: GoogLeNet (no average pooling) and AlexNet (patch scale: 46.5%), combined with arithmetic mean. Larger ensembles perform worse since we are averaging worse CNNs. In Figure 3.8, we show example labeling results on test images.

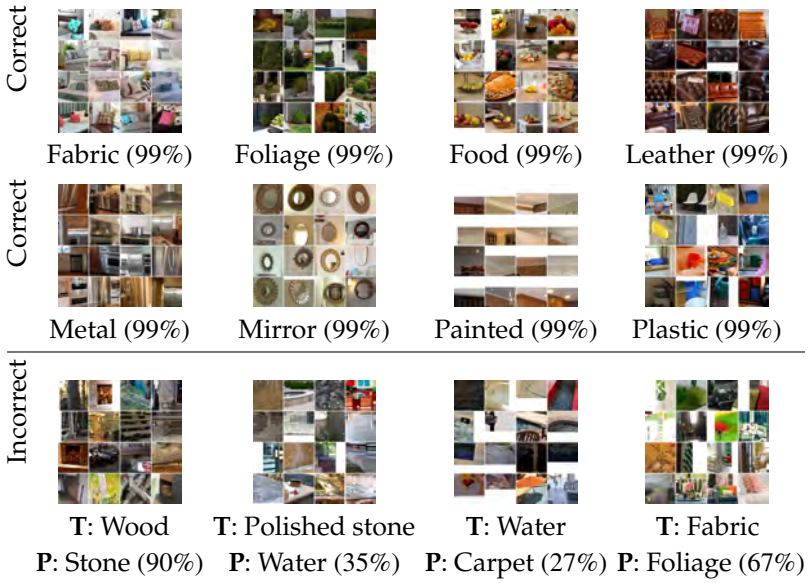

Figure 3.10: **High confidence predictions.** Top two rows: correct predictions. Bottom row: incorrect predictions (**T**: true, **P**: predicted). Percentages indicate confidence (the predictions shown are at least this confident). CNN: GoogLeNet.

3.5.3 Comparing MINC to FMD

Compared to FMD, the size and diversity of MINC is valuable for classifying real-world imagery. Table 3.5 shows the effect of training on all of FMD and testing on MINC (and vice versa). The results suggests that training on FMD alone is not sufficient for real-world classification. Though it may seem that our dataset is "easy," since the best classifications scores are lower for FMD than for MINC, we find that difficulty is in fact closely tied to dataset size (Section 3.5.1). Taking 100 random samples per category, AlexNet achieves 54.2 ± 0.7% on MINC (64.6 ± 1.3% when considering only the 10 FMD categories) and 66.5% on FMD.

		Test		
		FMD	MINC	*(10 categories in common)*
Train	FMD	66.5%	26.1%	
	MINC	41.7%	85.0%	

Table 3.5: **Cross-dataset experiments.** We train on one dataset and test on another dataset. Since MINC contains 23 categories, we limit MINC to the 10 categories in common. CNN: AlexNet.

Method	**Accuracy**	**Trials**
Sharan et al. [159]	57.1 ± 0.6%	14 splits
Cimpoi et al. [35]	67.1 ± 0.4%	14 splits
Fine-tuned AlexNet	66.5 ± 1.5%	5 folds
SIFT_IFV+fc7	**69.6 ± 0.3%**	10 splits

Table 3.6: **FMD experiments.** By replacing DeCAF features with oversampled AlexNet features we improve on the best FMD result.

3.5.4 Comparing CNNs with prior methods

Cimpoi [35] is the best prior material classification method on FMD. We find that by replacing DeCAF with oversampled AlexNet features we can improve on their FMD results. We then show that on MINC, a finetuned CNN is even better.

To improve on [35], we take their SIFT_IFV, combine it with AlexNet fc7 features, and add oversampling [99] (see supplemental[3] for details). With a linear SVM we achieve 69.6 ± 0.3% on FMD. Previous results are listed in Table 3.6.

Having found that SIFT_IFV+fc7 is the new best on FMD, we compare it to a finetuned CNN on a subset of MINC (2500 patches per category, one patch per photo). Fine-tuning AlexNet achieves 76.0 ± 0.2% whereas SIFT_IFV+fc7 achieves 67.4 ± 0.5% with a linear SVM (oversampling, 5 splits). This experiment shows that a finetuned CNN is a better method for MINC than SIFT_IFV+fc7.

[3] http://www.cs.cornell.edu/~sbell/pdf/cvpr2015-minc-supp.pdf

3.6 Conclusion

Material recognition is a long-standing, challenging problem. We introduce a new large, open, material database, MINC, that includes a diverse range of materials of everyday scenes and staged designed interiors, and is at least an order of magnitude larger than prior databases. Using this large database we conduct an evaluation of recent deep learning algorithms for simultaneous material classification and segmentation, and achieve results that surpass prior attempts at material recognition.

Some lessons we have learned are:

- Training on a dataset which includes the surrounding context is crucial for real-world material classification.
- Labeled clicks are cheap and sufficient to train a CNN alone. However, to obtain high quality segmentation results, training a CRF on polygons results in much better boundaries than training on clicks.

Many future avenues of work remain. Expanding the dataset to a broader range of categories will require new ways to mine images that have more variety, and new annotation tasks that are cost-effective. Inspired by attributes for textures [35], in the future we would like to identify material attributes and expand our database to include them. We also believe that further exploration of joint material and object classification and segmentation will be fruitful [82] and lead to improvements in both tasks. Our database, trained models, and all experimental results are available online at `http://minc.cs.cornell.edu/`.

3.7 Impact

Our work in this chapter was published at CVPR 2015 [14]. Our approach of using "click" labels to train semantic segmentation algorithms was later shown to yield a large improvement for objects, resulting in the most accurate models given a fixed annotation budget, out of squiggle-level, point-click, and full-image supervision [9]. Further, our MINC database has been used to train new state-of-the-art material recognition algorithms that go beyond the fully-connected CRF algorithm of Krähenbühl et al. [98] by directly learning pairwise potentials [83] or using "bilateral inceptions" [55]. Others have used our data to integrate multiple features obtained by different CNNs, obtaining close to human performance on the Flickr Material Dataset [160] with transfer learning [198].

CHAPTER 4

INTRINSIC IMAGES IN THE WILD

4.1 Introduction

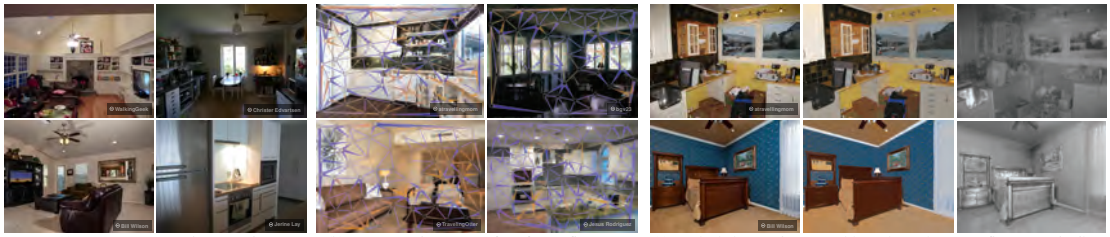

(a) 5000+ Internet photographs (b) Human judgements of surface reflectance (c) Intrinsic image decompositions: input image, reflectance, shading

Figure 4.1: We introduce a public dataset of indoor scenes for intrinsic images in the wild (a). (b) Our crowdsourcing pipeline lets users annotate pairs of points in each image with relative reflectance judgements. (c) Our intrinsic image decomposition algorithm performs well in respecting the human judgements and is based on a fully-connected conditional random field (CRF) that incorporates long-range interactions in the reflectance layer while simultaneously maintaining local detail. All source images are licensed under Creative Commons (cc).

There are many different levels of visual abstraction. In Chapters 2 and 3 we developed datasets and algorithms for labeling surface properties, with a focus on materials. In this chapter, we consider a lower-level visual problem, estimating the amount of light reflected by surfaces for photos in the wild, known as the "intrinsic images" problem. For this problem, we introduce both a new large-scale dataset and state-of-the-art method. Our main insight is that we can ask people to make *relative* judgements in images to obtain the properties we need. We use this to build up a dataset that would not otherwise be possible. We use our data to validate a new algorithm that reasons globally about an image, producing higher quality decompositions than previously possible.

Intrinsic image decomposition is a long-standing inverse problem with many applications in graphics and vision [104]. The goal of intrinsic images is to

separate an image into two layers, a reflectance (albedo) image and a shading (irradiance) image, which multiply to form the original image. Reliable algorithms for separating illumination from reflectance in scenes would enable a range of applications, such as image-based resurfacing, texture transfer between images, relighting, material recognition, and other interior design tasks. There has been significant recent progress on the problem of intrinsic image decomposition, aided by the release of the MIT Intrinsic Images dataset [69], which contains carefully constructed ground truth for images of objects. However, intrinsic image decomposition is still very challenging, especially on images of real-world *scenes*. There is currently no standard dataset for evaluating intrinsic images on images of such scenes, due in part to the challenge of capturing real-world photos with known ground truth reflectance and illumination. To span the rich range of real-world scenes we need a large set of images. For this scenario, both careful measurement (as in [69]) and using rendered images of synthetic scenes are not practical or satisfactory. Instead, to cover a rich variety of real-world conditions, we select thousands of images from public photo collections [13] and leverage human perception by turning to crowdsourcing to collect material annotations for each image.

We present a new, large-scale database of *Intrinsic Images in the Wild*—real-world photos of indoor scenes, with crowdsourced annotations of reflectance comparisons between points in a scene. Rather than creating per-pixel (absolute) annotations, we designed a scalable approach to human annotation involving humans reasoning about the relative reflectance of *pairs* of pixels in each image. This dataset is the first of its kind for intrinsic images, both in its scale and in its use of human annotation: the dataset contains over 5,000 images featuring a wide variety of scenes, and has been annotated with millions of individual

reflectance comparisons (on average 100 judgements per image). This makes our dataset several orders of magnitude larger than existing intrinsic image datasets. In addition, we include a dataset of about 400 images with a dense set of annotations (on average 900 per image). Figure 4.1 illustrates our dataset, including the pairwise comparisons we collect (Figure 4.1(b)).

Motivated by our new dataset, we have also created a new intrinsic image decomposition algorithm designed for images of real-world scenes. Our algorithm makes use of the fact that many surfaces in indoor scenes share the same material and reflectance, resulting in *long-range* sharing of reflectances across a scene (for example, a painted wall spanning an entire image). We build on recent work in fully connected conditional random field (CRF) inference [98] to enable such long-range connections in our algorithm. We evaluate our method on our new benchmark, and show that it outperforms several state-of-the-art algorithms.

In summary, our contributions are:

- A new, large-scale dataset for intrinsic images annotated via crowdsourcing that includes more than 5,000 images. This dataset is completely open and public, including both images and annotations, with the aim of enabling others to design and evaluate new algorithms for scene-level intrinsic images.
- A new intrinsic images algorithm based on a dense CRF formulation that considers long-range material relations to achieve better decomposition on our new database.

We evaluate our new algorithm, as well as a suite of other public intrinsic image algorithms, on our dataset. For each algorithm, we perform extensive cross-

validation to find the optimal parameters on our dataset, and find that our new algorithm outperforms these recent algorithms. Nonetheless, intrinsic image decomposition for real-world scenes of this complexity remains a challenging problem, with much room for improvement. We release our database of images and annotations to help drive future research in this problem.

4.2 Related work

Intrinsic images. Intrinsic image decomposition has a rich history in computer graphics and vision, and has been studied since the 1970s. One of the earliest observations is that large discontinuities in image intensity correspond to changes in reflectance, and all other variations are due mostly to changes in shading [104]. This led to the Retinex algorithm in which each image gradient is classified as belonging to either the reflectance layer or the shading layer according to its magnitude. The resulting decomposition is obtained by solving for the pair of layers whose gradients best match these classified gradients. Nearly forty years later, a version of this algorithm was the best performing on the MIT Intrinsic Images dataset [69]. Subsequent algorithms perform much better on this dataset, as described below.

Many others ideas have been proposed to solve the problem. Some recent techniques use classifiers trained on local grayscale patterns [170, 169], priors on texture statistics [126, 117], complex priors on shape, albedo, and illumination [6, 5, 8], meso- and macro-scales of shading [110], chromaticity segmentation [57], sparse sets of basis reflectances [128, 58], non-local texture constraints [163, 199], and red-black wavelets [164].

Further, many methods have been proposed that require additional input to solve the problem. With user interaction, Bousseau [19] showed that a very high-quality decomposition can be obtained, and Carroll [25] showed that diffuse interreflections can be separated. Others have addressed the problem using additional photos of the same scene either registered as an image stack [189, 74], or taken from different angles (enabling additional 3D reasoning) [70, 102, 101]. Finally, recent methods have been proposed for RGB-D (Kinect-style) imagery [7, 31]. In contrast, our paper is focused on completely automated methods that work on a single image.

Crowdsourcing. Recently many authors have shown how to effectively gather high-quality data from workers online in an economical and scalable way. Many types of problems have been addressed this way, including: acquiring material and object labels [13], solving micro-problems with humans in the loop [62], labeling parts and attributes of birds [22], evaluating image retargeting [148], and using gauge figures for understanding shape perception [38]. Additionally, many studies of worker dynamics have guided the design of tasks in this space, such as modeling workers with a confusion matrix [41] or with multidimensional classifiers that incorporate notions of user competence, bias, and expertise (CUBAM model) [190].

Intrinsic images databases. Our goal is to scale to the wide diversity of scenes in the real world in various lighting situations, and to acquire "ground truth" data for such scenes. One could create such a dataset in a few different ways. The MIT Intrinsic Images dataset [69] captured images of single objects and rigorously acquired irradiance by spray painting the objects for diffuse measurements. However, this approach does not scale to large numbers of scenes in the wild.

Another approach is to render synthetic scenes along with their reflectance and illumination (as has been done in prior work on a few test scenes, or on CG movie sequences [31]); but these approaches are constrained by the availability of models that span the range of real world materials, lightings and scenes. Instead, we chose to use human judgements as our ground truth data.

4.3 Database

We designed a crowdsourcing pipeline where human subjects (on Amazon Mechanical Turk (AMT)) report which of two points in an image has a darker surface reflectance. Our pipeline (shown in Figure 4.2) scales to millions of human judgements across thousands of real-world images. We aimed to produce a dataset that was broad enough to draw conclusions about intrinsic image algorithms. To design this pipeline we needed to address several questions:

- What judgements should the human annotators make?
- Which images and points should we show each user?
- How to present tasks to the user in an intuitive interface?
- How to identify users who are correctly performing the task and how to aggregate accurate judgements across users?

4.3.1 What judgements should we collect?

We would ideally collect ground truth reflectance information for each point in an image. However, there are several challenges in collecting such information

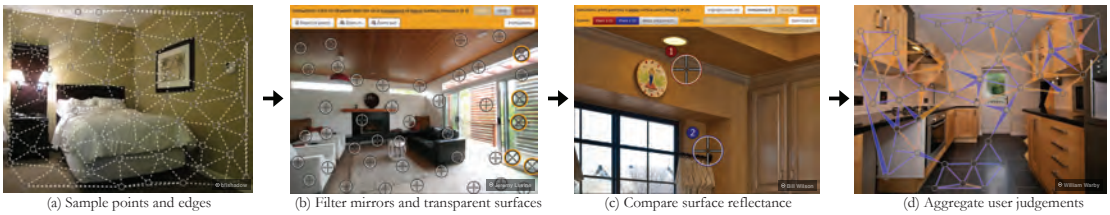
(a) Sample points and edges (b) Filter mirrors and transparent surfaces (c) Compare surface reflectance (d) Aggregate user judgements

Figure 4.2: *Our data collection pipeline.* (a) We sample points and edges from over 5,000 photographs, (b) workers flag points on mirrors and transparent surfaces, (c) users judge pairs of points and indicate which point has a darker surface reflectance (or if they are equal), and (d) we aggregate judgements from 5 users for each pair of points (each edge is styled according to the aggregate results, as described in Figure 4.3).

in a crowdsourced setting that guided how we collected judgements. A key issue is that humans are not good at making absolute judgements about illumination intensity or albedo, though they are reasonably accurate at *relative* judgements. Thus, we decided to ask humans to compare pairs of points in an image, rather than judge individual points. Asking for humans to judge *every* pair in an image is prohibitively expensive, so instead we gather judgements for pairs of sparsely sampled points (though we experiment with different densities, as described below). Another key issue is what question to ask of users—for instance, do we ask them to compare relative illumination at a pair of points, or relative surface albedo/material? We considered asking for illumination judgements (e.g., "which point is more in shadow?") but decided against this, because explicit questions about illumination are challenging for humans [131]. Hence, we decided to ask for material comparisons for pairs of points. We found that it was important to ask this question in the right way, as phrasing is often key for crowdsourced tasks, and material questions are particularly challenging for novices. We considered various possibilities and phrasings and finally settled on showing users pairs of points and asking them "which point has a darker surface color?" To make sure that workers understand our task, we instruct new workers with an interactive tutorial (described later).

4.3.2 Which images and which pairs of points?

Given the task described above, we next had to select our images and the points in each image for which we collect annotations.

Images. Our goal was to assemble a broad collection of images from the real world that are representative and free from image editing and other filters. We chose images from the OpenSurfaces dataset [13], which were gathered from Flickr and contain a variety of indoor scenes (kitchens, living rooms, bedrooms, and so on). We manually curated photos to remove images that do not represent how the world looks to the naked eye, with effects such as blur, excessive defocus, high noise, depth-of-field, fisheye, poor exposure, black-and-white, visible vignetting, washed out colors, infrared filters, distorted color tones, long-exposure effects, visible HDR artifacts, stitched panoramas, text overlays, and extra borders.

Points. Next, we must decide which points in each image to compare. To achieve good image coverage, and since it can be difficult to reason about the relative diffuse reflectance of points that are far apart in an image, we select points that are approximately equally spaced. In particular, we sample image points using Poisson disk sampling with a minimum radius (we use 7% of the image diameter).

Since we are sampling points that could lie on reflectance discontinuities, we remove potentially difficult judgements from the initial set of Poisson-disk-sampled points. Specifically, we remove (a) points within 4 pixels of a strong edge (as determined with a Canny edge detector), (b) over- or under-saturated

points (removing points where $(r+g+b)/3 < 0.02$ or > 0.98) and (c) points whose local neighborhoods have significant variance in color (removing points where the coefficient of variation of chromaticity within a 9×9 pixel window is above 0.5).[1]

Finally, we chose to exclude points where the concept of diffuse reflectance is not well-defined, in particular, points with transparent or mirror-like appearance. We filtered out such points using a separate user task run as a preprocess on the set of points (see Figure 4.2(b)).

Pairs of points. Now that we have a list of candidate points in an image, we want to choose a set of pairs of points to compare. Since we are asking users the question: "which point has a darker surface color?", we want the points to have similar chromaticity, so that the surface reflectance intensity can be easily compared. We also do not want to sample all $O(n^2)$ pairs of points in each image, since this would lead to excessive redundancy and over 1,000 pairs per photo (which is expensive to annotate for all images). Instead, we compute a Delaunay triangulation of the points, then reject edges of this triangulation where the difference in chromaticity between the point pair is too high (pairs where the Euclidean distance between points in $[r, g, b]/(r + g + b)$ chromaticity space is > 0.125).

After removing these edges, we go back and try to add new edges, by considering all possible edges that do not intersect existing edges and are within our chromaticity threshold. We greedily add such edges, starting from the shortest edge in the set, skipping edges that intersect an existing edge. Finally, we delete

[1]The coefficient of variation is a "normalized" measure of variance computed as the sample standard deviation over the mean.

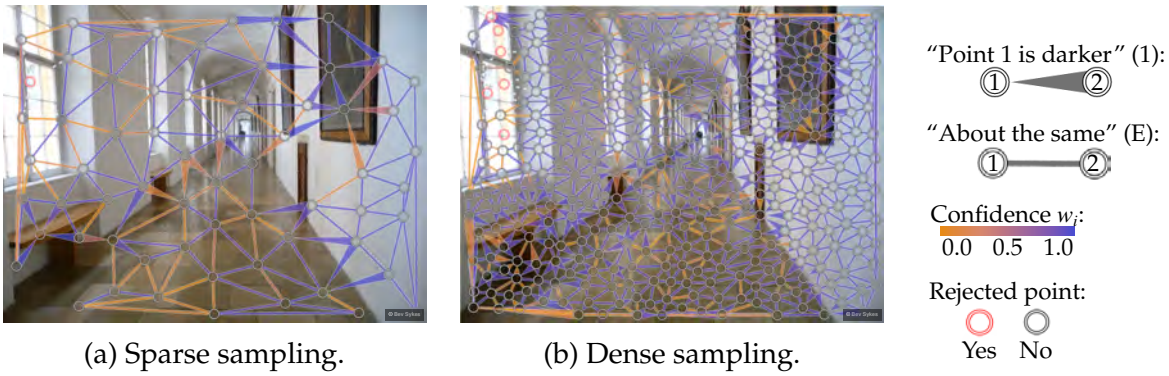

(a) Sparse sampling. (b) Dense sampling.

Figure 4.3: *Aggregated human judgements for an example scene.* The edges connecting points indicate the aggregated reflectance judgement comparing the two points. We sample points at two different densities: (a) sparsely, at 7% of the image width and (b) densely, at 3%.

any edge that is not part of a cycle; edges in cycles can be cross-checked against each other, allowing us to verify consistency of edges during our subsequent data analysis. On average, the above process results in 44 ± 16 points and 106 ± 45 pairs per image.

Dense sampling. To understand the effect of image scale on human comparisons, we created another set of more densely sampled edges on a subset of images. In particular, we selected about 400 whitebalanced photos and sampled points with a Poisson-disk sampling radius of 3% of the image diameter. Of the set of whitebalanced photos, we selected about 200 from images that had the most edges discarded by our chromaticity threshold, 100 photos at random, and a final 100 from photos where intrinsic image algorithms perform poorly (according to our metric described in Section 4.3.5). For these denser points, we do not threshold edges based on image chromaticity, as nearby points tend to be on the same object, and are thus easier to judge. Figure 4.3 shows example sparse and dense points.

4.3.3 Annotation interface

Our user interface for collecting annotations, shown in Figure 4.2(c), shows the user an image and asks them, for a particular pair of pixels (indicated with crosshairs and labeled Points 1 and 2), which of the two points has a darker surface color. The user can then select one of three options: **Point 1**, **Point 2**, and **About the same**. We ask users to specify their confidence in their assessment as **Guessing**, **Probably**, or **Definitely**, as was done by [22].

Tutorial. While humans are skilled at brightness and color constancy—i.e., discounting lighting when comparing surface reflectance (across a range of typical illumination conditions)—they are not used to explicitly thinking about this effect. We found that if one asks users to compare surface color and ignore lighting, a sizeable portion (almost half) of workers misunderstand the task as "which image pixel is darker?". We were able to reduce this proportion to about 25% by adding a tutorial which explains exactly the distinction between pixel intensity difference and surface reflectance difference. The tutorial then presents several test scenes and provides feedback and the correct answer if the worker makes a mistake. We chose difficult test scenes that force users to understand concepts such as: local highlights do not affect surface reflectance, and viewing the scene as a whole is sometimes necessary to visually comprehend and compare reflectance. The tutorial we developed is shown in the video and included on our website.[2]

Efficient input. Since users are to provide thousands of answers, we designed an interface that allows for rapid input. For each photo, our interface displays the

[2] `http://intrinsic.cs.cornell.edu/`

photo in its entirety, pauses for 1 second, and then zooms to show a pair of points. Once the user indicates their answer for that pair, the interface smoothly zooms to the next pair of points. We use van Wijk smooth zooming [180] (implemented by D3 [18]) to quickly show the next pair of points. At any time, users can zoom in/out, pan around the image, or repeat the zoom animation and have the points flash to make them easier to see. Users can also return to the previous pair and enter a new answer.

Users had unanimously positive feedback regarding our task UI:

- "Fun. It's exactly what I wish there was more of on MTurk as far as image categorization/similar HITs go."
- "This task is very well-designed and easy to understand and complete. The zoom function is quite helpful."
- "These are addicting as all hell."

Mirror and transparent surfaces. Prior to asking users to judge relative surface reflectance, we filter points through an initial stage in which users flag points as being either on a mirror or on a transparent surface (Figure 4.2(b)). As with our comparison task, a tutorial explains the types of surfaces we want filtered and lets users practice. See the video[3] for more illustrations of our two user interfaces.

[3] `http://intrinsic.cs.cornell.edu/`

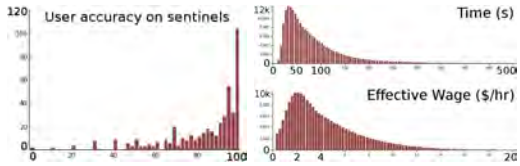

Figure 4.4: *Histograms of worker performance (left) and time spent (right).* Vertical axis on both plots: number of users. Left: percentage of sentinel data answered correctly. Right: time spent and effective wage (pay per task / time spent).

4.3.4 Data verification

After showing a pair of surface points to multiple workers, we want to classify that pair into one of three categories: (1) Point 1 has a darker reflectance than Point 2, (2) Point 2 has a darker reflectance than Point 1, and (3) they have approximately the same reflectance. We could do simple majority voting on the user-provided input to determine the category; however, consistent with other work on crowdsourcing, we found that the raw input is too noisy for this simple approach to work well.

On Mechanical Turk, there are thousands of workers of varying skill. While we believe that almost all the workers are capable of performing the task, we found that a significant fraction of workers (about 31%, based on our analysis below) either did not try to do the task correctly, or did not understand the instructions, even after the tutorial where they can try out the task and receive feedback explaining the correct answer. To address this problem, we take three steps to ensure high-quality data: (1) we replicate every task (i.e., each pair of points) to at least 5 workers, (2) we insert "sentinel" objects with known answers into each task, and (3) we use the CUBAM machine learning algorithm [190] to automatically model user competence and bias when computing consensus labels.

Sentinels. Inspired by the microtasks work of Gingold, et al. [62], each of our tasks (also known as a "HIT" on AMT) contains 25 comparisons plus 5 "sentinel" comparisons drawn from a set of known answers. To hide which items are sentinels, our server dynamically selects 5 test items that the worker has not seen before. As a user submits tasks, we measure their accuracy on the sentinels. The moment a user makes at least 5 mistakes *and* has an average accuracy below 80%, that user is blocked from performing the task. We add the test for average accuracy to avoid prematurely blocking users. When a given user has seen all test items, we stop serving the 5 extra comparisons, as the user has proven to be accurate enough on all sentinels. We chose to test a user across HITs, rather than including a large amount of sentinel items inside each HIT since we found that workers maintain approximately the same accuracy between submissions. This wastes less resources ensuring that workers are behaving correctly. Figure 4.4 shows the distribution of worker scores on sentinel items. With this method, about 31% of users were blocked. Users seemed appreciative of the fact that the effective pay increased after the sentinels were finished, and we only identified a single user who passed our tests and later began submitting random answers (some time after the sentinels finished).

Modeling workers. Once we have filtered out users who are not correctly performing the task, we must aggregate the reliable answers to obtain a single judgement J_i for each pair of points. Since some comparisons can be genuinely ambiguous, we would like to assign a confidence (or weight) w_i to each judgement J_i. Further, different users may have different competence and internal thresholds when comparing surface reflectances, and we would like to compensate for these effects. The CUBAM user model [190] lends itself to these issues, but requires that the questions have binary answers, while our judgements have

3 possible answers ("Point 1", "Point 2", "About the same"). However, we can convert our 3-class answers into two binary answers by imagining that users are making the following decisions in a small decision tree:

1. Do the two points have the same reflectance?
2. If not, does the darker point have a darker surface reflectance?

For example, a response of "Point 1" is converted to ("No", "No"), if Point 2 is darker than Point 1. Given this conversion, we solve for the most likely competence and threshold for each user and the most likely binary response for each decision using CUBAM. Thus, for each pair of points, we are able to model two forms of user bias: decision (1) models how similar two surfaces have to be before the user considers them to be the same, and decision (2) models whether the user confuses reflectance and image intensity by indicating that points in shade always have a darker reflectance.

To simplify notation, we denote the two points as "D" (darker pixel) and "L" (lighter pixel). We use luminance for this step (CIELAB) since we want to capture human perception. For example, in Figure 4.5, point L has a darker surface reflectance and thus the correct judgement for this pair is J_i = L.

Figure 4.5: Points on a fabric surface with a cast shadow.

Given the two-decision model of each comparison, we use CUBAM to compute a score for each decision, where a score of 0 indicates ambiguous, +1 is strong "yes", and −1 is strong "no". If we let $c_{i,1}$ and $c_{i,2}$ be the CUBAM scores for the i^{th} user judgement for our two decisions above, we use the distance from 0 as our

confidence/weight w_i for judgement J_i:

$$(J_i, w_i) = \begin{cases} (\mathrm{E}, c_{i,1}) & \text{if } c_{i,1} > 0 \\ (\mathrm{D}, c_{i,2}) & \text{if } c_{i,1} \leq 0 \text{ and } c_{i,2} > 0 \\ (\mathrm{L}, -c_{i,2}) & \text{else} \end{cases} \tag{4.1}$$

where E indicates that users judge the points to have equal or "about the same" reflectance intensity. Finally, we map the judgements from {E, L, D} to the original set of possible answers {E, 1, 2}.

Running the experiment. As workers were performing tasks, we periodically reviewed subsets of the aggregated answers. Whenever we decided that the aggregated answer for an unambiguous comparison was incorrect, we corrected the comparison, excluded it from future aggregation with CUBAM, and added it to our set of sentinel test items. This ensures that our sentinel items are difficult—i.e., discriminative in selecting workers who are not trying very hard. This strategy is similar to "hard negative mining" used in machine learning [51] (the idea of using hard examples to train good classifiers).

To fairly compensate workers, we approved all submissions instantly (even those performed incorrectly). We were surprised to discover that this strategy roughly doubled the number of simultaneous workers for the same rate of pay. Users were very appreciative of the fast and certain approval.

4.3.5 Error metric: WHDR

In order to use our judgements to evaluate intrinsic image decompositions, we need a way to numerically evaluate a decomposition (R, S) given judgements

J_i and weights w_i. We propose a new metric, the "weighted human disagreement rate" (WHDR), which measures the percent of human judgements that an algorithm disagrees with, weighted by the confidence of each judgement:

$$\text{WHDR}_\delta(J, R) = \frac{\sum_i w_i \cdot \mathbf{1}\left(J_i \neq \hat{J}_{i,\delta}(R)\right)}{\sum_i w_i} \tag{4.2}$$

where R is the algorithm output reflectance layer, $\mathbf{1}(\cdot)$ is the unit indicator, $\hat{J}_{i,\delta}$ is the judgement predicted by the algorithm being evaluated, and δ is the relative difference between two surface reflectances where people *just* begin to switch between saying "they are about the same" (E) to "one point is darker" (1 or 2). To transform the algorithm reflectance layer R into the same units as the judgements (answers in the set $\{1, 2, \text{E}\}$), we must threshold differences between the points used in the human judgement in the reflectance layer R. Because R is only defined up to a scale factor, we compare two reflectances using their ratio, as:

$$\hat{J}_{i,\delta}(R) = \begin{cases} 1 & \text{if } R_{2,i}/R_{1,i} > 1 + \delta \\ 2 & \text{if } R_{1,i}/R_{2,i} > 1 + \delta \\ \text{E} & \text{else} \end{cases} \tag{4.3}$$

where $R_{1,i}$ is the reflectance sampled at point 1 for the i^{th} judgement (and similarly for $R_{2,i}$). For all of our results, we set $\delta = 10\%$.

4.3.6 Discussion and results

Using our AMT pipeline, we obtained 4,880,372 responses from 1,381 workers which we aggregated to obtain 875,833 comparisons across 5,230 photos. Of these, 397 photos were also sampled at a higher density to obtain 358,293 comparisons. In Figure 4.3, we show example aggregated judgements, where directed edges

indicate which point is darker, blue/orange edges have high/low confidence, and red points are on a mirror or transparent surface.

Judgement self-consistency. Since we discarded edges that are not part of cycles, we can estimate the self-consistency of our dataset by measuring the fraction of triangles that are consistent (e.g., inequalities $\{R_1 > R_2, R_2 > R_3, R_3 > R_1\}$ are not consistent). For each photo, we divide the total weight of consistent triangles by the total weight of all triangles (the "weight" of a triangle is the sum of the weights of its edges). Averaging across all photos, we find a mean weighted triangle consistency of 92.8%.

User-reported confidence. To assess the accuracy of user-reported confidence, we correlated our judgement weights w_i with user-reported confidence by computing the mean weight w_i for all answers at each level of confidence. We found that inter-user agreement and user-reported confidence were indeed correlated: "Guessing", "Probably", and "Definitely" responses had a mean weight (± standard deviation) of 0.54 ± 0.41, 0.63 ± 0.39, and 0.74 ± 0.34, respectively. However, we found that in general, most users did not reliably report their confidence, and thus, despite the positive correlation, we chose not to use the user-reported confidence for any further analysis. In future runs of this task we could eliminate the confidence question to decrease both annotation time and cost.

Validation: varying lighting. To further validate our user judgements, we collected 11 photographs across 4 scenes with identical camera viewpoint but varying lighting conditions from [20], and then measured the extent to which user judgements changed as a result of the lighting change. The scenes are included

on our website and in the supplemental material[4]. On average, we found that for sparsely sampled points, 10.3% of the judgements changed state, and for densely sampled points, 8.7% changed. Judgements that change state are incorrect in at least one of the photos, so we would like our confidence score to be lower for these judgements. Indeed, we find that the mean confidence for consistent judgements (dense: 0.80, sparse: 0.75) is about twice that of judgements that change state (dense: 0.38, sparse: 0.48). This indicates that CUBAM is correctly assigning a lower weight to unreliable judgements.

4.4 Intrinsic Images Algorithm

Our overarching goal is to develop algorithms that can perform accurate intrinsic image decompositions for real-world photographs of whole scenes "in the wild." For images of scenes, our hypothesis is that it is important to model long-range interactions in which objects tend to share a small number of reflectance values. With this in mind, we designed a new algorithm that has a discrete working set of hypothesis reflectances, and considers all $O(n^2)$ pairs of pixels simultaneously when computing reflectances. Further, because we have collected a large dataset of image judgements, we can explore new algorithms whose parameters can be automatically learned using training data, rather than by hand.

Problem formulation. To recap, an intrinsic image algorithm takes as input a photograph (in our case, an Internet photo of an indoor scene), and seeks to decompose the image into a product of reflectance (albedo) and shading (irradiance) at each point. This is a very under-constrained problem, as there are

[4] http://www.cs.cornell.edu/~sbell/pdf/siggraph2014-intrinsic.pdf

infinitely many possible reflectance and shading layers that multiply to explain an input image; hence we want to find the decomposition that *most likely* explains the image, under some priors on what makes a likely decomposition. In other words, given RGB image $\mathbf{I}$, we want to find the RGB reflectance layer $\mathbf{R}^*$ and shading layer $\mathbf{S}^*$ that is most likely under probability distribution p:

$$\mathbf{R}^*, \mathbf{S}^* = \arg\max_{\mathbf{R},\mathbf{S}} p(\mathbf{R}, \mathbf{S} \mid \mathbf{I}) \tag{4.4}$$
$$\text{such that } I_i^c = R_i^c \cdot S_i^c$$

where I_i^c is color channel $c \in \{r, g, b\}$ for image pixel i (and similarly for $\mathbf{R}$ and $\mathbf{S}$).

Formulated this way, the key questions are: (1) how to define the probability distribution $p(\mathbf{R}, \mathbf{S}|\mathbf{I})$ and (2) how to efficiently find the best $\mathbf{R}$ and $\mathbf{S}$ under this distribution. While a full answer to (1) would involve understanding the statistics of natural scenes and illuminations, often these statistics are approximated with a set of priors on $\mathbf{R}$ and $\mathbf{S}$. Our algorithm builds on important priors that have appeared in the literature; our key insight is to apply them in a more global sense, reasoning about all $O(n^2)$ pairs of pixels in an image, whereas most previous methods only consider pairs of neighboring pixels. This global reasoning is a powerful way to encode the observation, true of many real world indoor scenes, that pixels far apart in the image can still often have the same reflectance—for instance, all of the walls in a scene often have the same paint color. In particular, we assign a high probability to decompositions that are consistent with the following priors, each of which have been suggested in prior work:

- Pixels that are nearby, and that have similar chromaticity or intensity, also have similar reflectance.
- Reflectances are piecewise-constant [104, 110, 8].

- Reflectances are sampled from a sparse set [128, 58, 164].
- Certain shading values are *a priori* more likely than others [8].
- Neighboring pixels have similar shading [57].
- Shading is grayscale, or the same color as the light source.

These priors are not new, and different methods of global reasoning have been proposed, such as connecting distant image regions with similar texture [199] or optimizing for sparsity in the reflectance layer [164, 8]. Our method constructs the reflectance layer by drawing from a sparse set of reflectances, a technique inspired by [58].

Our key contribution is that we show how to incorporate all these priors in a global sense, simultaneously reasoning about all $O(n^2)$ pairs of pixels. To do so, we make use of recent work on efficient inference for dense conditional random fields (CRFs) by Krähenbühl and Koltun [96, 98], but show how to apply their framework to the problem of intrinsic image decomposition.

Algorithm Overview. Our algorithm works as follows. First, we hypothesize a set of reflectances $\mathcal{R}$ that are likely to exist in the image—one can think of this set as a "palette" of reflectances that we can draw on for that image. The set $\mathcal{R}$ is unique for each image and, for a typical run of our algorithm, will contain 20 entries once our algorithm converges. After first choosing an initial set of reflectance colors $\mathcal{R}$ using clustering, we iterate between two stages:

1. We label each pixel with a reflectance chosen from $\mathcal{R}$ such that $p(\mathbf{R}, \mathbf{S} \mid \mathbf{I})$ is maximized.
2. We adjust the reflectances in $\mathcal{R}$ by minimizing discontinuities in the shading layer $\mathbf{S}$.

The first stage improves the reflectance layer, and is optimized using discrete labeling; the second stage improves the shading layer, and is optimized using continuous L^1 minimization. We now describe each stage of the algorithm in detail.

Note on grayscale shading. Since we assume that shading is grayscale, our problem only requires solving for scalar reflectance intensity R and shading intensity S. Given these scalar values, we can expand to a full RGB decomposition by:

$$\mathbf{R}_i = \frac{R_i}{\frac{1}{3}\sum_c I_i^c}\mathbf{I}_i \qquad\qquad \mathbf{S}_i = \frac{\frac{1}{3}\sum_c I_i^c}{R_i}[1,1,1] \tag{4.5}$$

where the chromaticity of $\mathbf{S}$ is assumed to be grayscale and the chromaticity for $\mathbf{R}$ is taken from the input $\mathbf{I}$.

4.4.1 Initialization

We assume in what follows that our input image $\mathbf{I}$ has a linear response (in our work, we map our downloaded images from an assumed sRGB space to linear). To compute an initial set $\mathcal{R}$, our algorithm starts by performing a k-means clustering of pixel colors in the input image (similar to [57]). Rather than work in RGB space, which has correlated channels, we transform the colors to better cluster reflectances. For diffuse surfaces lit with pure white light, image pixels on that surface will have the same chromaticity. To take advantage of this invariant, we transform RGB space to three new axes: (1) pixel intensity, (2) red chromaticity, and (3) green chromaticity:

$$[r,g,b] \mapsto \left[\beta \cdot \frac{r+g+b}{3}, \frac{r}{r+g+b}, \frac{g}{r+g+b}\right] \tag{4.6}$$

Under ideal conditions (white lighting, colored diffuse surfaces, no interreflections), this transform perfectly separates different reflectance colors along the second two axes. While more sophisticated color spaces have been proposed [128], we find that Equation 4.6 is sufficient for initialization. When computing color distances, we scale the intensity axis by β since chromaticity is a better predictor of reflectance than intensity. Training against our dataset, we found that a weight of $\beta = 0.5$ works well.

After performing k-means clustering in this color space, we transform back to RGB and collect the cluster centers as our initial set $\mathcal{R}$. Note that while each reflectance in $\mathcal{R}$ is a RGB color, we only use its intensity for the final output. We find that for our algorithm, keeping $\mathcal{R}$ as RGB colors and then projecting down to scalar intensities produces better results than simply using scalar intensity values. In practice, we found that our algorithm is reasonably insensitive to the number of clusters k, though $k \approx 20$ performs the best. Variations on our method are explored later in Table 4.1(b) and Table 4.2.

As described above, our algorithm then alternates between (1) assigning each pixel with a reflectance selected from $\mathcal{R}$ and (2) optimizing the palette of reflectances $\mathcal{R}$ itself to improve shading intensity S.

4.4.2 Stage 1: Optimize reflectance

In the first stage, we would like to label every pixel in the input image with a reflectance chosen from $\mathcal{R}$. We use x to denote the labeling, where x maps each pixel i to a reflectance chosen from our hypothesis reflectances $\mathcal{R}$, denoted as $\mathcal{R}(x_i)$. Each x_i can be thought of as an integer from 0 to $k - 1$ that acts as an index

into our palette $\mathcal{R}$, so reflectance intensity $R_i = \frac{1}{3}\sum_c \mathcal{R}^c(x_i)$.

The optimal reflectance labeling is obtained by maximizing $p(x \mid \mathbf{I})$, which is a discrete labeling problem. We now describe how we model this probability.

Using fully connected conditional random fields

Recently, Krähenbühl and Koltun proposed an algorithm for approximately minimizing a global objective function with a quadratic number of terms in linear time [96, 98]. While their model was originally proposed to improve object recognition and segmentation, we show that it can be adapted for intrinsic image decomposition. Their model considers objective functions of the form:

$$p(x \mid \mathbf{I}) = \frac{1}{Z(\mathbf{I})} \exp\left\{ -\sum_i \psi_i(x_i) - \sum_{i<j} \psi_{ij}(x_i, x_j) \right\} \tag{4.7}$$

$$\psi_{ij}(x_i, x_j) = \sum_m \mu^{(m)}(x_i, x_j)\, k^{(m)}(\mathbf{f}_i - \mathbf{f}_j) \tag{4.8}$$

where,

$p(x \mid \mathbf{I})$	probability of labels x given image $\mathbf{I}$
$Z(\mathbf{I})$	partition function (normalizes the distribution)
i, j	pixel indices
x_i	discrete label for pixel i
$\mathbf{f}_i$	feature vector for pixel i
$\psi_i(\cdot)$	unary cost function for pixel i
$\psi_{ij}(\cdot,\cdot)$	pairwise cost function for pixels i, j
$\mu^{(m)}(\cdot,\cdot)$	m^{th} (negative-semidefinite) label compatibility function
$k^{(m)}(\cdot)$	m^{th} (positive-definite) kernel function

The objective is maximized when x is chosen to minimize the costs incurred by $\psi_i(x_i)$ and $\psi_{ij}(x_i, x_j)$. An important feature of this objective function is that there are $O(n^2)$ pairwise terms ψ_{ij}. When maximizing $p(x|\mathbf{I})$, we can omit the partition function $Z(\mathbf{I})$ and minimize the negative logarithm to arrive at an energy function:

$$\begin{aligned} E(x) &= -\log p(x|\mathbf{I}) + \text{const} \\ &= \sum_i \psi_i(x_i) + \sum_{i<j} \psi_{ij}(x_i, x_j) \end{aligned} \tag{4.9}$$

The key insight of their algorithm is that when using a mean field approximation to the CRF distribution, message passing (which is $O(n^2)$) can be approximated as high-dimensional filtering if certain pairwise functions are used. They use the permutohedral lattice of Adams et al. [1], to perform filtering in linear time, thus obtaining an $O(nd)$ algorithm that approximately maximizes $p(x|\mathbf{I})$, despite having $O(n^2)$ terms, where d is the dimensionality of features $\mathbf{f}$. While their prior work does not quantify the error introduced by their approximation, the model performs well in practice and converges quickly. For example, with 640×480 images and 5-dimensional features, optimization takes about 1 second with one CPU thread.

Probability model

Recall that in our model, the layer of labels x maps each pixel to a reflectance chosen from our hypothesis reflectances $\mathcal{R}$. We now explain how we design functions $\psi_i, \psi_{ij}, \mu, k$ and features $\mathbf{f}$ such that the optimal labeling x is a good estimate of reflectance according to our priors.

Our energy function consists of two types of costs: (1) unary costs ψ_i for each

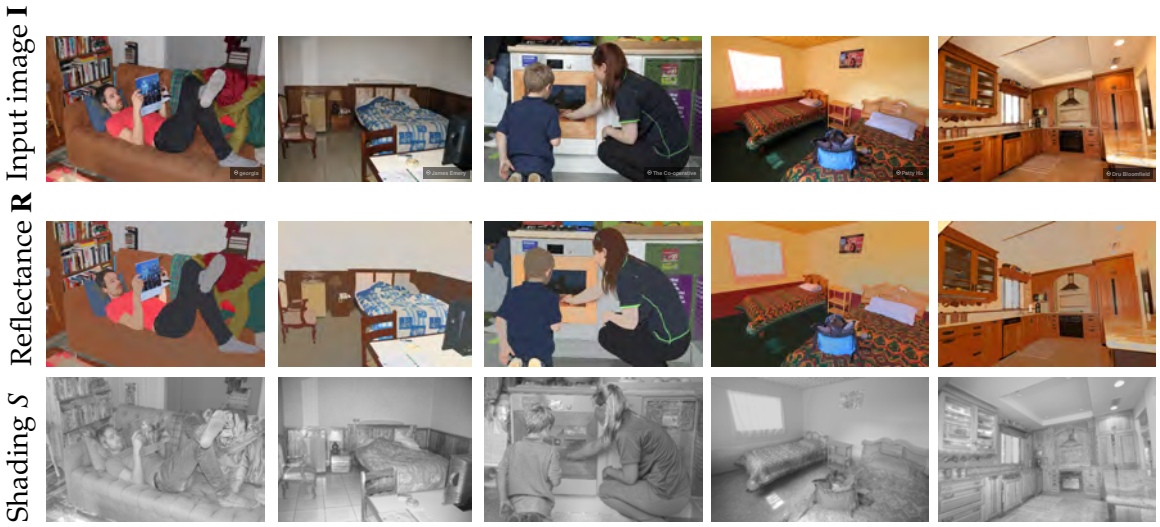

(a) Living room (b) Bedroom 1 (c) Kitchen 1 (d) Bedroom 2 (e) Kitchen 2

Figure 4.6: Example decompositions using our algorithm for a variety of scenes. All outputs are rescaled and mapped to sRGB for display.

pixel, where we want shading to be smooth and avoid extreme values, and (2) pairwise costs ψ_{ij} where we want reflectance to be piecewise constant for all pairs of similar pixels. These costs are represented in an energy function $E(x)$ defined as a weighted sum of three costs:

$$E(x) = \underbrace{w_p E_p(x)}_{\text{pairwise } \psi_{ij}} + \underbrace{w_s E_s(x) + w_l E_l(x)}_{\text{unary } \psi_i} \tag{4.10}$$

where $E_p(x)$ is a pairwise reflectance term, $E_s(x)$ is a pairwise shading term encoded as a unary term, and $E_l(x)$ penalizes extreme values of shading. We now describe each term in more detail.

Pairwise reflectance E_p. The most important term in our model is our pairwise reflectance term E_p, which encourages pixels that are nearby in position, chromaticity, and intensity, to be assigned the same surface reflectance. We map each pixel to a 5-dimensional feature space $\mathbf{f}$ that includes position, intensity, and chromaticity, such that we expect Euclidean distance in this space to predict reflectance distance. For every pair of pixels in the image, if the two pixels are

assigned a different reflectance, we pay a cost proportional to the L^1 difference in this reflectance, Gaussian-weighted according to the distance between the pixels in our feature space.

Mathematically, we define E_p as:

$$E_p(x) = \sum_{i<j} \mu(x_i, x_j) \exp\left(-\frac{1}{2}\|\mathbf{f}_i - \mathbf{f}_j\|_2^2\right) \tag{4.11}$$

$$\mu(x_i, x_j) = \left\|\log \mathcal{R}(x_i) - \log \mathcal{R}(x_j)\right\|_1$$

where $\mu(\cdot, \cdot)$ is the label compatibility function and $\mathbf{f}_i$ is the feature vector for pixel i:

$$\mathbf{f}_i = \left[\frac{p_i^x}{\theta_p\, d}, \frac{p_i^y}{\theta_p\, d}, \frac{\frac{1}{3}\sum_c I_i^c}{\theta_l}, \frac{I_i^r}{\theta_c \sum_c I_i^c}, \frac{I_i^g}{\theta_c \sum_c I_i^c}\right] \tag{4.12}$$

Our feature vector describes each pixel i in terms of its position (p_i^x, p_i^y) normalized by the image diameter d, its intensity, and its red/green chromaticity. Each feature is weighted by model parameters θ_p, θ_l, and θ_c. Under white illumination, two pixels with the same reflectance will have the same chromaticity, so instead of using RGB values for color features, we separate intensity from chromaticity and weight them differently. The particular design of this term (e.g., L^1 distances and Gaussian weights) is chosen in part so that our dense CRF (Equation 4.7) can be efficiently optimized.

As examples of how this term works, consider pixels that are nearby, have similar chromaticity, and have similar intensity. For these pixels, the Gaussian kernel $\exp\left(-\frac{1}{2}\|\mathbf{f}_i - \mathbf{f}_j\|_2^2\right)$ will be large, thus constraining these pixels to receive similar reflectances. In contrast, for pixels that are nearby but have a very different chromaticity and/or reflectance, our pairwise term E_p will be small, allowing the shading smoothness term E_s (described below) to constrain the relative reflectance between nearby regions.

Shading smoothness E_s. Another important feature of good decompositions is that the shading channel tends to vary smoothly across smooth surfaces. Such a smoothness prior on shading helps to determine the relative reflectance across a smooth, textured object—we want the texture of such an object to be correctly attributed to the reflectance layer, with a smooth shading layer.

Hence, we would ideally include in our optimization a pairwise term that depends on shading, such as the following:

$$E_s^{\text{desired}}(x) = \sum_{i<j} \mu_s(x_i, x_j) \exp\left(-\frac{1}{2}\left\|\frac{\mathbf{p}_i - \mathbf{p}_j}{\sigma_s}\right\|_2^2\right)$$
$$\mu_s(x_i, x_j) = \left(\log S_i - \log S_j\right)^2 \tag{4.13}$$

where σ_s is a Gaussian kernel parameter, $\mathbf{p}_i = \left(p_i^x, p_i^y\right)$ is the position of pixel i, and S is shading intensity, $S_i = \sum_c I_i^c / \sum_c \mathcal{R}^c(x_i)$. However, including this term would require a label compatibility function μ_s that depends on image features (since S_i depends on $\mathbf{I}_i$), which does not fit within the constraints of Equation 4.8. Instead, we can approximate S_j by solving the model iteratively, using the shading channel from the previous iteration as our value for S_j. This term now has the functional form of a unary term:

$$E_s(x^{(t)}) = \sum_i \left(\log S_i^{(t)} - \log \tilde{S}_i^{(t-1)}\right)^2 \tag{4.14}$$

$$\tilde{S}_i^{(t-1)} = \frac{1}{A_i} \sum_j S_j^{(t-1)} \exp\left(-\frac{1}{2}\left\|\frac{\mathbf{p}_i - \mathbf{p}_j}{\sigma_s^{(t)}}\right\|_2^2\right) \tag{4.15}$$

where A_i is a normalizing term chosen so that the Gaussian weights sum to 1. Note that $\tilde{S}^{(t-1)}$ is a Gaussian blur of $S^{(t-1)}$ and is fast to compute. Each iteration, we gradually decrease the blur size $\sigma_s^{(t)}$:

$$\sigma_s^{(t)} = \frac{\hat{\sigma}_s d}{t} \tag{4.16}$$

where $\hat{\sigma}_s$ is the normalized initial blur radius, d is the image diameter, and t is the iteration number. In the first iteration ($t = 1$), we find that omitting this term (E_s) works better than initializing shading intensity $S^{(0)}$ with the image intensity or with a constant. Since the blur radius decreases each iteration, this term effectively results in a coarse-to-fine method of smoothing the shading channel.

Absolute shading intensity E_l. In addition to encouraging smoothness of shading, we want to ensure that the optimizer does not choose extreme values of shading for too many pixels, so we add a penalty that pulls shading intensity S towards a constant:

$$E_l(x) = \sum_i |S_i - \bar{S}| \tag{4.17}$$

Training against our dataset, we find that $\bar{S} = 0.5$ works well.

Optimizing the model. Using the method of Krähenbühl and Koltun [98], we can find the discrete labeling x that approximately minimizes Equation 4.10 in just a few seconds. If any labels are not used in the solution, they are dropped from $\mathcal{R}$.

4.4.3 Stage 2: Optimize for shading

In Stage 1, we obtained a hypothesis decomposition (R, S), as well as an indication of which pairs of points have the same reflectance (i and j have the same reflectance iff $x_i = x_j$). In Stage 2, we hold the label assignments x fixed and continuously optimize the palette of reflectances $\mathcal{R}$ in order to improve shading intensity S.

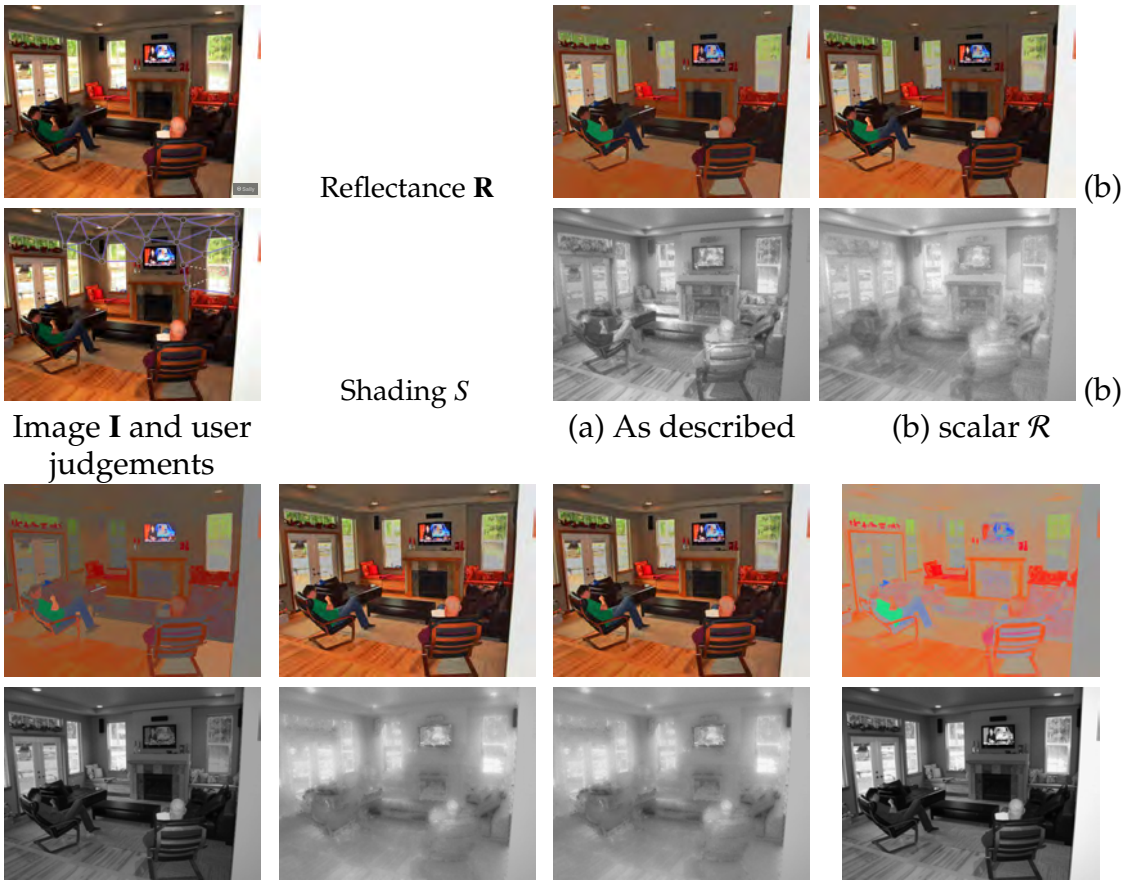

Image **I** and user judgements | (a) As described | (b) scalar $\mathcal{R}$

(c) $w_s = 0$ (No S smoothness) | (d) $\theta_p = 0.001$ (Local-only pairwise) | (e) $w_p = 0$ (No pairwise) | (f) $w_l = 0$ (No S regularization)

Table 4.1: *Algorithm variants.* To illustrate the effect of each term, we take the parameter settings found from training and remove different terms. The WHDR errors for each variant increase from left to right, and are listed in Table 4.2. Top left: input and judgements. Other 6: columns: reflectance (top) and shading (bottom) for each variant.

Following Garces et al. [57], we improve our guess of reflectances by minimizing shading discontinuities between adjacent regions across the image. Since adjacent pixels are likely to be nearby in 3D, they are likely to receive the same illumination. However, inside an image region that is assigned a single reflectance label, shading is already constrained (since setting a value for either R or S fixes the other layer). Thus, if we hold the labels x fixed, we can only minimize shading discontinuities across reflectance boundaries, where $x_i \neq x_j$.

We can update the set of reflectances by multiplying $\mathcal{R}$ by a vector of scalars r, which allows us to regularize the relative change r:

$$\mathcal{R}^{(t)}(i) = r^{(t)}(i) \cdot \mathcal{R}^{(t-1)}(i) \tag{4.18}$$

We solve for r by minimizing shading discontinuities:

$$r^{(t)} = \arg\min_{r} \sum_{(i,j)\in B} |\log S_i - \log S_j| \tag{4.19}$$
$$\log S_i = \log\left(\sum_c I_i^c\right) - \log\left(\sum_c \mathcal{R}^{(t-1),c}(x_i)\right) - \log r(x_i)$$

where S_i is the shading intensity, and B is the set of adjacent pixels (i, j) with different reflectance labels $x_i \neq x_j$. By working in log space, we avoid potential problems with numerical instability and divide-by-zero. We efficiently optimize Equation 4.19 with iteratively reweighted least squares (IRLS), adding a small damping term $10^{-8}\|\log r\|^2$ to each iteration of IRLS since Equation 4.19 is only well-defined up to a constant. Note that we are solving for $|r| = k \approx 20$ variables, not an entire shading layer, and thus this step converges in a few seconds.

Final iteration. As a final optional step, we can split apart connected components in the discrete reflectance map, prior to the last L^1 minimization (Equation 4.19). While this step is not crucial, we find that it provides a small improvement for most scenes. Specifically, we take each connected region in the reflectance image and assign it to a new unique label. As a result, our number of labels in $\mathcal{R}$ jumps from around 20 to around 3000. We find that small connected components in the reflectance channel are typically part of detailed textures. In these cases, smoothing the shading channel performs better than attempting to reason in reflectance space.

Number of iterations. We always run the algorithm for a fixed number of iterations since our shading smoothness term E_s changes every iteration (the blur radius decreases). We find that while the algorithm produces a reasonable result in just a few iterations, the decomposition continues to improve, and that about 25 iterations is sufficient. As listed in Table 4.2, we obtain mean error ($\text{WHDR}_{10\%}$) of 23.5%, 21.5%, and 21.0% after 1, 10, and 25 iterations respectively.

4.5 Results

In this section we use our dataset to evaluate our algorithm and a range of public algorithms for intrinsic image decomposition. We evaluated our algorithm on all images in our dataset. Some example decompositions are shown in Figure 4.6. Generally we find that our algorithm performs very well for real-world scenes. While it is particularly good at finding a single reflectance to explain large continuous regions, it can also handle intricate textures such as wallpapers and bricks. Even when there are many surfaces that do not fit the diffuse reflectance model (such as glossy metals or tinted windows), the model often returns a reasonable result.

4.5.1 Training

Using our large dataset, we explored the effects of changing both the parameters and the structure of our algorithm. We can delete different terms from our energy function $E(x)$ (Equation 4.10) or we can try adding new terms such as priors on absolute reflectances. Table 4.1 shows the effect of deleting different terms and

Algorithm variant	WHDR
(a) As described	21.0%
Add reflectance prior $E_r(x) = -\sum_i \log p(\mathcal{R}(x_i))$	21.0%
Add chromaticity prior $E_c(x) = \sum_i \left\| \frac{\mathcal{R}(x_i)}{\sum_c \mathcal{R}^c(x_i)} - \frac{\mathbf{I}_i}{\sum_c I_i^c} \right\|_1$	21.1%
Use more clusters ($k = 30$)	21.2%
Initialize shading $S_i^{(0)} = \bar{S}$	21.2%
Initialize shading $S_i^{(0)} = \frac{1}{3}\sum_c I_i^c$	21.4%
Eq. 4.19: expand B to include 3-pixel windows	21.4%
Stop after $n_{\text{iter}} = 10$ iterations	21.5%
Don't split connected components in final iteration	21.6%
Eq. 4.19: use L^2 instead of L^1	22.2%
Stop after $n_{\text{iter}} = 1$ iteration	23.5%
Use L^1 in shading smoothness (E_s in Eq. 4.14)	24.6%
(b) Use scalar $\mathcal{R}$ instead of RGB	25.4%
(c) Remove shading smoothness ($w_s = 0$)	26.0%
(d) Limit pairwise to local ($\theta_p = 0.001$)	36.1%
(e) Remove pairwise reflectance ($w_p = 0$)	36.3%
(f) Remove shading regularization ($w_l = 0$)	36.4%

Table 4.2: To justify our design choices, we show that many variants produce higher error. Variants (a) through (f) are shown in Table 4.1. The variants are described in more detail in the supplemental (http://www.cs.cornell.edu/~sbell/pdf/siggraph2014-intrinsic.pdf).

Table 4.2 lists the training error for an even larger set of variants.

In total, we evaluated 295 variants on the full data set and found the following configuration to have the lowest mean error ($\text{WHDR}_{10\%}$): $w_l = 500$, $w_p = 10000$, $w_s = 20000$, $\theta_c = 0.025$, $\theta_l = 0.1$, $\theta_p = 0.1$, $\hat{\sigma}_s = 0.1$, $\beta = 0.5$, $\bar{S} = 0.5$, $k = 20$, $n_{\text{iter}} = 25$.

4.5.2 Ranking

We evaluated a set of existing open-source algorithms over our entire dataset. To compare these algorithms, we evaluate all of them using two scores. First, we compute their weighted human disagreement rate (WHDR) for each photo

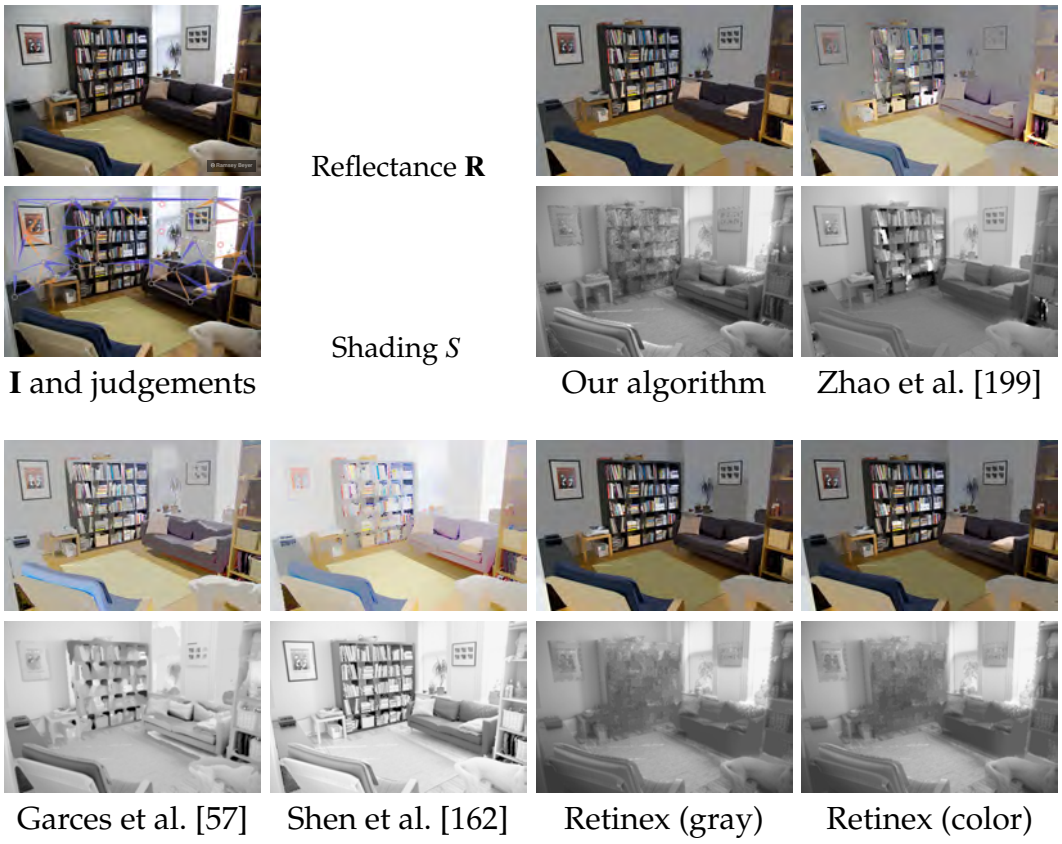

Table 4.3: Visual comparison of our algorithm against several recent open-source algorithms. Each algorithm uses the best parameters found from training (i.e., minimizes mean $\text{WHDR}_{10\%}$ across all photos). Top left: input and judgements. Other 6: columns: reflectance (top) and shading (bottom) for each algorithm.

and average the scores across all photographs. Second, for each photograph, we rank each algorithm by its WHDR score. If two algorithms tie (which is possible since WHDR is discrete), we average together the ranks of those algorithms. For example, if 4 algorithms get scores $[20\%, 11\%, 20\%, 2\%]$, the corresponding ranks would be $[3.5, 2, 3.5, 1]$. We then compute the *mean rank* of each algorithm as its average rank across all photos. When computing WHDR_δ we use $\delta = 10\%$, though we find similar results with 5% and 15%.

Figure 4.7 illustrates our evaluation of several algorithms according to both WHDR and mean rank, including: [199], [57], Retinex [69], [162], and two base-

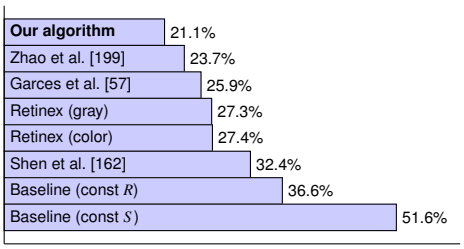

(a) Mean $\text{WHDR}_{10\%}$ over all edges.

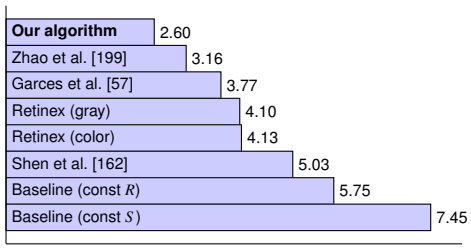

(b) Mean rank of $\text{WHDR}_{10\%}$ over all edges.

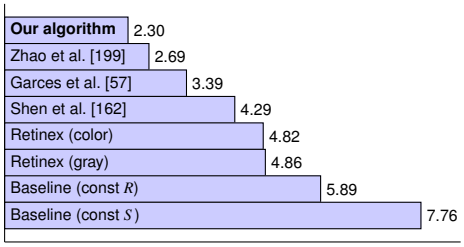

(c) Mean rank of $\text{WHDR}_{10\%}$ over dense edges only.

Figure 4.7: Quantitative comparison of our algorithm against several recent open-source algorithms, using mean weighted human disagreement rate ($\text{WHDR}_{10\%}$). For (c), only the 397 densely sampled photos are considered (about 900 judgements per photo with a minimum separation of 3% of the image diameter). All values are computed using leave-one-out cross validation. See Section 4.5.2 for details.

lines. The baseline decompositions are "const R" ($R_i = 1$) and "const S" ($S_i = 1$), and are converted from intensity to RGB using Equation 4.5. We attempted to include [58] but found that it was too slow to include in our 5,000+ photo evaluation.

Fair evaluation. Since none of these algorithms were given the opportunity to train for our dataset, we tried to make the evaluation fair by trying a range of parameters for each algorithm. We varied both thresholds for Retinex; k for [57]; w_d for [162]; and chromaticity threshold t, texture patch distance, and texture patch variance for [199]. In addition, we tried two variants of [162] and [199]: one as published, and a second where we take sRGB into account when loading the image. In total, we computed over 2,500,000 decompositions for our 5,000+ photo data set. To measure a final test error for each photo, we use leave-one-out

cross-validation (i.e., test each photo using the best parameters for all other photos).

Our algorithm. Out of all the methods we evaluated, our algorithm both has the lowest mean error and the best average rank, averaged across all photos. This is consistent with our visual judgement of the results.

Zhao et al. [199]. We find that for real-world images, [199] performs quite well. The method has the strength of Retinex in that it is accurate at decomposing texture on smooth surfaces, while also having sparse global constraints to connect distant parts of the image together.

Garces et al. [57]. The next best performing algorithm is [57], which is designed for real-world scenes. Most errors in output from [57] appear to come from incorrect clustering of surface reflectances. Highly textured regions are often merged together into a single component, causing the texture to incorrectly appear in the shading layer.

Retinex [69]. The Retinex algorithm [69] is the simplest algorithm, and performs surprisingly well for its algorithmic complexity. We found that the optimal threshold for whole scenes (color threshold 0.7, gray threshold 0.5) is very different than the optimal threshold for the MIT Intrinsic Images dataset (color threshold 0.075, gray threshold 1.0). We were also surprised to find that grayscale intensity was a better predictor of reflectance than color, for scenes "in the wild". Consistent with [69], we note that the L^2 variant of Retinex performs significantly worse than L^1 (41.8% versus 27.4%).

Shen et al. [162]. Finally, we found [162] to perform only slightly better than the baseline in terms of mean error. This seems to correspond to our visual judgement of the output, in which high-frequency texture details are often put in the shading channel, and shading details are not removed from the reflectance layer.

Visual comparison. To understand the typical kinds of visual artifacts made by each algorithm, we include an example decomposition in Table 4.3. Since there is significant variety across photos, and the relative ranking between algorithms changes for each photo, this single example is not sufficient to rank algorithms. More visual comparisons are included in the supplemental material.[5]

Dense vs sparse edges. We have two edge lengths: "sparse", with a point spacing of 7% of the image diameter, and "dense", with a point spacing of 3% of the image diameter. We can repeat the evaluation with only dense edges, as shown in Figure 4.7(c). We find that [162] performs better in a close-range evaluation, which is to be expected since the method optimizes over local windows. To make sure that it is not the distribution over edge types that is affecting the results, we compared the distribution of edges and found that it was about the same for both groups: for sparse edges, 62.8% are equal ("about the same") and 63.9% of the dense edges are equal.

Median individual human. Finally, we can place humans on the scale in the same units, by excluding some user responses from the aggregation and then testing them against the user majority, using our WHDR metric. We exclude 100 random users from the aggregation, and test the excluded users against the

[5] http://www.cs.cornell.edu/~sbell/pdf/siggraph2014-intrinsic.pdf

responses aggregated from the remaining users. Blocked users are excluded from both sets. Since we are evaluating algorithms against humans, who are inconsistent, this is effectively the lowest error we can expect an algorithm to obtain. Averaged across all photos in our dataset, we find that humans have a median WHDR = 7.5%.

4.5.3 MIT Intrinsic Images dataset

We have validated our algorithm against the MIT Intrinsic Images dataset [69], and found that it performs reasonably. We obtained a mean training and test error of $\text{LMSE}_{20} = 0.027$ and $\text{LMSE}_{20} = 0.031$ respectively (which matches color Retinex $\text{LMSE}_{20} = 0.031$). This is certainly not the lowest error reported for this dataset. For example, [8] explicitly models shape and illumination and achieves a lower error, but is limited to individual objects. Our method focuses on real-world scenes, which have very different statistics from small, cleanly segmented purely diffuse objects.

4.6 Limitations and future work

Weaknesses of WHDR. When visually evaluating decompositions, there are many different mistakes that algorithms make: texture variations in **S**, shadows/highlights in **R**, etc. No algorithm avoids all mistakes. An important motivation was therefore to have a large dataset to evaluate algorithms on a wide variety of scenes, each with their own challenges. The question of ranking algorithms becomes: how much should we penalize each mistake? Our "weighted

human disagreement rate" (WHDR) metric is one such answer. We recognize that certain mistakes are not well captured by WHDR, such as a decomposition that does not model colored shading (since our annotations only measure intensity) or that leaves texture in the shading channel (since the sampling is sparse). Conversely, WHDR is sensitive to errors on single-color surfaces (e.g., walls), where humans tend to be confident and consistent. While there is room for proposing other metrics, we found that algorithms that achieved lower WHDR also achieved qualitatively better results.

Reflection models. Our dataset currently filters out mirror and transparent objects, but there is still a wide range of surfaces that do not fit diffuse reflectance models. We chose not to ask users to estimate gloss since many glossy items appear diffuse if they are not oriented to receive a highlight. Nonetheless, we would like to explore this issue in the future and expand our image formation model to include glossy reflection.

Colored lighting and hard shadows. Scenes in the real world have colored illumination (Figure 4.8), especially when considering interreflections between colored surfaces. It is common for scenes to have multiple dominant illuminating colors, such as a blue sky and an incandescent light bulb. Further, hard shadows with colored illumination cause the shadowed region to have a shift in chromaticity. For these scenes, our algorithm may put the shadow discontinuity in the texture channel. While the common assumption that shading is grayscale works reasonably well for many scenes, we would like to consider methods and collect datasets that capture color in the shading channel and do not assume that **S** is grayscale.

Figure 4.8: Challenging scenes that violate our assumptions. Using the parameters from Sec. 4.5.1, we obtain WHDR = 67%, 45%, 43%.

Synthetic images. We would like to further evaluate the quality of human judgements by using ground truth synthetic rendered images. However, the main challenge with synthetic images is that it is extremely difficult to replicate the true diversity and variety found in Internet photo collections. Further, many 3D scenes available online do not accurately model reality and include features such as meso-scale geometry in albedo maps.

Photograph variety. While our dataset does a reasonable job of covering typical indoor photographs, there are only a few outdoor and nature scenes (e.g., in the "staircase" category), and thus it does not fully represent the statistics of all images available online. Future work could include determining whether the same priors (piece-wise constant reflectances, sparse set of intensities, etc.) are useful in decomposing outdoor photographs.

4.7 Conclusion

In this chapter we introduced a large scale dataset (5000+ images) for *Intrinsic Images in the Wild*, with crowdsourced pairwise annotations of reflectance intensity comparisons. We also introduced a dense-CRF-based intrinsic image

decomposition algorithm that considers long-range interactions to achieve better decomposition on our new database, while maintaining local detail. While we have taken steps towards intrinsic images for real-world scenes and uncalibrated photos, many challenges and avenues of future work remain on this problem. Just as the availability of the MIT Intrinsic Images dataset was important to galvanizing research on intrinsic image algorithms, we hope our public database and code will help drive improvements in intrinsic image decomposition in the wild.

4.8 Impact

Our work was published at SIGGRAPH 2014 [11]. Our IIW judgement dataset has been used to train and validate new models that use deep learning to predict reflectance and lightness variations in an image [203, 206, 123]. Using our data, others have proposed extensions of our algorithm that use deeply learned priors [203], or entirely new algorithms using global least squares optimizations [206], L1 image transforms [17], or near-L0 image transforms [44]. Our pairwise reflectance judgements have inspired others to extend our relative reflectance judgements to relative depth judgements [206] which can be globalized to solve for a full depth map.

CHAPTER 5

INSIDE-OUTSIDE NET: DETECTING OBJECTS IN CONTEXT WITH SKIP POOLING AND RECURRENT NEURAL NETWORKS

5.1 Introduction

Scene understanding requires a complete description of many different aspects of a scene, including objects, materials, depth, surfaces, and lighting. In previous chapters, we focused on materials, surfaces, and lighting. In this chapter, we address a different but important piece of the scene understanding problem—which objects are present in an image and where are they? In order to have a fully general method of understanding images in the world, automatic detection and localization of objects is a critical piece. To address this problem, we develop a new deep-learning-based object detection architecture with several new components.

Reliably detecting an object requires a variety of information, including the object's fine-grained details and the context surrounding it. Current state-of-the-art detection approaches [60, 146] only use information near an object's region of interest (ROI). This places constraints on the type and accuracy of objects that may be detected.

We explore expanding the approach of [65] to include two additional sources of information. The first uses a multi-scale representation [92] that captures fine-grained details by pooling from multiple lower-level convolutional layers in a ConvNet [166]. These skip-layers [158, 116, 119, 73] span multiple spatial resolutions and levels of feature abstraction. The information gained is especially

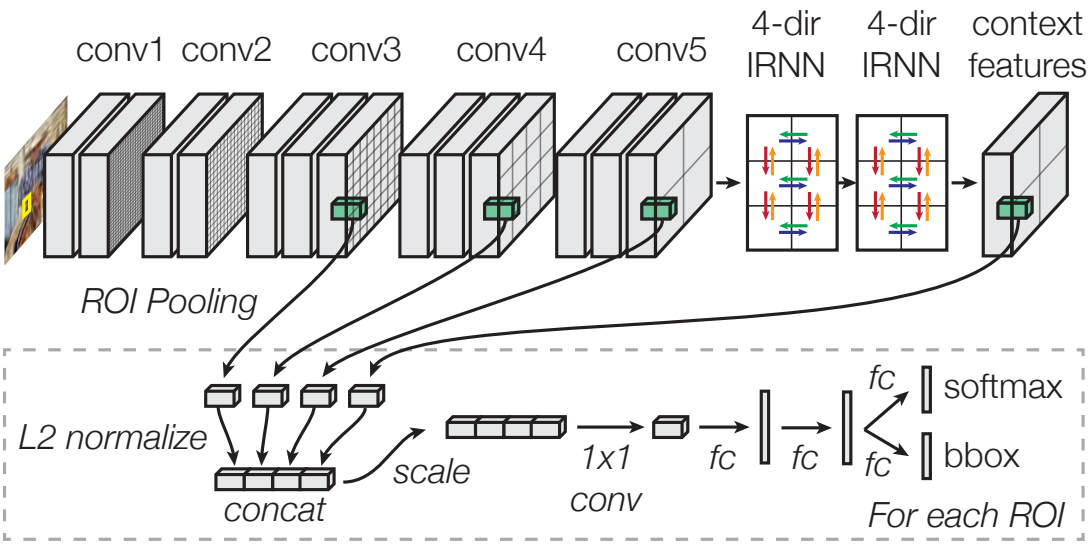

Figure 5.1: **Inside-Outside Net (ION).** In a single pass, we extract VGG16 [166] features and evaluate 2000 proposed regions of interest (ROI). For each proposal, we extract a fixed-size descriptor from several layers using ROI pooling [65]. Each descriptor is L2-normalized, concatenated, scaled, and dimension-reduced (1x1 convolution) to produce a fixed-length feature descriptor for each proposal of size 512x7x7. Two fully-connected (fc) layers process each descriptor and produce two outputs: a one-of-K class prediction ("softmax"), and an adjustment to the bounding box ("bbox").

important for small objects, which require the higher spatial resolution provided by lower-level layers.

Our second addition is the use of contextual information. It is well known in the study of human and computer vision that context plays an important role in visual recognition [175, 133, 45]. To gather contextual information we explore the use of spatial Recurrent Neural Networks (RNNs). These RNNs pass spatially varying contextual information both horizontally and vertically across an image. The use of at least two RNN layers ensures information may be propagated across the entire image. We compare our approach to other common methods for adding contextual information, including global average pooling and additional convolutional layers. Global average pooling provides information about the entire image, similar to the features used for scene or

image classification [127, 99].

Following previous approaches [66], we use object proposal detectors [80, 177, 205] to identify ROIs in an image. Each ROI is then classified as containing one or none of the objects of interest. Using dynamic pooling [77] we can efficiently evaluate thousands of different candidate ROIs with a single forwards pass of the network. For each candidate ROI, the multi-scale and context information is concatenated into a single layer and fed through several fully connected layers for classification.

We demonstrate that both sources of additional information, context and multi-scale, are complementary in nature. This matches our intuition that context features look broadly across the image, while multi-scale features capture more fine-grained details. We show large improvements on the PASCAL VOC [48] and Microsoft COCO [112] object detection datasets and provide a thorough evaluation of the gains across different object types. We find that they are most significant for object types that have been historically difficult. For example, we show improved accuracy for potted plants which are often small and amongst clutter. In general, we find that our approach is more adept at detecting small objects than previous state-of-the-art methods. For heavily occluded objects like chairs, gains are found when using contextual information.

While the technical methods employed (spatial RNNs [68, 23, 184], skip-layer connections [158, 116, 119, 73]) have precedents in the literature, we demonstrate that their well-executed combination has an unexpectedly positive impact on the detector's accuracy. As always, the devil is in the details [27] and thus this chapter aims to provide a thorough exploration of design choices and their outcomes.

Contributions. We make the following contributions:

1. We introduce the ION architecture that leverages context and multi-scale skip pooling for object detection.
2. We achieve state-of-the-art results on PASCAL VOC 2007, with a mAP of 80.1%, VOC 2012, with a mAP of 77.9%, and on COCO, with a mAP of 33.1%.
3. We conduct extensive experiments evaluating choices like the number of layers combined, using a segmentation loss, normalizing feature amplitudes, different RNN architectures, and other variations.
4. We analyze ION's performance and find improved accuracy across the board, especially for small objects.

5.2 Prior work

ConvNet object detectors. ConvNets with a small number of hidden layers have been used for object detection for the last two decades (e.g., from [178] to [158]). Until recently, they were successful in restricted domains such as face detection. Recently, deeper ConvNets have led to radical improvements in the detection of more general object categories. This shift came about when the successful application of deep ConvNets to image classification [99] was transferred to object detection in the R-CNN system of Girshick et al. [66] and the OverFeat system of Sermanet et al. [157]. Our work builds on the rapidly evolving R-CNN ("region-based convolutional neural network") line of work. Our experiments are conducted with Fast R-CNN [65], which is an end-to-end trainable refinement of He et al.'s SPPnet [77]. We discuss the relationship of

our approach to other methods later in the paper in the context of our model description and experimental results.

Spatial RNNs. Recurrent Neural Networks (RNNs) exist in various extended forms, including bidirectional RNNs [155] that process sequences left-to-right and right-to-left in parallel. Beyond simple sequences, RNNs exist in full multi-dimensional variants, such as those introduced by Graves and Schmidhuber [68] for handwriting recognition, or as hierarchical recurrent pyramids (the Neural Abstraction Pyramid [10]). As a lower-complexity alternative, [23, 184] explore running an RNN spatially (or laterally) over a feature map in place of convolutions. In this paper, we employ spatial RNNs as a mechanism for computing contextual features for use in object detection.

Skip-layer connections. Skip-layer connections are a classic neural network idea wherein activations from a lower layer are routed directly to a higher layer while bypassing intermediate layers. The specifics of the wiring and combination method differ between models and applications. Our usage of skip connections is most closely related to those used by Sermanet et al. [158] (termed "multi-stage features") for pedestrian detection. Different from [158], we find it essential to L2 normalize activations from different layers prior to combining them.

The need for activation normalization when combining features across layers was recently noted by Liu et al.(ParseNet [116]) in a model for semantic segmentation that makes use of global image context features. Skip connections have also been popular in recent models for semantic segmentation, such as the "fully convolutional networks" in [119], and for object instance segmentation, such as the "hypercolumn features" in [73].

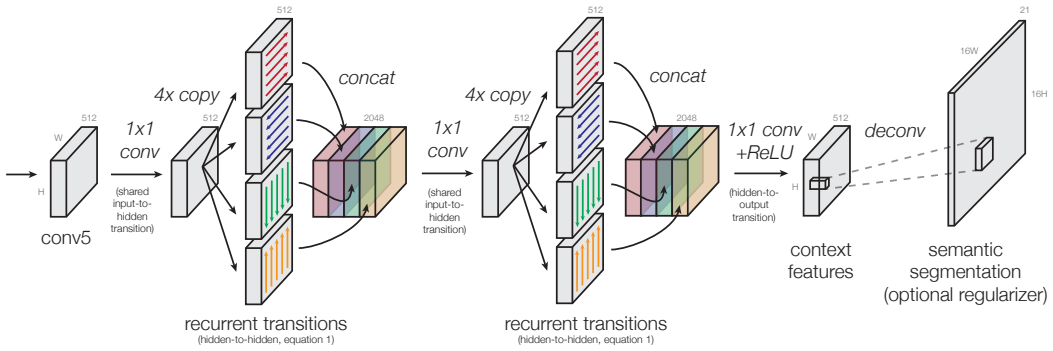

Figure 5.2: **Four-directional IRNN architecture.** We use "IRNN" units [105] which are RNNs with ReLU recurrent transitions, initialized to the identity. All transitions to/from the hidden state are computed with 1x1 convolutions, which allows us to compute the recurrence more efficiently (Eq. 5.1). When computing the context features, the spatial resolution remains the same throughout (same as conv5). The semantic segmentation regularizer has a 16x higher resolution; it is optional and gives a small improvement of around +1 mAP point.

5.3 Architecture: Inside-Outside Net (ION)

In this section we describe ION (Figure 5.1), a detector with an improved descriptor both inside and outside the ROI. We begin with a brief overview of the entire architecture, followed by specific details. To detect objects, a single deep ConvNet processes an image, and the convolutional feature maps from each layer are stored in memory. At the top of the network, a 2x stacked 4-directional IRNN (Figure 5.2, explained later) computes context features that describe the image both globally and locally. The context features have the same dimensions as "conv5." This is done once per image. In addition, we have thousands of proposal regions (ROIs) that might contain objects. For each ROI, we extract a fixed-length feature descriptor from several layers ("conv3", "conv4", "conv5", and "context features"). The descriptors are L2-normalized, concatenated, rescaled, and dimension-reduced (1x1 convolution) to produce a fixed-length feature descriptor for each proposal of size 512x7x7. Two fully-connected (FC) layers process each descriptor and produce two outputs: a one-of-K object class

prediction ("softmax"), and an adjustment to the proposal region's bounding box ("bbox"). The rest of this section explains the details of ION and motivates why we chose this particular architecture.

5.3.1 Pooling from multiple layers

Recent successful detectors such as Fast R-CNN, Faster R-CNN [146], and SPPnet, all pool from the last convolutional layer ("conv5_3") in VGG16 [166]. In order to extend this to multiple layers, we must consider issues of dimensionality and amplitude.

Since we know that pre-training on ImageNet is important to achieve state-of-the-art performance [3], and we would like to use the previously trained VGG16 network [166], it is important to preserve the existing layer shapes. Therefore, if we want to pool out of more layers, the final feature must also be shape 512x7x7 so that it is the correct shape to feed into the first fully-connected layer (fc6). In addition to matching the original shape, we must also match the original activation amplitudes, so that we can feed our feature into fc6.

To match the required 512x7x7 shape, we concatenate each pooled feature along the channel axis and reduce the dimension with a 1x1 convolution. To match the original amplitudes, we L2 normalize each pooled ROI and re-scale back up by an empirically determined scale. Our experiments use a "scale layer" with a learnable per-channel scale initialized to 1000 (measured on the training set). We later show in Section 5.5.2 that a fixed scale works just as well.

As a final note, as more features are concatenated together, we need to corre-

spondingly decrease the initial weight magnitudes of the 1x1 convolution, so we use "Xavier" initialization [172].

5.3.2 Context features with IRNNs

Our architecture for computing context features in ION is shown in more detail in Figure 5.2. On top of the last convolutional layer (conv5), we place RNNs that move *laterally* across the image. Traditionally, an RNN moves left-to-right along a sequence, consuming an input at every step, updating its hidden state, and producing an output. We extend this to two dimensions by placing an RNN along each row and along each column of the image. We have four RNNs in total that move in the cardinal directions: right, left, down, up. The RNNs sit on top of conv5 and produce an output with the same shape as conv5.

There are many possible forms of recurrent neural networks that we could use: gated recurrent units (GRU) [33], long short-term memory (LSTM) [78], and plain tanh recurrent neural networks. In this chapter, we explore RNNs composed of rectified linear units (ReLU). Le et al. [105] recently showed that these networks are easy to train and are good at modeling long-range dependencies, if the recurrent weight matrix is initialized to the identity matrix. This means that at initialization, gradients are propagated backwards with full strength. Le et al. [105] call a ReLU RNN initialized this way an "IRNN," and show that it performs almost as well as an LSTM for a real-world language modeling task, and better than an LSTM for a toy memory problem. We adopt this architecture because it is very simple to implement and parallelize, and is much faster than LSTMs or GRUs to compute.

For our problem, we have four independent IRNNs that move in four directions. To implement the IRNNs as efficiently as possible, we split the internal IRNN computations into separate logical layers. Viewed this way, we can see that the input-to-hidden transition is a 1x1 convolution, and that it can be shared across different directions. Sharing this transition allows us to remove 6 conv layers in total with a negligible effect on accuracy (−0.1 mAP). The bias can be shared in the same way, and merged into the 1x1 conv layer. The IRNN layer now only needs to apply the recurrent matrix and apply the nonlinearity at each step. The output from the IRNN is computed by concatenating the hidden state from the four directions at each spatial location.

This is the update for an IRNN that moves to the right; similar equations exist for the other directions:

$$h_{i,j}^{\text{right}} \leftarrow \max\left(\mathbf{W}_{hh}^{\text{right}} h_{i,j-1}^{\text{right}} + h_{i,j}^{\text{right}}, 0\right). \tag{5.1}$$

Notice that the input is not explicitly shown in the equation, and there is no input-to-hidden transition. This is because it was computed as part of the 1x1 input-to-hidden convolution, and then copied in-place to each hidden layer. For each direction, we can compute all of the independent rows/columns in parallel, stepping all IRNNs together with a single matrix multiply. On a GPU, this results in large speedups compared to computing the RNN cells one by one.

We also explore using semantic segmentation labels to regularize the IRNN output. When using these labels, we add the deconvolution and crop layer as implemented by Long et al. [119]. The deconvolution upsamples by 16x with a 32x32 kernel, and we add an extra softmax loss layer with a weight of 1. This is evaluated in Section 5.5.3.

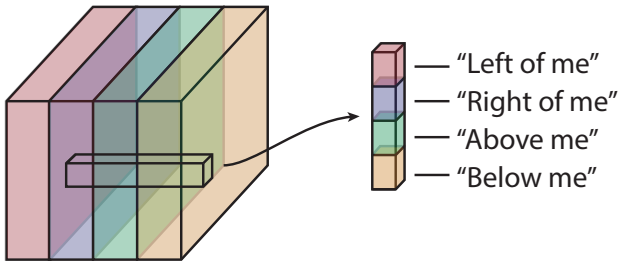

(a) Output of first IRNN ***(b)*** Slice of single cell

Figure 5.3: Interpretation of the first IRNN output. Each cell in the output summarizes the features to the left/right/top/bottom.

Variants and simplifications. We explore several further simplifications.

1. We fixed the hidden transition matrix to the identity $\mathbf{W}_{hh}^{\text{right}} = I$, which allows us to entirely remove it:

$$h_{i,j}^{\text{right}} \leftarrow \max\left(h_{i,j-1}^{\text{right}} + h_{i,j}^{\text{right}}, 0\right). \tag{5.2}$$

   This is like an accumulator, but with ReLU after each step. In Section 5.5.5 we show that removing the recurrent matrix has a surprisingly small impact.
2. To prevent overfitting, we include dropout layers ($p = 0.25$) after each concat layer in all experiments. We later found that in fact the model is underfitting and there is no need for dropout anywhere in the network.
3. Finally, we trained a separate bias b_0 for the first step in the RNN in each direction. However, since it tends to remain near zero after training, this component is not really necessary.

Interpretation. After the first 4-directional IRNN (out of the two IRNNs), we obtain a feature map that summarizes nearby objects at every position in the image. As illustrated in Figure 5.3, we can see that the first IRNN creates a sum-

mary of the features to the left/right/top/bottom of every cell. The subsequent 1x1 convolution then mixes this information together as a dimension reduction.

After the second 4-directional IRNN, every cell on the output depends on every cell of the input. In this way, our context features are both global and local. The features vary by spatial position, and each cell is a global summary of the image with respect to that specific spatial location.

5.4 Results

We train and evaluate our dataset on three major datasets: PASCAL VOC2007 [48], VOC2012, and on MS COCO [112]. We demonstrate state-of-the-art results on all three datasets.

5.4.1 Experimental setup

All of our experiments use Fast R-CNN [65] built on the Caffe [86] framework, and the VGG16 architecture [166], all of which are available online. As is common practice, we use the publicly available weights pre-trained on ILSVRC2012 [151] downloaded from the Caffe Model Zoo.[1]

We make some changes to Fast R-CNN, which give a small improvement over the baseline. We use 4 images per mini-batch, implemented as 4 forward/backward passes of single image mini-batches, with gradient accumulation. We sample 128 ROIs per image leading to 512 ROIs per model update. We

[1] https://github.com/BVLC/caffe/wiki/Model-Zoo

Method	Boxes	R	W	D	Train	Time	mAP	aero	bike	bird	boat	bottle	bus	car	cat	chair	cow	table	dog	horse	mbike	person	plant	sheep	sofa	train	tv
FRCN [65]	SS				07+12	0.3s	70.0	77.0	78.1	69.3	59.4	38.3	81.6	78.6	86.7	42.8	78.8	68.9	84.7	82.0	76.6	69.9	31.8	70.1	74.8	80.4	70.4
Faster [146]	RPN				07+12	0.2s	73.2	76.5	79.0	70.9	65.5	52.1	83.1	84.7	86.4	52.0	81.9	65.7	84.8	84.6	77.5	76.7	38.8	73.6	73.9	83.0	72.6
MR-CNN [60]	SS+EB	✓			07+12	30s	78.2	80.3	84.1	78.5	70.8	**68.5**	**88.0**	85.9	87.8	60.3	85.2	73.7	87.2	86.5	**85.0**	76.4	48.5	76.3	75.5	85.0	81.0
ION [ours]	SS				07+12	0.8s	74.6	78.2	79.1	76.8	61.5	54.7	81.9	84.3	88.3	53.1	78.3	71.6	85.9	84.8	81.6	74.3	45.6	75.3	72.1	82.6	81.4
ION [ours]	SS	✓			07+12	0.8s	75.6	79.2	83.1	77.6	65.6	54.9	85.4	85.1	87.0	54.4	80.6	73.8	85.3	82.2	82.2	74.4	47.1	75.8	72.7	84.2	80.4
ION [ours]	SS	✓	✓	✓	07+12	1.2s	77.6	79.7	83.4	78.1	65.7	62.0	86.5	85.8	88.8	60.2	83.4	75.1	86.5	87.3	82.1	79.7	48.3	77.0	75.3	85.3	82.4
ION [ours]	SS+EB	✓	✓	✓	07+12	2.0s	79.4	82.5	86.2	79.9	71.3	67.2	88.6	87.5	88.7	60.8	84.7	72.3	87.6	**87.7**	83.6	82.1	53.8	**81.9**	74.9	85.8	81.2
ION [ours]	SS	✓			07+12+S	0.8s	76.5	79.2	79.2	77.4	69.8	55.7	85.2	84.2	89.8	57.5	78.5	73.8	87.8	85.9	81.3	75.3	49.7	76.9	74.6	85.2	82.1
ION [ours]	SS	✓	✓		07+12+S	1.2s	78.5	80.2	84.7	78.8	72.4	61.9	86.2	86.7	89.5	59.1	84.1	74.7	88.9	86.9	81.3	80.0	50.9	80.4	74.1	86.6	83.3
ION [ours]	SS	✓	✓	✓	07+12+S	1.2s	79.2	80.2	85.2	78.8	70.9	62.6	86.6	86.9	89.8	61.7	86.9	76.5	88.4	87.5	83.4	80.5	52.4	78.1	**77.2**	**86.9**	**83.5**
ION [ours]	SS+EB	✓	✓	✓	07+12+S	2.0s	**80.1**	**84.2**	**87.2**	**82.1**	**74.8**	67.1	85.0	**88.0**	**89.3**	**60.4**	**86.1**	**76.3**	**88.7**	86.3	83.5	**82.2**	**55.5**	80.5	75.3	86.5	83.3

Table 5.1: **Detection results on VOC 2007 test.** Legend: **07+12:** 07 trainval + 12 trainval, **07+12+S:** 07+12 plus SBD segmentation labels [72], **R:** include 2x stacked 4-dir IRNN (context features), **W:** two rounds of box regression and weighted voting [60], **D:** remove all dropout, **SS:** SelectiveSearch [177], **EB:** EdgeBoxes [205], **RPN:** region proposal net. [146], **Time:** per image, excluding proposal generation.

Method	Boxes	R	W	D	Train	mAP	aero	bike	bird	boat	bottle	bus	car	cat	chair	cow	table	dog	horse	mbike	person	plant	sheep	sofa	train	tv
FRCN [65]	SS				07++12	68.4	82.3	78.4	70.8	52.3	38.7	77.8	71.6	89.3	44.2	73.0	55.0	87.5	80.5	80.8	72.0	35.1	68.3	65.7	80.4	64.2
Faster [146]	RPN				07++12	70.4	84.9	79.8	74.3	53.9	49.8	77.5	75.9	88.5	45.6	77.1	55.3	86.9	81.7	80.9	79.6	40.1	72.6	60.9	81.2	61.5
FRCN+YOLO [143]	SS				07++12	70.4	83.0	78.5	73.7	55.8	43.1	78.3	73.0	89.2	49.1	74.3	56.6	87.2	80.5	80.5	74.7	42.1	70.8	68.3	81.5	67.0
HyperNet [94]	RPN				07++12	71.4	84.2	78.5	73.6	55.6	53.7	78.7	79.8	87.7	49.6	74.9	52.1	86.0	81.7	83.3	81.8	48.6	73.5	59.4	79.9	65.7
MR-CNN [60]	SS+EB		✓		07+12	73.9	85.5	82.9	76.6	57.8	62.7	79.4	77.2	86.6	55.0	79.1	62.2	87.0	83.4	84.7	78.9	45.3	73.4	65.8	80.3	74.0
ION [ours]	SS	✓	✓	✓	07+12	74.7	86.9	84.5	75.2	58.2	57.7	80.5	78.3	90.4	54.4	79.9	60.5	88.4	83.0	83.0	81.2	50.7	77.3	67.6	83.5	72.3
ION [ours]	SS+EB	✓	✓	✓	07+12	76.4	88.0	84.6	77.7	63.7	**63.6**	80.8	80.8	90.9	55.5	81.9	60.9	89.1	84.9	84.2	83.9	53.2	79.8	67.4	84.4	72.9
ION [ours]	SS	✓	✓	✓	07+12+S	76.4	87.5	84.7	76.8	63.8	58.3	**82.6**	79.0	90.9	57.8	82.0	64.7	88.9	86.5	84.7	82.3	51.4	78.2	**69.2**	**85.2**	73.5
ION [ours]	SS+EB	✓	✓	✓	07+12+S	**77.9**	**88.3**	**85.7**	**80.5**	**67.2**	**63.6**	82.5	**82.0**	**91.4**	**58.2**	**84.1**	**65.3**	**90.1**	**87.3**	**85.0**	**84.4**	**53.6**	**80.7**	69.1	84.6	**74.7**

Table 5.2: **Detection results on VOC 2012 test.** Legend: **07+12:** 07 trainval + 12 trainval, **07++12:** 07 trainvaltest + 12 trainval, **07+12+S:** 07+12 plus SBD segmentation labels [72], **R:** include 2x stacked 4-dir IRNN (context features), **W:** two rounds of bounding box regression and weighted voting [60], **D:** remove all dropout, **SS:** SelectiveSearch [177], **EB:** EdgeBoxes [205], **RPN:** region proposal network [146].

Method	Boxes	RW	D	Train	Avg. Precision, IoU: 0.5:0.95	0.50	0.75	Avg. Precision, Area: Small	Med.	Large	Avg. Recall, # Dets: 1	10	100	Avg. Recall, Area: Small	Med.	Large
FRCN [65]*	SS			train	20.5	39.9	19.4	4.1	20.0	35.8	21.3	29.5	30.1	7.3	32.1	52.0
FRCN [65]*	SS	✓		train	20.0	40.3	18.1	4.1	19.6	34.5	20.8	29.1	29.8	7.4	31.9	50.9
ION [ours]	SS	✓		train	23.0	42.0	23.0	6.0	23.8	37.3	23.0	32.4	33.0	9.7	37.0	53.5
ION [ours]	SS	✓	✓	train	23.6	43.2	23.6	6.4	24.1	38.3	23.2	32.7	33.5	10.1	37.7	53.6
ION [ours]	SS	✓	✓	train+S	24.9	44.7	25.3	7.0	26.1	40.1	23.9	33.5	34.1	10.7	38.8	54.1
ION [ours]	SS	✓✓	✓	train+S	24.6	46.3	23.3	7.4	26.2	38.8	23.7	33.9	34.6	11.7	40.0	53.8
ION comp.†	MCG+RPN	✓✓	✓	trainval35k+S	31.2	53.4	32.3	12.8	32.9	45.2	27.8	43.1	45.6	23.6	50.0	63.2
ION post.†	MCG+RPN	✓✓	✓	trainval35k+S	**33.1**	**55.7**	**34.6**	**14.5**	**35.2**	**47.2**	**28.9**	**44.8**	**47.4**	**25.5**	**52.4**	**64.3**

Table 5.3: **Detection results on COCO 2015 test-dev.** Legend: **R:** include 2x stacked 4-dir IRNN (context features), **W:** two rounds of bounding box regression and weighted voting [60], **D:** remove all dropout, **+S:** train with segmentation labels, **SS:** SelectiveSearch [177], **MCG:** MCG proposals [138], **RPN:** region proposal net [146]. †Our submission to the 2015 MS COCO Detection Competition, and post-competition improvements, described in the Supplemental (http://www.cs.cornell.edu/~sbell/). *These scores are higher than [65] due to our improved hyperparameters.

measure the L2 norm of the parameter gradient vector and rescale it if its norm is above 20 (80 when accumulating over 4 images).

To accelerate training, we use a two-stage schedule. As noted by Girshick [65], it is not necessary to fine-tune all layers, and nearly the same performance can be achieved by fine-tuning starting from conv3_1. With this in mind, we first train for 40k iterations with conv1_1 through conv5_3 frozen, and then another 100k iterations with only conv1_1 through conv2_2 frozen. All other layers are fine-tuned. When training for COCO, we use 80k and 320k iterations respectively. We found that shorter training schedules are not enough to fully converge.

We also use a different learning rate (LR) schedule. The LR exponentially decays from $5 \cdot 10^{-3}$ to 10^{-4} in the first stage, and from 10^{-3} to 10^{-5} in the second stage. To reduce the effect of random variation, we fix the random seed so that all variants see the same images in the same order. For PASCAL VOC we use the same pre-computed selective search boxes from Fast R-CNN, and for COCO we use the boxes precomputed by Hosang et al. [80]. Finally, we modified the test thresholds in Fast R-CNN so that we keep only boxes with a softmax score above 0.05, and keep at most 100 boxes per image.

When re-running the baseline Fast R-CNN using the above settings, we see a +0.8 mAP improvement over the original settings on VOC 2007 test. We compare against the baseline using our improved settings where possible.

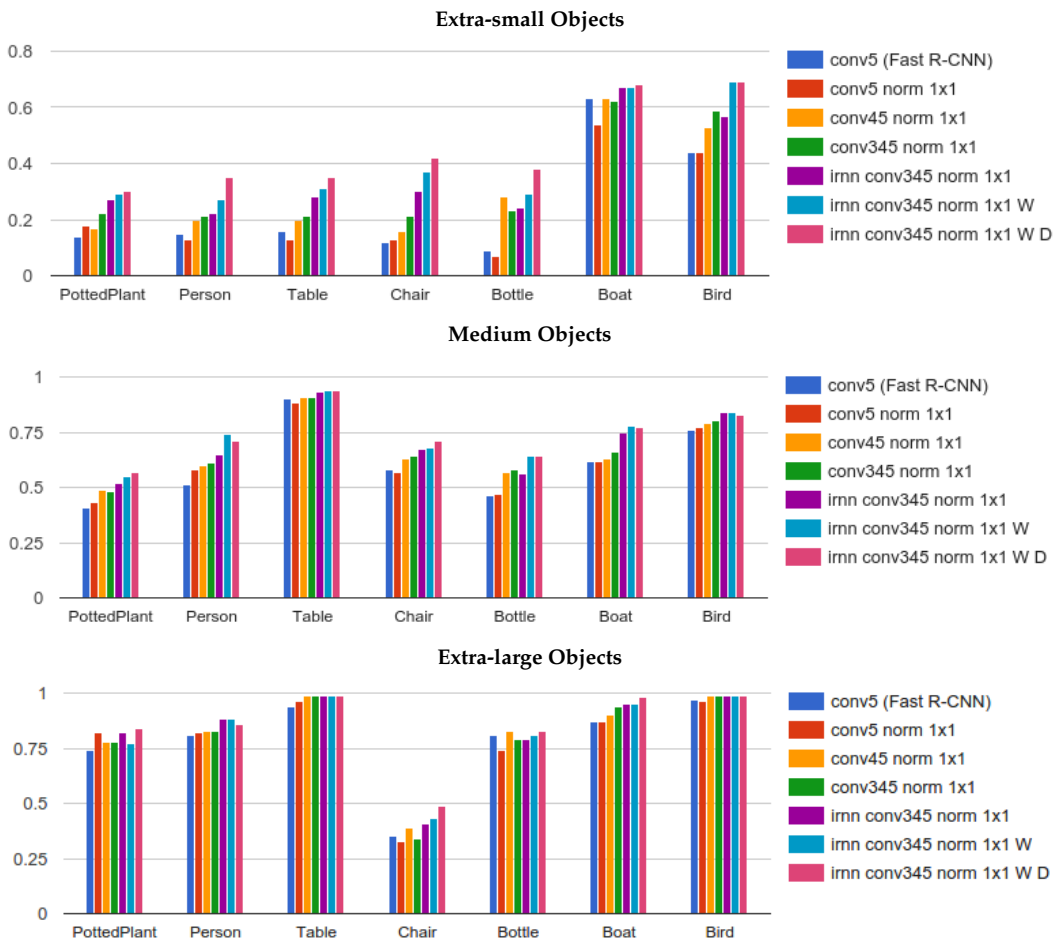

Figure 5.4: **VOC 2007 normalized AP by size.** Left to right: increasing complexity. Left-most bar in each group: Fast R-CNN; right-most bar: our best model that achieves 79.2% mAP on VOC 2007 test. Our detector has a particularly large improvement for small objects. See Hoiem [79] for details on these metrics.

5.4.2 PASCAL VOC 2007

As shown in Table 5.1, we evaluate our detector (ION) on PASCAL VOC 2007, training on the VOC 2007 trainval dataset merged with the 2012 trainval dataset, a common practice. Applying our method described above, we obtain a mAP of 76.5%. We then make some simple modifications, as described below, to achieve a higher score of 79.2%.

MR-CNN [60] introduces a bounding box regression scheme to improve

results on VOC, where bounding boxes are evaluated twice: (1) the initial proposal boxes are evaluated and regressed to improved locations and then (2) the improved locations are passed again through the network. All boxes are accumulated together, and non-max supression is applied. Finally, a weighted vote is computed for each kept box (over all boxes, including those suppressed), where boxes that overlap a kept box by at least 0.5 IoU contribute to the average. For our method, we use the softmax scores as the weights. When adding this scheme to our method, our mAP rises from 76.5% to 78.5%. Finally, we observed that our models are underfitting and we remove dropout from all layers to get a further gain up to 79.2%.

For a direct comparison to MR-CNN, we also trained our method on both SelectiveSearch [177] and EdgeBoxes [205] (SS+EB) but not segmentation labels. With these settings, we achieve 79.4% mAP with a runtime of 2s/image,[2] while MR-CNN achieves 78.2% mAP at 30s/image. See Table 5.1.

5.4.3 PASCAL VOC 2012

We also evaluate on the slightly more challenging VOC 2012 dataset, submitting to the public evaluation server.[3] In Table 5.2, we show the top methods on the public leaderboard as of the time of submission. Our detector obtains a mAP of 76.4%, which is several points higher than the next best submission, and is the most accurate for most categories.

[2]On a single Titan X GPU, excluding proposal generation
[3]Anonymous URL: http://host.robots.ox.ac.uk:8080/anonymous/B3VFLE.html

5.4.4 MS COCO

Microsoft has recently released the Common Objects in Context dataset, which contains 80k training images ("2014 train") and 40k validation images ("2014 val"). There is an associated MS COCO challenge with a new evaluation metric, that averages mAP over different IoU thresholds, from 0.5 to 0.95 (written as "0.5:0.95"). This places a significantly larger emphasis on localization compared to the PASCAL VOC metric which only requires IoU of 0.5.

We are only aware of one baseline performance number for this dataset, as published in the Fast R-CNN paper, which cites a mAP of 19.7% on the 2015 test-dev set [65]. We trained our own Fast R-CNN model on "2014 train" using our longer training schedule and obtained a higher mAP of 20.5% mAP on the same set, which we use as a baseline. As shown in Table 5.3, when trained on the same images with the same schedule, our method obtains a large improvement over the baseline with a mAP of 24.9%.

Applying box voting [60] gives us a further improvement (+1.6 mAP) on the original PASCAL VOC metric (IoU 0.5), but interestingly decreases performance (-0.3 mAP) on the new COCO metric (IOU 0.5:0.95). We note that this effect is entirely due to the change in metric, which weights localization errors differently. As described in the Supplemental,[4] we fixed this for our competition submission by raising the box voting IoU threshold from 0.5 to ~ 0.85.

We submitted ION to the 2015 MS COCO Detection Challenge and won the Best Student Entry with 3rd place overall. Using only a single model (no ensembling), our submission achieved 31.0% on test-competition score and

[4] http://www.cs.cornell.edu/~sbell/

31.2% on test-dev score (Table 5.3). After the competition, we further improved our test-dev score to 33.1% by adding left-right flipping and adjusting training parameters. See the Supplemental,[5] for details on our challenge submission.

5.4.5 Improvement for small objects

In general, small objects are challenging for detectors: there are fewer pixels on the object, they are harder to localize, and there can be many more of them per image. Small objects are even more challenging for proposal methods. For all experiments, we are using selective search [177] for object proposals, which performs very poorly on small objects in COCO with an average recall under 10% [137].

We find that our detector shows a large relative improvement in this category. For COCO, if we look at small[6] objects, average precision and average recall improve from 4.1% to 7.0% and from 7.3% to 10.7% respectively. We highlight that this is even higher than the baseline proposal method, which is only possible because we perform bounding box regression to predict improved box locations. Similarly, we show a size breakdown for VOC2007 test in Figure 5.4 using Hoiem's toolkit for diagnosing errors [79], and see similarly large improvements on this dataset as well.

ROI pooling from:				Merge features using:	
C2	C3	C4	C5	1x1	L2+Scale+1x1
			✓	*70.8	71.5
		✓	✓	69.7	74.4
	✓	✓	✓	63.6	**74.6**
✓	✓	✓	✓	59.3	**74.6**

Table 5.4: **Combining features from different layers.** Metric: Detection mAP on VOC07 test. Training set: 07 trainval + 12 trainval. **1x1**: combine features from different layers using a 1x1 convolution. **L2+Scale+1x1**: use L2 normalization, scaling (initialized to 1000), and 1x1 convolution, as described in section 5.3.1. These results do not include "context features." *This entry is the same as Fast R-CNN [65], but trained with our hyperparameters.

5.5 Design evaluation

In this section, we explore changes to our architecture and justify our design choices with experiments on PASCAL VOC 2007. All numbers in this section are VOC 2007 test mAP, trained on 2007 trainval + 2012 trainval, with the settings described in Section 5.4.1. Note that for this section, we use dropout in all networks, and a single round of bounding box regression at test time.

5.5.1 Pool from which layers?

As described in Section 5.3.1, our detector pools regions of interest (ROI) from multiple layers and combines the result. A straightforward approach would be to concatenate the ROI from each layer and reduce the dimensionality using a 1x1 convolution. As shown in Table 5.4 (left column), this does not work. In VGG16, the convolutional features at different layers can have very different amplitudes, so that naively combining them leads to unstable learning. While it

[5] Ibid

[6] "Small" means area $\leq 32^2$ px; about 40% of COCO is "small."

L2 Normalization method	Seg.	Scale: Learned	Scale: Fixed
Sum across channels	✓	76.4	76.2
Sum over all entries	✓	76.5	**76.6**

Table 5.5: **Approaches to normalizing feature amplitude.** Metric: VOC07 test mAP. All items regularized with segmentation labels.

is possible in theory to learn a model with inputs of very different amplitude, this is ill-conditioned and does not work well in practice. It is necessary to normalize the amplitude such that the features being pooled from all layers have similar magnitude. Our method's normalization scheme fixes this problem, as shown in Table 5.4 (right column).

5.5.2 How should we normalize feature amplitude?

When performing L2 normalization, there are a few choices to be made: do you sum over channels and perform one normalization per spatial location (as in ParseNet [116]), or should you sum over all entries in each pooled ROI and normalize it as a single blob. Further, when re-scaling the features back to an fc6-compatible magnitude, should you use a fixed scale or should you learn a scale per channel? The reason why you might want to learn a scale per channel is that you get more sharing than you would if you relied on the 1x1 convolution to model the scale. We evaluate this in Table 5.5, and find that all of these approaches perform about the same, and the distinction doesn't matter for this problem. The important aspect is whether amplitude is taken into account; the different schemes we explored in Table 5.5 are all roughly equivalent in performance.

ROI pooling from:					Use seg. loss?	
C2	C3	C4	C5	IRNN	No	Yes
				✓	69.9	70.6
			✓	✓	73.9	74.2
		✓	✓	✓	75.1	76.2
	✓	✓	✓	✓	75.6	76.5
✓	✓	✓	✓	✓	74.9	**76.8**

Table 5.6: **Effect of segmentation loss.** Metric: detection mAP on VOC07 test. Adding segmentation loss tends to improve detection performance by about 1 mAP, with no test-time penalty.

To determine the initial scale, we measure the mean scale of features pooled from conv5 on the training set, and use that as the fixed scale. Using Fast R-CNN, we measured the mean norm to be approximately 1000 when summing over all entries, and 130 when summing across channels.

5.5.3 How much does segmentation loss help?

Although our target task is object detection, many datasets also have semantic segmentation labels, where the object class of every pixel is labeled. Many images in PASCAL VOC and every image in COCO has these labels. This is valuable information that can be incorporated into a training algorithm to improve performance.

As shown in Figure 5.2, when adding stacked IRNNs it is possible to have them also predict a semantic segmentation output—a multitask setup. In Table 5.6, we see that these extra labels consistently provide about a +1 point boost in mAP for object detection. This is because we are training the network with more bits of supervision, so even though we are adding extra labels that we do not care about during inference, the features inside the network are trained to

Context method	Seg.	mAP
(a) 2x stacked 512x3x3 conv		74.8
(b) 2x stacked 256x5x5 conv		74.6
(c) Global average pooling		74.9
(d) 2x stacked 4-dir IRNN		**75.6**
(a) 2x stacked 512x3x3 conv	✓	75.2
(d) 2x stacked 4-dir IRNN	✓	**76.5**

Table 5.7: **Comparing approaches to adding context.** All rows also pool out of conv3, conv4, and conv5. Metric: detection mAP on VOC07 test. **Seg:** if checked, the top layer received extra supervision from semantic segmentation labels.

contain more information than they would have otherwise if only trained on object detection. Since this is an extra layer used only for training, we can drop the layer at test time and get a +1 mAP point boost with no change in runtime.

5.5.4 How should we incorporate context?

While RNNs are a powerful mechanism of incorporating context, they are not the only method. For example, one could simply add more convolutional layers on top of conv5 and then pool out of the top convolutional layer. As shown in Figure 5.5, stacked 3x3 convolutions add two cells worth of context, and stacked 5x5 convolutions add 4 cells. Alternatively, one could use a global average and unpool (tile or repeat spatially) back to the original shape as in ParseNet [116].

We compared these approaches on VOC 2007 test, shown in Table 5.7. The 2x stacked 4-dir IRNN layers have fewer parameters than the alternatives, and perform better on the test set (both with and without segmentation labels). Therefore, we use this architecture to compute "context features" for all other experiments.

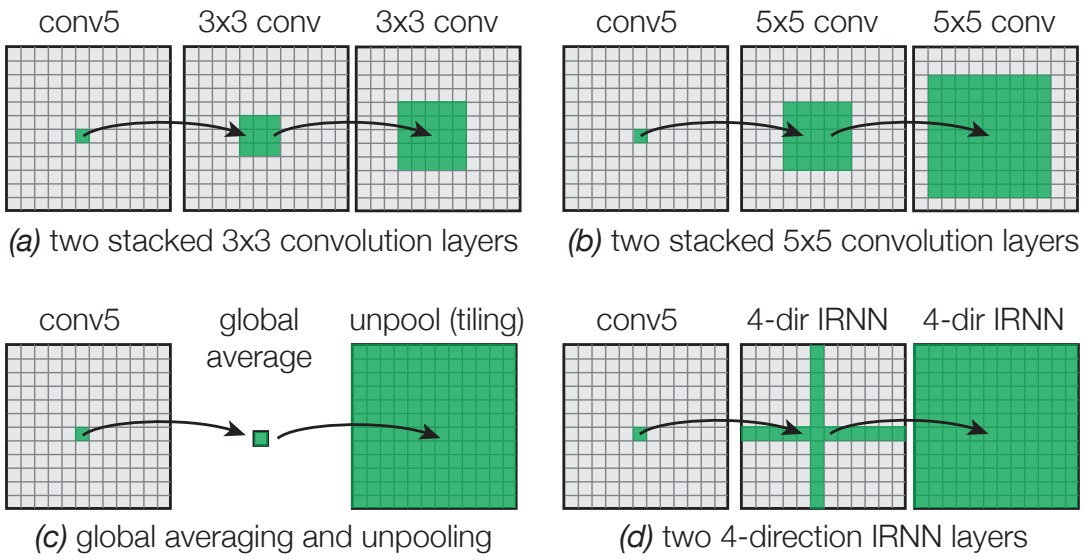

Figure 5.5: **Receptive field of different layer types.** When considering a single cell in the input, what output cells depend on it? **(a)** If we add two stacked 3x3 convolutions on top of conv5, then a cell in the input influences a 5x5 window in the output. **(b)** Similarly, for a 5x5 convolution, one cell influences a 9x9 window in the output. **(c)** For global average pooling, every cell in the output depends on the entire input, but the output is the same value repeated. **(d)** For IRNNs, every cell in the output depends on the entire input, but also varies spatially.

5.5.5 Which IRNN architecture?

When designing the IRNN for incorporating context, there are a few basic decisions to be made, namely how many layers and how many hidden units per layer. In addition, we explore the idea of entirely removing the recurrent transition (equivalent to replacing it with the identity matrix), so that the IRNN consist of repeated steps of: accumulate, ReLU, accumulate, etc.. Note that this is not the same as an integral/area image, since each step has ReLU.

As shown in Table 5.8, the number of hidden units does not have a strong effect on the performance (Table 5.8), so we choose 512 as the baseline size for all other experiments. In the Supplemental,[7] we include additional experiments

[7] http://www.cs.cornell.edu/~sbell/

ROI pooling from: C3	C4	C5	IRNN	Seg.	# units	Include $\mathbf{W}_{hh}$? Yes	No
✓	✓	✓	✓	✓	128	76.4	75.5
✓	✓	✓	✓	✓	256	**76.5**	75.3
✓	✓	✓	✓	✓	512	**76.5**	76.1
✓	✓	✓	✓	✓	1024	76.2	76.4

Table 5.8: **Varying the hidden transition.** We vary the number of units and try either learning recurrent transition $\mathbf{W}_{hh}$ initialized to the identity, or entirely removing it (same as setting $\mathbf{W}_{hh} = I$).

showing that 2 IRNN layers is optimal on VOC 2007 test. While stacking more convolution layers tends to make ConvNets perform better, the same is not always true for RNNs [89].

Finally, we were surprised to discover that removing the recurrent $\mathbf{W}_{hh}$ transition performs almost as well as learning it (Table 5.8). It seems that the input-to-hidden and hidden-to-output connections contain sufficient context that the recurrent transition can be removed and replaced with an addition, saving a large matrix multiply.

5.5.6 Other variations

There are some other variations on our architecture that perform almost as well, which we summarize in Table 5.9. For example, (a) the first IRNN only processes two directions left/right and the second IRNN only processes up/down. This kind of operation was explored in ReNet [184] and performs the same as modeling all four directions in both IRNN layers. We also explored (b) pooling out of both IRNNs, and (c) pooling out of both stacked convolutions and the IRNNs. None of these variations perform better than our main method.

Variation	mAP
Our method	**76.5**
(a) Left-right then up-down	**76.5**
(b) Pool out of both IRNNs	75.9
(c) Combine 2x stacked 512x3x3 conv and IRNN	**76.5**

Table 5.9: **Other variations.** Metric: VOC07 test mAP. We list some other variations that all perform about the same.

5.6 Conclusion

This paper introduces the Inside-Outside Net (ION), an architecture that leverages context and multi-scale knowledge for object detection. Our architecture uses a 2x stacked 4-directional IRNN for context, and multi-layer ROI pooling with normalization for improved object description. To justify our design choices, we conducted extensive experiments evaluating choices like the number of layers combined, using segmentation loss, normalizing feature amplitudes, different IRNN architectures, and other variations. We achieve state-of-the-art results on both PASCAL VOC and COCO, and find our proposed architecture is particularly effective at improving detection of small objects.

5.7 Impact

Our work in this chapter was first presented at the MS COCO 2015 Detection Challenge, where we won Best Student Entry, and later published as a paper at CVPR 2016 [15]. Concurrently with our work, the second place entry in the MS COCO competition revisited skip connections with a similar architecture [196]. Our ION architecture has inspired similar approaches of combining skip pooling and context to obtain more accurate results [204].

CHAPTER 6

LEARNING VISUAL SIMILARITY FOR PRODUCT DESIGN WITH CONVOLUTIONAL NEURAL NETWORKS

6.1 Introduction

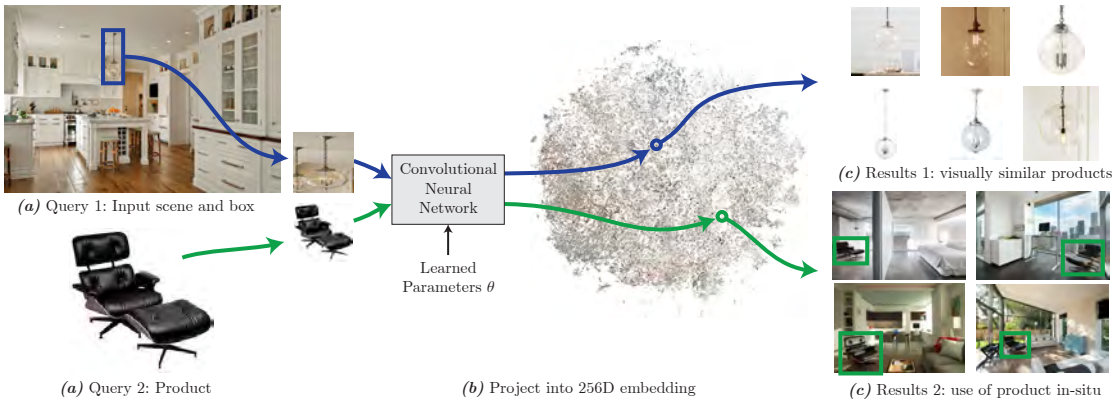

Figure 6.1: *Visual search using a learned embedding*. Query 1: given an input box in a photo **(a)**, we crop and project into an embedding **(b)** using a trained convolutional neural network (CNN) and return the most visually similar products **(c)**. Query 2: we apply the same method to search for in-situ examples of a product in designer photographs. The CNN is trained from pairs of internet images, and the boxes are collected using crowdsourcing. The 256D embedding is visualized in 2D with t-SNE. Photo credit: Crisp Architects and Rob Karosis (photographer).

In this final chapter, we explore a higher level of visual abstraction in scene understanding—the question of which of which objects in scenes are visually similar. We pose this as a metric learning problem, which allows us to answer questions like "What is this product", "Where has this product been seen?", and "What products go together stylistically?" We use deep learning to learn this metric by training on thousands of pairs of images downloaded from the web and annotated using crowdsourcing.

Home owners and consumers are interested in visualizing ideas for home

improvement and interior design. Popular sites like Houzz, Pinterest, and LikeThatDecor have large active communities of users that browse the sites for inspiration, design ideas and recommendations, and to pose design questions. For example, some topics and questions that come up are:

- "What is this {chair, lamp, wallpaper} in this photograph? Where can I find it?", or, "Find me {chairs, ...} similar to this one." This kind of query may come from a user who sees something they like in an online image on Flickr or Houzz, a magazine, or a friend's home.
- "How has this armchair been used in designer photos?" Users can search for the usage of a product for design inspiration.
- "Find me a compatible chair matching this table." For example, a home owner is replacing furniture in their home and wants to find a chair that matches their existing table (and bookcase).

Currently, sites like Houzz have active communities of users that answer design questions like these with (sometimes informed) guesses. Providing automated tools for design suggestions and ideas can be very useful to these users.

The common thread between these questions is the need to find *visually similar* objects in photographs. In this chapter we learn a distance metric between an object *in-situ* (i.e., a sub-image of a photograph) and an *iconic* product image of that object (i.e., a clean well-lit photograph, usually with a white background). The distance is small between the in-situ object image and the iconic product image, and large otherwise. Learning such a distance metric is challenging because the in-situ object image can have many different backgrounds, sizes, orientations, or lighting when compared to the iconic product image, and, it

could be significantly occluded by clutter in the scene.

Recently, the area of deep learning using convolutional neural networks (CNNs) has made incredible strides in recognizing objects across a variety of viewpoints and distortions [167, 99]. Therefore, we build our method around this powerful tool to learn functions that can reason about object similarity across wide baselines and wide changes in appearance. To apply deep learning, however, we need ground truth data to train the network. We use crowdsourcing to collect matching information between in-situ images and their corresponding iconic product images to generate the data needed to train deep networks.

We make the following contributions:

- We develop a crowdsourced pipeline to collect pairings between in-situ images and their corresponding product images.
- We show how this data can be combined with a siamese CNN to learn a high quality embedding. We evaluate several different training methodologies including: training with contrastive loss, object classification softmax loss, training with both, and the effect of normalizing the embedding vector.
- We apply this embedding to image search applications like finding a product, finding designer scenes that use a product, and finding visually similar products across categories.

Figure 3.2 illustrates how our visual search works. On the left are two types of queries: (1) an object in a scene marked with a box and (2) an iconic product image. The user sends the images as queries to the CNN we have learned. The queries map to different locations in our 256D learned embedding (visualized in the middle). A nearest neighbor query in the embedding produces the results on

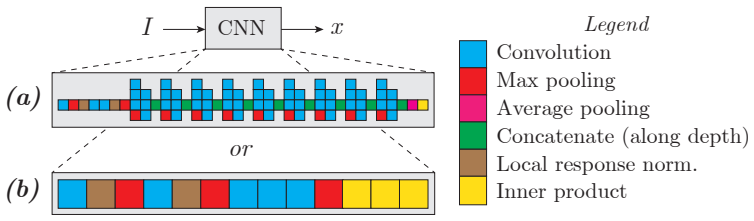

Figure 6.2: *CNN architectures:* **(a)** GoogLeNet and **(b)** AlexNet. Either CNN consists of a series of simple operations that processes the input I and produces a descriptor x. Operations are performed left to right; vertically stacked operations can be computed in parallel. This is only meant to give a visual overview; see [167] and [99] for details including kernel sizes, layer depths, added nonlinearities, and dropout regularization. Note that there is no "softmax" layer; it has been removed so that the output is the D-dimensional vector x.

the right, our visually similar objects. For query 1, we search for iconic products, and for query 2 we search for usages of a product in designer scenes. We include complete results for visual search and embeddings in the supplemental and on our website (http://productnet.cs.cornell.edu).

6.2 Related Work

There are many bodies of related work; we focus on learning similarity metrics and visual search, and deep learning using CNNs.

Learning similarity metrics and visual search. Metric learning is a rich area of research; see [100] for a survey. One of the most successful approaches is OASIS [28] which solves for a bi-linear similarity function given triplet judgements. In the area of graphics, metric learning has been applied to illustration style [56] and font similarity [125]. Complementary to metric learning are *attributes*, which assign semantic labels to vector directions or regions of the input feature space. Whittle search uses relative attributes for product search [132, 95],

Furniture-geek [130] understands fine-grained furniture attributes. In addition to modeling visual similarity, there are many approaches to solving the *instance* retrieval problem. For example, Girod et al. [64] use the CHoG descriptor to match against millions of images of CDs, DVDs, and book covers. Many papers have built methods around feature representations including Fisher Vectors [136] and VLAD [84]. In contrast to the above approaches that mostly use "hand-tuned" features, we want to learn features end-to-end directly from input pixels, using convolutional neural networks.

In industry, there have been examples of instance retrieval for different problem domains like books and movies. Proprietary services like Google Goggles and Amazon Flow attempt to handle any arbitrary input image and recognize specific products. Other services like TinEye.com perform "reverse image search" to find near-duplicates across the entire internet. In contrast, we focus on modeling a higher level notion of visual similarity.

Convolutional neural networks (CNNs). A full review of deep learning and convolutional neural networks is beyond the scope of this thesis; please see [27]. Here, we cover the most relevant background, and focus our explanation to how we use this tool for our problem. CNNs are functions for processing images, consisting of a number of stages ("layers") such as convolution, pooling, and rectification, where the parameters of each stage are learned to optimize performance on some task, given training data. While CNNs have been around for many years, with early successes such as LeNet [106], it is only recently that they have shown competitive results for tasks such as object classification or detection. Driven by the success of Krizhevsky et al. [99]'s "SuperVision" submission to the ILSVRC2012 image classification challenge, there has been

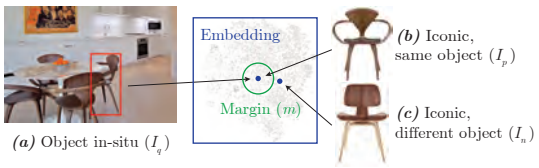

Figure 6.3: Our goal is to learn an embedding such that the object in-situ **(a)** and an iconic view of an object **(b)** map to the same point. We also want different objects **(c)** to be separated by at least a margin m, even if they are similar. Photo credit: Austin Rooke.

an explosion of interest in CNNs, with many new architectures and approaches being presented.

For our work, we focus on two recent successful architectures: AlexNet (a.k.a. "SuperVision") [99] and GoogLeNet [167]. AlexNet has 5 convolutional layers and 3 inner product layers, and GoogLeNet has many more layers. Both networks are very efficient and can be parallelized on modern GPUs to process hundreds of images per second. Figure 6.2 gives a schematic of these two networks.

In addition to image classification, CNNs have been applied to many problems in computer vision and show state-of-the-art performance in areas including classifying image photography style [88], recognizing faces [168], and ranking images by fine-grained similarity [187]. CNNs have been shown to produce high quality image descriptors that can be used for visual instance retrieval, even if they were trained for object classification [4, 142].

6.3 Background: learning a distance metric with siamese networks

In this section, we provide a brief overview of the theory behind siamese networks and contrastive loss functions [71], and how they may be used to train a similarity metric from real data.

Given a convolutional neural network (such as AlexNet or GoogLeNet), we can view the network as a function f that maps each image I into an embedding position x, given parameters θ: $x = f(I; \theta)$. The parameter vector θ contains all the weights and biases for the convolutional and inner product layers, and typically contains 1M to 100M values. The goal is to solve for the parameter vector θ such that the embedding produced through f has desirable properties and places similar items nearby.

Consider a pair of images (I_q, I_p) that are two views of the same object, and a pair of images (I_q, I_n) that show different objects. We can map these images into our embedding to get x_q, x_p, x_n. If we had a good embedding, we would find that x_q and x_p are nearby, and x_q and x_n are further apart. This can be formalized as the contrastive loss function L, which measures how well f is able to place similar images nearby and keep dissimilar images separated. As implemented in Caffe [85], L has the form:

$$L(\theta) = \underbrace{\sum_{(x_q, x_p)} L_p(x_q, x_p)}_{\substack{\text{Penalty for similar images} \\ \text{that are far away}}} + \underbrace{\sum_{(x_q, x_n)} L_n(x_q, x_n)}_{\substack{\text{Penalty for dissimilar} \\ \text{images that are nearby}}} \tag{6.1}$$

$$L_p(x_q, x_p) = \|x_q - x_p\|_2^2 \tag{6.2}$$

$$L_n(x_q, x_n) = \max\left(0, m^2 - \|x_q - x_n\|_2^2\right) \tag{6.3}$$

The loss consists of two penalties: L_p penalizes a positive pair (x_q, x_p) that is too far apart, and L_n penalizes a negative pair (x_q, x_n) that is closer than a margin m. If a negative pair is already separated by m, then there is no penalty for that pair and $L_n(x_q, x_n) = 0$.

To improve the embedding, we adjust θ to minimize the loss function L, which can be done with stochastic gradient descent with momentum [99] as follows:

$$v^{(t+1)} \leftarrow \mu \cdot v^{(t)} - \alpha \cdot \frac{\partial L}{\partial \theta}\left(\theta^{(t)}\right) \tag{6.4}$$

$$\theta^{(t+1)} \leftarrow \theta^{(t)} + v^{(t+1)} \tag{6.5}$$

where $\mu \in [0, 1)$ is the momentum and $\alpha \in [0, \infty)$ is the learning rate. We use mini-batch learning, where L is approximated by only considering a handful of examples each iteration.

The remaining challenge is computing L and $\frac{\partial L}{\partial \theta}$. Hadsell et al. [71] showed that an efficient method of computing and minimizing L is to construct a *siamese network* which is two copies of the CNN that share the same parameters θ. An indicator variable y selects whether each input pair I_1, I_2 is a positive ($y = 1$) or negative ($y = 0$) example. This entire structure can now be viewed as a new bigger network that consumes inputs I_1, I_2, y, θ and outputs L. With this view, it is now straightforward to apply the backpropagation algorithm [149] and efficiently compute the gradient $\frac{\partial L}{\partial \theta}$.

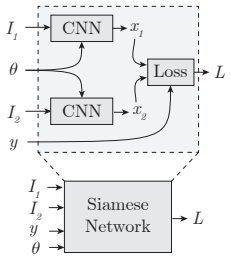

Figure 6.4: Siamese network abstraction.

For all of our experiments, we use Caffe [85], which contains efficient GPU implementations for training CNNs.

6.4 Our approach

For our work, we build a database of millions of products and scenes downloaded from Houzz.com. We focus on learning a single embedding that contains two types of images: in-situ examples of products I_q (cropped sub-images) and iconic product images I_p, as shown in Figure 6.3. Rather than hand-design the mapping $I_q \mapsto x_q$, we use a siamese network, described above, to automatically learn a mapping that is both high quality and fast to compute.

While siamese architectures [71] are quite effective, there are many ways to train the weights for a CNN. We explore different methods of training an embedding as shown in Figure 6.5. Some of these variations have been used before; for example, Razavian [142] used architecture **A** for instance retrieval, Chopra [34] used **B** for identity verification, Wang [187] used a triplet version of **B** with L2 normalization for fine-grained visual similarity, and Weston [192] used **C** for MNIST digits and semantic role labeling. We evaluate these architectures on a real-world internet dataset.

To train our CNN, we explore a new source of training data. We collect a hundred thousand examples of matching in-situ products and their iconic images. We use MTurk to collect the necessary in-situ bounding boxes for each product (Section 6.5). We then train multiple CNN architectures using this data and compare different multitask loss functions and different distance metrics. Finally, we demonstrate how the learned mapping can be used in visual search applications both across all object categories and within specific categories (Section 6.6). We perform searches in two directions, returning either product images or in-situ products in scenes.

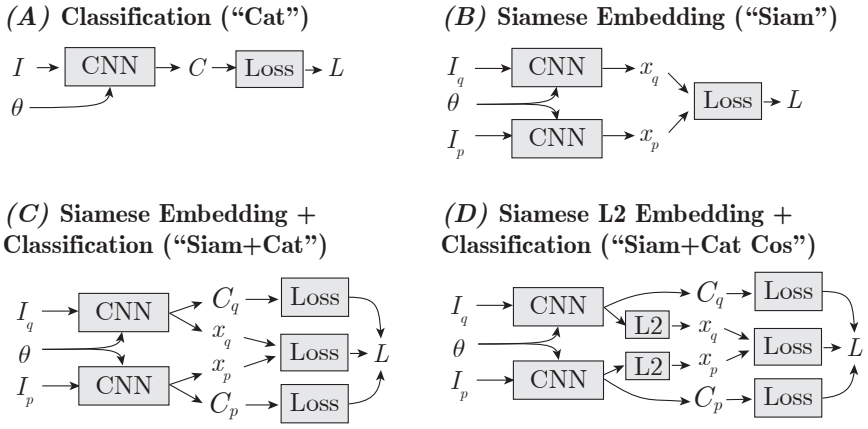

Figure 6.5: *Training architectures.* We study the effect of several training architectures: (**A**) a CNN that is used for classification and then re-purposed as an embedding, (**B**) directly training an embedding, (**C**) also predicting the object categories C_q, C_p, and (**D**) also normalizing the embedding vectors to have unit L2 length (since Euclidean distance on normalized vectors is cosine distance). Loss for classification: softmax loss (softmax followed by cross-entropy); loss for embedding: contrastive loss.

6.5 Learning our visual similarity metric

In this section, we describe how we build a new dataset of positive and negative examples for training, how we use crowdsourcing to label the extent of each object, and how we train the network. Finally, we visualize the resulting embedding and demonstrate that we have learned a powerful visual similarity metric.

6.5.1 Collecting Training Data

Training the networks requires positive and negative examples of matching in-situ images and iconic product images. A great resource for such images exist at websites like Houzz.com; the site contains millions of photos of both rooms and products. Many of the rooms contain product tags, where a "pro" user has

annotated a product inside a room. The annotation can include a description, another photo, and/or a link to where the product may be purchased. For example, Figure 6.6 shows an example photo with several tags; two of which contain links to photos.

Images. To build our database, we recursively browsed pages on Houzz.com, downloading each photo and its metadata. In total, we downloaded 7,249,913 product photos and 6,515,869 room photos. Most products have an object category that is generally correct, which we later show can be used to improve the training process. Before we can use the data, we must detect duplicate and near-duplicate images; many images are uploaded thousands of times, sometimes with small variations. To detect both near- and exact-duplicates, we pass the images through AlexNet [99] and extract the output from the 7th layer (`fc7`), which has been shown to be a high quality image descriptor [4]. We cluster any two images that have nearly identical descriptors, and then keep only one copy (the one with the most metadata). As a result, we retained 3,387,555 product and 6,093,452 room photos.

Product tags. Out of the 3,387,555 product photos, 178,712 have "product tags", where a "pro" user has marked an object in-situ with its corresponding iconic product photo. This gives us a single point, but we want to know the spatial extent of the product in the room. Further, many of these tags are incorrect or the result of spam. We use crowdsourcing to (a) provide a tight bounding box around each tagged in-situ object and (b) clean up invalid tags.

(a) Full scene *(b)* Iconic product images

Figure 6.6: Example product tags from in-situ objects to their products (Houzz.com), highlighted with blue circles. Two of the five tags contain iconic photos of the product. Photo credit: Fiorella Design.

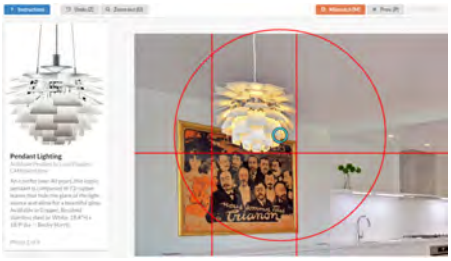

Figure 6.7: *MTurk interface.* A video of the interface and instructions are included in the supplemental (`http://www.seanbell.ca/tmp/siggraph2015-supplemental-bell-bala.zip`). Photo credit: Austin Rooke.

Crowdsourcing object extents

We chose to have workers draw bounding boxes instead of full polygon segments, as in Microsoft COCO [111] or OpenSurfaces [12], since bounding boxes are cheaper to acquire and we want training data of the same form as our final user input (bounding boxes).

We designed a single MTurk task where workers are shown an iconic view of a product on the left, and the product in-situ on the right (see Figure 6.7). We show the location of the tag as an animated blue circle, to focus the worker's attention on the correct object (e.g., if there are multiple copies). See the supplemental[1] for a sample video of the user interface. We then ask the worker to either draw a tight bounding box around the object, or flag the pair as a mismatched item

[1] `http://www.seanbell.ca/tmp/siggraph2015-supplemental-bell-bala.zip`

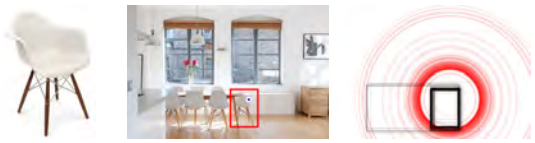

Figure 6.8: *Example sentinel*. Left: product image shown to workers. Center: ground truth box (red) and product tag location (blue circle). Right: 172 worker responses with bounding box (black) and circle (red), rendered with 20% opacity. Photo credit: Increation Interiors.

(to eliminate spam). Note that workers are instructed to only flag very obvious mismatches and allow small variations on the products. Thus, the ground truth tags often have a different color or material but are otherwise nearly the same product.

The size of the object in-situ in the image can vary considerably depending on the object, the viewpoint, etc. We collect the extent of each object in-situ by asking the worker to click *five* times: (1) workers first click to set a bounding circle around the object, (2) then workers click to place a vertical line on the left/right edge of the object, (3-5) workers place the remaining bounding lines on the right/left, top, bottom. The initial bounding circle lets us quickly adjust the zoom level to increase accuracy. This step is critical to let us handle the very large variation in size of the objects while giving the workers the visual detail they need to see to provide good input. We also found in testing that using infinite lines, instead of boxes, makes it easier to draw a box around oddly shaped items.

In addition, we added "undo" and "go back" buttons to allow workers to fix mistakes. At the end of the task, workers are shown all of their bounding boxes on a new page, and can click to redo any item. These features were used by 60.4% of the workers. Worker feedback for our interface was unanimously positive.

Quality control

When crowdsourcing on Mechanical Turk, it is crucial to implement rigorous quality control measures, to avoid sloppy work. Some workers intentionally submit random results, others do not read the instructions. We ensure quality results with two methods: sentinels and duplication [63]. Sentinels ensure that bad workers are quickly blocked, and duplication ensures that small mistakes by the remaining good workers are caught.

Sentinels. Sentinels are secret test items randomly mixed into each task. Users must agree with the ground truth by having an intersection-over-union (IOU) score of at least 0.7, $\text{IOU}(A, B) = \frac{|A \cap B|}{|A \cup B|}$. If users make at least n mistakes and have an accuracy less than $n \cdot 10\%$, $3 \leq n \leq 8$, we prevent the user from submitting. Thus, a worker who submits 3 incorrect answers in a row will be blocked immediately, but we will wait longer before blocking a borderline worker. We order the sentinels so that the most difficult ones are presented first, so bad workers will be blocked after submitting just a few tasks. In total, we have 248 sentinels, and 6 of them are listed in the instructions with the correct answer. Despite giving away some of the answers, 11.9% of workers were blocked by our sentinels.

Figure 6.8 shows the variety of responses obtained for a single sentinel. Note that this example appears slightly ambiguous, since there are multiple copies of the chair that the worker could annotate. However, we have asked the worker to label only the one with the blue dot (which is animated in the task to make it more salient). It is important that we get all workers to follow a single convention so that we can use worker agreement as a measure of success.

Duplication. Even if a worker is reliable, they may be given a difficult example, or they may make occasional small mistakes. Therefore, we collect two copies of every bounding box and check whether the workers agree. If the intersection-over-union (IOU) of the two boxes is above 0.7, then we choose the box from the worker with the higher average sentinel score. If the workers disagree, we collect more boxes (up to 5) until we find a pair of responses that agrees (IOU ≥ 0.7).

Results With 1,742 workers, we collected 449,107 total responses which were aggregated to 101,945 final bounding boxes for an average cost of $0.0251 per final box. An additional 2,429 tags were "mismatched", i.e., at least half of the workers labeled *mismatch*. Workers were paid $0.05 to label 7 boxes (1 of which is a sentinel) and spent an average of 17.1 seconds per response.

6.5.2 Learning a distance metric

From crowdsourcing, we have collected a dataset of positive examples—the same product in-situ and in an iconic image. We now describe how we convert this data into a full dataset, how we train the network, and finally visualize the resulting embedding.

Generating positive and negative training data

The contrastive loss function consists of two types of examples: positive examples of similar pairs and negative examples of dissimilar pairs. Figure 6.9 shows how the contrastive loss works for positive and negative examples respectively for

our domain. The gradient of the loss function acts like a force (shown as a red arrow) that pulls together x_p and x_q and pushes apart x_q and x_n.

We have 101,945 pairs of the form: (in-situ bounding box, iconic product image). This forms all of our positive examples (I_q, I_p). To build negative examples, we take each in-situ image I_q and pick 80 random product images of the same object category, and 20 random product images of a different category. We repeat the positive pair 5 times, to give a 1:20 positive to negative ratio. We also augment the dataset by re-cropping the in-situ images with different amounts of padding: {0, 8, 16, 32, 48, 64, 80} pixels, measured with respect to a fixed 256x256 square input shape (for example, 16 pixels of padding means that $1/8^{\text{th}}$ of each dimension is scene context).

We split all of these examples into training, validation, and test sets, making sure to separate bounding boxes by photo to avoid any contamination. This results in 63,820,250 training and 3,667,769 pairs. We hold out 6,391 photos for testing which gives 10,000 unseen test bounding boxes. After splitting the examples, we randomly shuffle the pairs within each set.

Training the network

Various parameter choices have to be made when training the CNN.

Selecting the training architecture. As shown earlier in Figure 6.5, we explore multiple methods of training the CNN: (**A**) training on only category labels (no product tags), (**B**) training on only product tags (no category labels), (**C**) training on both product tags and category labels, and (**D**) addi-

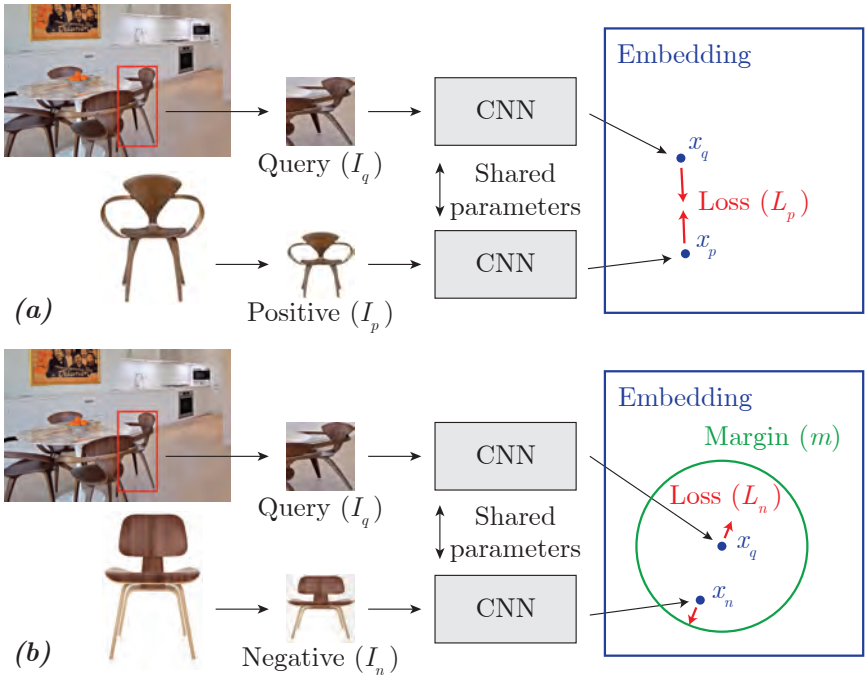

Figure 6.9: *Training procedure.* In each mini-batch, we include a mix of **(a)** positive and **(b)** negative examples. In each iteration, we take a step to decrease the loss function; this can be viewed as "forces" on the points (red arrows). Photo credit: Austin Rooke.

tionally normalizing the embedding to unit L2 length. In the supplemental (`http://www.seanbell.ca/tmp/siggraph2015-supplemental-bell-bala.zip`) we detail the different training parameters for each architecture (learning rate, momentum, etc.).

Selecting the margin. The margin m, in the contrastive loss function, can be chosen arbitrarily, since the CNN can learn to globally scale the embedding proportional to m. The only important aspect is the relative scale of the margin and the embedding, at the time of initialization. Making the margin too large can make the problem unstable and diverge; making it too small can make learning too slow. Therefore, we try a few different margins $m \in \{1, \sqrt{10}, \sqrt{100}, \sqrt{1000}\}$ and select the one that performs best. When using L2 normalization (Figure 6.5(d)), we use $m = \sqrt{0.2}$.

Initializing the network parameters. We are training with stochastic gradient descent (SGD); the choice of initialization can have a large impact on both the time taken to minimize the objective, and on the quality of the final optimum. It has been shown that for many problem domains [141], transfer learning (training the network to a different task prior to the final task) can greatly improve performance. Thus, we use networks that were trained on a large-scale object recognition benchmark (ILSVRC2012), and use the learned weights hosted on the BVLC Caffe website [85] to initialize our networks.

To convert the network used for object classification to one for embedding, we remove the "softmax" operation at the end of the network and replace the last layer with an inner product layer with a D-dimensional output. Since the network was pre-trained on warped square images, we similarly warp our queries. We try multiple dimensions $D \in \{256, 1024, 4096\}$. Later we describe how we quantitatively evaluate performance and select the best network.

Visualizing the embedding

After the network has converged, we visualize the result by projecting our D-dimensional embedding down to two dimensions using the t-SNE algorithm [179]. As shown in Figure 6.10, we visualize our embedding (trained with architecture **D**) by pasting each photo in its assigned 2D location.

When visualizing all products on the same 2D plane, we see that they are generally organized by object category. Further, when considering the portion of the plane occupied by a specific category, the products appear to be generally organized by some notion of visual style, even though the network was not trained

Figure 6.10: *2D embedding visualization using t-SNE [179].* This embedding was trained using architecture **D** and is 256D before being non-linearly projected to 2D. To reduce visual clutter, each photo is snapped to a grid (overlapping photos are selected arbitrarily). Full embeddings are in the supplemental (http://www.seanbell.ca/tmp/siggraph2015-supplemental-bell-bala.zip), including those for a single object category. Best viewed on a monitor.

to model the concept of "style". The supplementary material[2] includes more visualizations of embeddings including embeddings computed for individual object classes. These are best viewed on a monitor.

6.6 Results and applications

We now qualitatively and quantitatively evaluate the results. We demonstrate visual search in three applications: finding similar products, in-situ usages of a product, and visually similar products across different object categories.

[2] http://www.seanbell.ca/tmp/siggraph2015-supplemental-bell-bala.zip

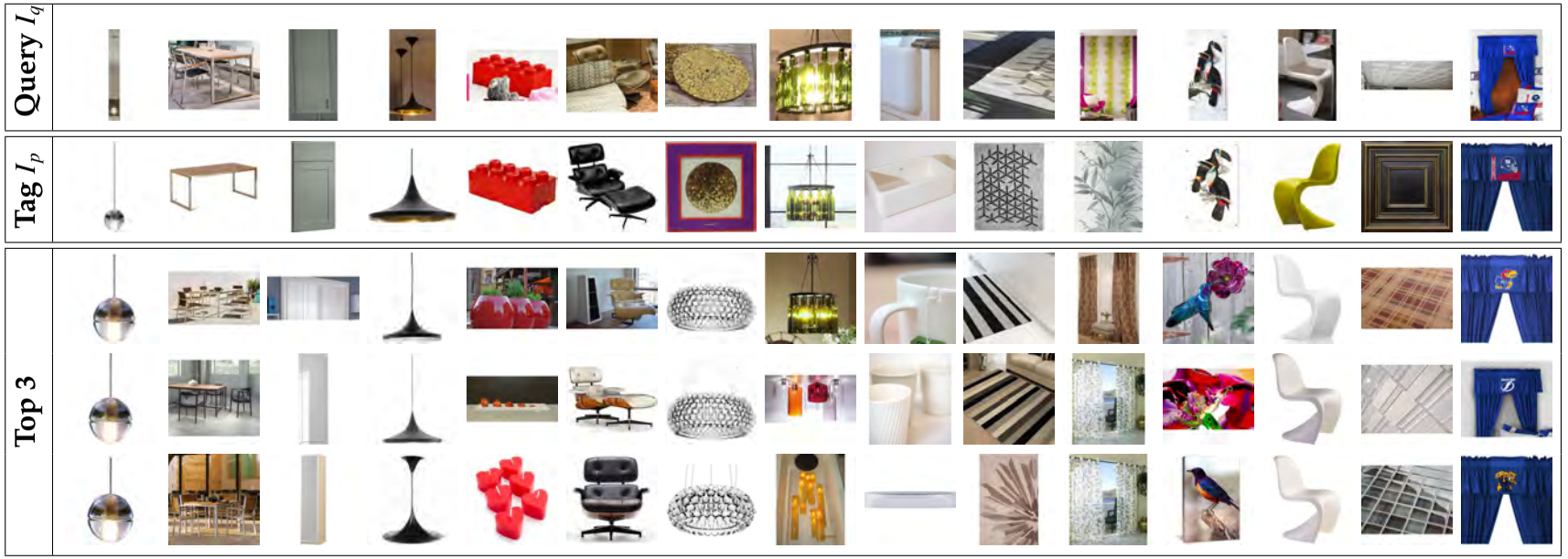

Table 6.1: *Product search: uncurated random queries from the test set*. For each query I_q, we show the top 3 retrievals using our method as well as the tagged canonical image I_p from Houzz.com. Object categories are not known at test time. Note that sometimes the retrieved results are closer to the query than I_p.

6.6.1 Visual search

Product search. The main use of our projection $I_q \mapsto x_q$ is to look up visually similar images. Table 6.1 shows several example queries randomly sampled from the test set. The results are not curated and are truly representative of a random selection of our output results. The query object may be significantly occluded, rotated, scaled, or deformed; or, the product image may be a schematic representation rather than an actual photo; or, the in-situ image is of a glass or transparent object, and therefore visually very different from the iconic product image. Nonetheless, we find that our descriptor generally performs very well. In fact, in some cases our results are closer than the tagged iconic product image because the ground truth often shows related items of different colors. Usually when the search fails, it tends to still return items that are similar in some way. In the supplemental[3] we show 500 more random uncurated examples of searches returned from our test set.

In-situ search. Since we have a descriptor that can model both iconic and in-situ cropped images, we can search in the "reverse" direction, where the query is a product and the returned results are cropped boxes in scenes. We use the bounding boxes we already collected from crowdsourcing as the database to search over. Figure 6.13 shows random examples sampled from the test set. Notice that since the scenes being searched over are designer photos, this becomes a powerful technique for exploring design ideas. For example, we could discover which tables go well with a chair by finding scenes that contain the chair and then looking for tables in the scenes.

[3] http://www.seanbell.ca/tmp/siggraph2015-supplemental-bell-bala.zip

Cross-category search. When retrieving very large sets of items for an input query, we found that when items show up from a different object category, these items tend to be visually or stylistically similar to the input query in some way. Despite not training the descriptor to reason about visual style, the descriptor is powerful enough to place stylistically similar items nearby in the space. We can explore this behavior further by explicitly searching only products of a *different* object category than the query (e.g. finding a table that is visually similar to a chair). Note that before we can do these sorts of queries, it is necessary to clean up the category labels on the dataset, since miscategorized items will show up in every search. Therefore, we use the "GN Cat" CNN (architecture **A**) [167] to predict a category for every product, and we remove all labels that either aren't in the top-20 or have confidence $\leq 1\%$. Table 6.2 shows example queries across a variety of object categories. These results are curated, since most queries do not have a distinctive style to them, and thus it is not apparent that anything has been matched. In the next section, we show a user study that evaluates to what extent our CNNs return stylistically similar items.

The product search and "in-situ" search are both trained with architecture **D**, and "cross-category" search uses architecture **B** (Figure 6.5). In the next section we detail how we quantitatively evaluated each architecture and selected the best.

6.6.2 Evaluating the metric

For our dataset, we cannot measure precision, since we only have a list of image positive pairs (in-situ image I_q and iconic product image I_p). However, we can

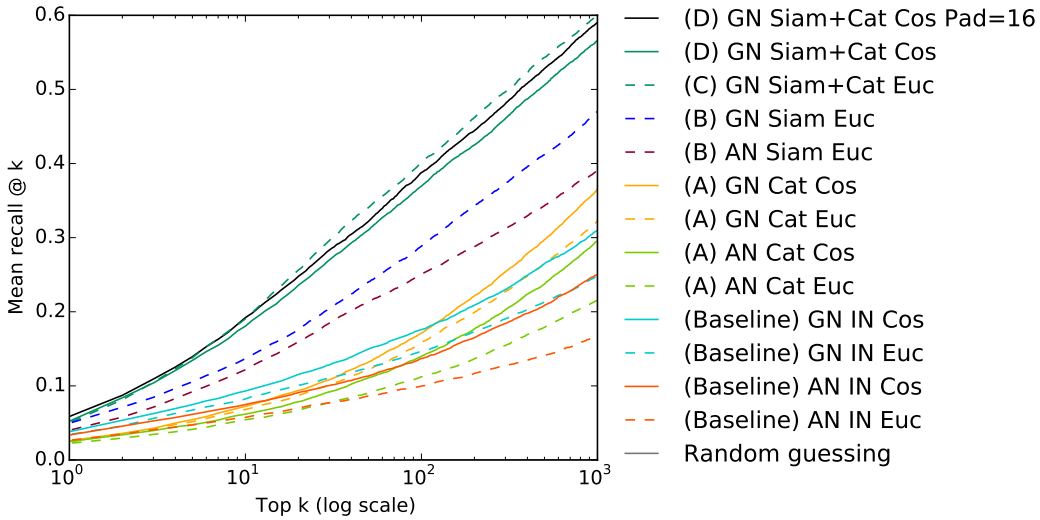

Figure 6.11: *Quantitative evaluation (log scale).* Recall (whether or not the single tagged item was returned) as a function of the number of items returned (k). Recall for each query is either 0 or 1, and is averaged across 10,000 items. "GN": GoogLeNet, "AN": AlexNet, "Euc": Euclidean distance, "Cos" cosine distance, "Siam": trained with a Siamese network, "Cat": trained with object categories, "IN": ImageNet weights (not trained at all), "P=16": the box is expanded so that after warping to a square, there are 16 pixels of padding. Random guessing is flat along the bottom.

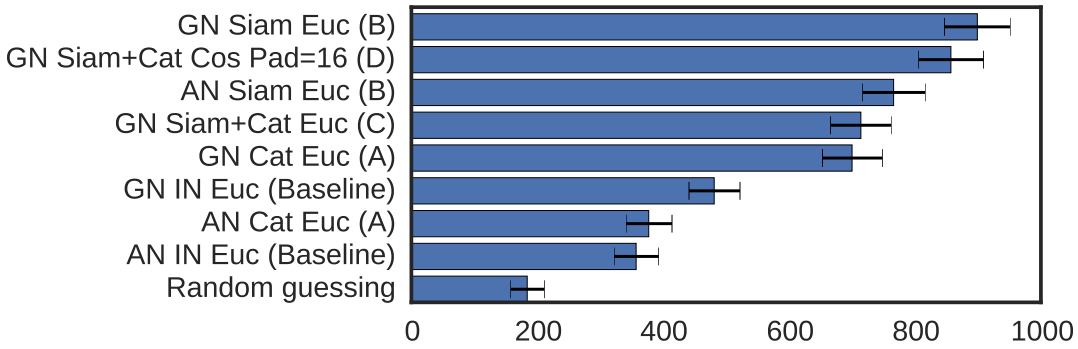

Figure 6.12: *User study for cross-category searches.* Number of times that a user clicked on the prediction from a given algorithm. Error bars: 95% confidence interval (bootstrap sampling). Naming conventions are explained in Figure 6.11.

measure recall of the product image—that is, we look at the closest k products to the query I_q and measure whether or not the tagged product I_p appears in the top k results. For each query, recall will be either 0 or 1; we average this over our test set of 10,000 pairs. We plot mean recall for each k in Figure 6.11.

Table 6.2: *Style search: example cross-category queries.* For each object category ("armchairs", "rugs", etc.), we show the closest product of that category to the input I_q, even though the input (usually) does not belong to that category. We show this for 12 different object categories. Note that object category is not used to compute the descriptor x_q; it is only used at retrieval time to filter the set of products.

It is important to note that image I_p is usually *not* the best match for I_q, as there is significant redundancy in the product images, even after accounting for near-duplicates. Often I_q and I_p differ in materials or in color. Nonetheless, a visual similarity metric should be able to deal with these issues, and place x_q and x_p reasonably close together in the embedding (so that its rank is small). So while a lower rank is better, a rank of 1 is not a reasonable expectation.

Baseline. To evaluate our embedding, we compare how well it can rank products compared to two high quality image descriptors for two different CNNs when trained on ImageNet ("IN"). For each CNN, we use the output from the last hidden layer and call them "AN IN" (i.e., AlexNet layer `fc7`) and "GN IN" (i.e., GoogLeNet layer `pool5/7x7_s1`). These two architectures are popular and have become the basis of a wide variety of state-of-the-art algorithms for image retrieval [4, 142]. We tried applying PCA since it has been shown that it can improve performance [142], but we found that it performed the same as the original descriptors, and thus is not shown.

Distance metrics. We compare two versions of each descriptor: a Euclidean version ("Euc") and a L2 normalized version ("Cos", since cosine distance is equal to Euclidean distance on normalized vectors). We evaluated other metrics including L1, Canberra, and Bray-Curtis dissimilarity on the baseline networks. We found that other metrics performed either comparably or worse than Cosine, and thus we only evaluate Cosine for the full dataset. For example, in Figure 6.11, "GN Cat Cos" means that we train GoogLeNet with object categories, and measure cosine distance using the last layer.

Padding. At test time, we experimented with adding different amounts of padding to the input query. We find that a modest amount of padding, 16 pixels, is optimal. Since all algorithms benefit from padding, we only show the effect on the best algorithm. The supplemental[4] includes our full padding evaluation.

Training architectures. As shown in Figure 6.11 the best architecture for image retrieval is **D**, which is a siamese GoogLeNet CNN trained on both image pairs and object category labels, with cosine as the distance metric. For all experiments, we find that GoogLeNet (GN) consistently outperforms AlexNet (AN), and thus we only consider variations of **C** and **D** using GoogLeNet. Architecture **A** is the commonly used technique of fine-tuning a CNN to the target dataset. It performs better than the ImageNet baselines, but not as well as any of the siamese architectures **B**, **C**, **D**. It might appear that **C** is the best curve (which is missing L2 normalization), but we emphasize that we show up to $k = 1000$ only for completeness and the top few results $k < 10$ matter the most (where **D** is the best).

Embedding dimension. We studied the effect of dimension on architecture **C**. Using more dimensions makes it easier to satisfy constraints, but also significantly increases the amount of space and time required to search. We find that 256, 1024, and 4096 all perform about the same, and thus use 256 dimensions for all experiments. See the supplemental[5] for the full curves.

Runtime. One of the key benefits of using CNNs is that computing $I_q \mapsto x_q$ is very efficient. Using a Grid K520 GPU (on an Amazon EC2 g2.2xlarge instance),

[4] http://www.seanbell.ca/tmp/siggraph2015-supplemental-bell-bala.zip

[5] Ibid.

we can compute x_q in about 100 ms, with most of the time spent loading the image. Even with brute force lookup (implemented as dense matrix operations), we can rank x_q against all 3,387,555 products in about one second on a single CPU. This can be accelerated using approximate nearest neighbor techniques [122], and is left for future work.

User study. As described in Section 6.6.1, Table 6.2 shows examples of cross-category searches. Since our siamese CNNs were trained on image pairs and/or object categories, it is unclear which (if any) should work as a style descriptor for this type of search. Therefore, we set up a user study where a user is shown an item of one category and 9 items of a second category (e.g. one chair in context, and 9 table product images) and instructed to choose the best match, stylistically. We run this experiment on MTurk, where each of the 9 items are generated by a different model (8 models, plus one random). Each grid of 9 items is shown to 5 users, and only grids where a majority agree on an answer are kept. The supplemental[6] contains screenshots of our user study. The results are shown in Figure 6.12, and we can see that all methods outperform random guessing, siamese architectures perform the best, and not training at all (baseline) performs the worst.

6.6.3 Discussion, limitations, and future work

There are many avenues to further improve the quality of our embedding, and to generalize our results.

[6] http://www.seanbell.ca/tmp/siggraph2015-supplemental-bell-bala.zip

Multitask predictions. We found that traning for object category along with the embedding performs the best for product search. Since the embedding and the object prediction are related by fully connected layers, the two spaces are similar. Thus, we effectively expand our training set of 86,945 pairs with additional 3,387,555 product category labels. At test time, we currently don't use the predicted object category—it is only a regularizer to improve the embedding. However, we could use the object category and use it to prune the set of retrieved results, potentially improving precision.

Style similarity vs. image similiarity. While we have not trained the CNN to model visual style, it seems to have learned a visual similarity metric powerful enough to place stylistically similar items nearby in the space. But style similarity and visual similarity are not the same. Two objects being visually similar often implies that they are also stylistically similar, but the converse is not true. Thus, if our embedding were to be used by designers interested in searching across compatible styles, we would need to explicitly train for this behavior. In future work, we hope to collect new datasets of style relationships to explore this behavior.

Active learning. We have a total of 3,387,555 product photos and 6,093,452 scene photos, but only 101,945 known pairs (I_q, I_p). As a result, dissimilar pairs of images that are not part of our known relationships may be placed nearby in the space, but there is no way to train or test for this. A human-in-the-loop approach may be useful here, where workers filter out false positives while training progresses. We propose exploring this in the future.

6.7 Conclusion

We have presented a visual search algorithm to match in-situ images with iconic product images. We achieved this by using a crowdsourcing pipeline for generating training data, and training a multitask siamese CNN to compute a high quality embedding of product images across multiple image domains. We demonstrated the utility of this embedding on several visual search tasks: searching for products within a category, searching across categories, and searching for usages of a product in scenes. Many future avenues of research remain, including: training to understand visual style in products, and improved faceted query interfaces, among others.

6.8 Impact

Since presenting our work on visual similarity at SIGGRAPH 2015, other researchers have shown that the approach presented in ProductNet also works for 3D shapes [109], clothing style [183], and sketches [154]. Buiding on the success of this approach, I am now co-founding a deep learning startup GrokStyle, based on this technology for visual search.

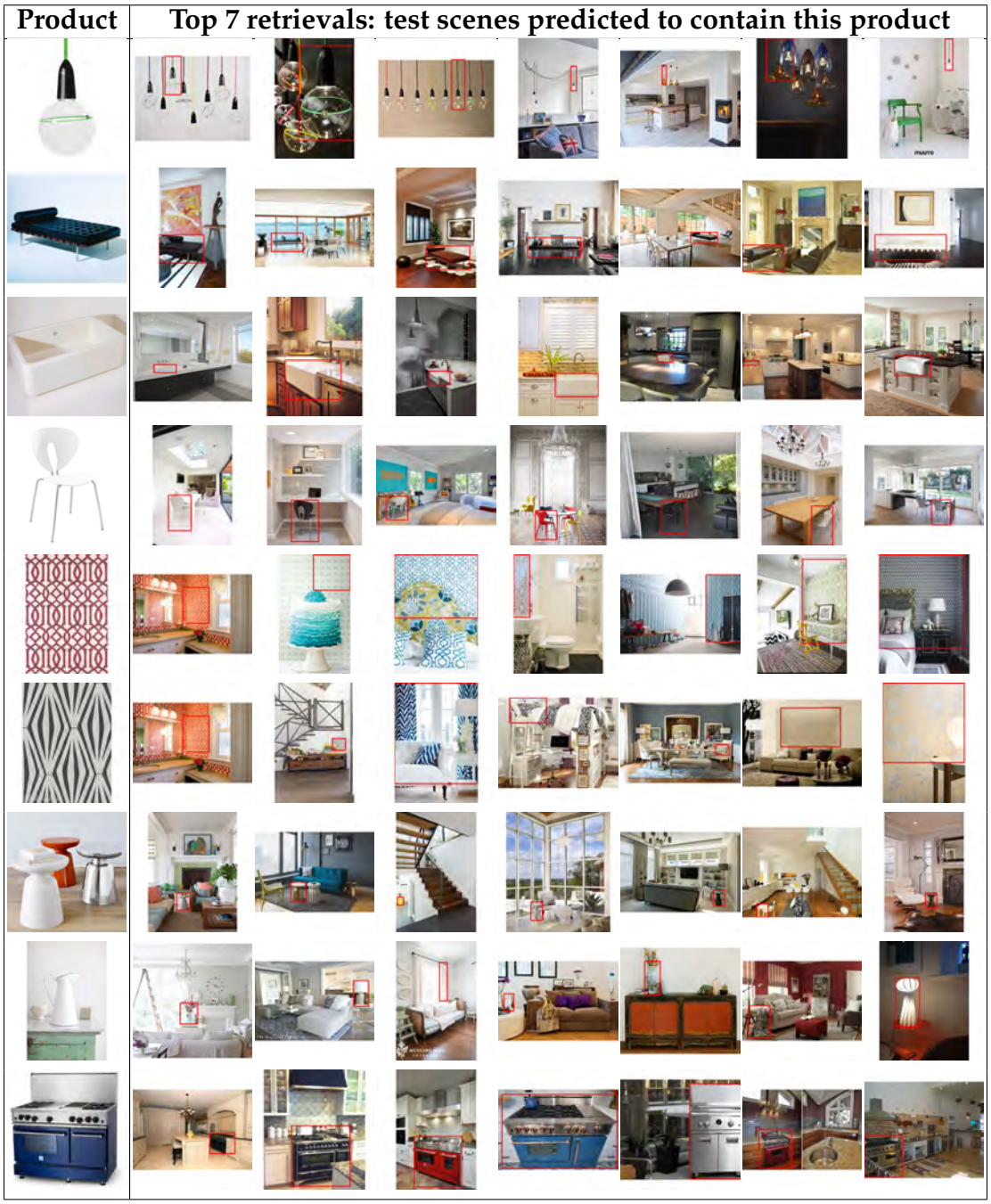

Figure 6.13: *In-situ product search: random uncurated queries searching the test set*. Here, the query is a product, and the retrievals are examples of where that product was used in designer images on the web. The boxes were drawn by mturk workers, for use in testing product search; we are assuming that the localization problem is solved. Also note that the product images (queries) were seen during training, but the scenes being searched over were not (since they are from the test set). When sampling random rows to display, we only consider items that are tagged at least 7 times (since we are showing the top 7 retrievals). We show many more in the supplemental (`http://www.seanbell.ca/tmp/siggraph2015-supplemental-bell-bala.zip`).

CHAPTER 7

CONCLUSION

The tools and data that we have for recognizing, editing, and exploring applying scene properties for everyday problems are slowly improving. As we develop more sophisticated methods of collecting data, train larger and richer models, we can solve increasingly important problems for humanity.

This thesis explores several directions that improve automatic scene understanding. In Chapter 2, we collected appearance information at a large-scale, which had not been done before for materials. In Chapters 3 and 4, we used this to inform and drive new algorithms to understand materials at pixel-level material categories and pixel-level reflectance. In Chapters 5 and 6, we developed higher level algorithms to detect objects in images, and recognized objects at a fine-grained per-object level. Together, these contributions significantly advance our knowledge of what information can be extracted from an image.

7.1 Impact

The work presented in this thesis has had a large impact on the community.

OpenSurfaces. Our annotations from OpenSurfaces have enabled others to train texture recognition and segmentation algorithms [37, 36], and to redecorate rooms by automatically suggesting materials for indoor digital scenes [29]. Our dataset has also been expanded with new "describable texture attributes" and re-released as an augmented dataset [36]. Researchers from Microsoft have used

our segmentation interface to power the Microsoft Commons Objects in Context (MS COCO) project [113] which labeled over 2.5 million objects; this data has significantly advanced the state-of-the-art in object detection as part of the yearly MS COCO object detection challenge.

IIW (Intrinsic Images in the Wild). Our IIW judgement dataset has been used to train and validate new models that use deep learning to predict reflectance and lightness variations in an image [203, 206, 123]. Using our data, others have proposed extensions of our algorithm that use deeply learned priors [203], or entirely new algorithms using global least squares optimizations [206], L1 image transforms [17], or near-L0 image transforms [44]. Our pairwise reflectance judgements have inspired others to extend our relative reflectance judgements to relative depth judgements [206] which can be globalized to solve for a full depth map.

MINC (Materials in Context). Our approach of using "click" labels to train semantic segmentation algorithms was later shown to yield a large improvement for objects, resulting in the most accurate models given a fixed annotation budget, out of squiggle-level, point-click, and full-image supervision [9]. Further, our MINC database has been used to train new state-of-the-art material recognition algorithms that go beyond the fully-connected CRF algorithm of Krähenbühl et al. [98] by directly learning pairwise potentials [83] or using "bilateral inceptions" [55]. Others have used our data to integrate multiple features obtained by different CNNs, obtaining close to human performance on the Flickr Material Dataset [160] with transfer learning [198].

ION (Inside-Outside Net). Our work in this chapter was first presented at the MS COCO 2015 Detection Challenge, where we won Best Student Entry, and later published as a paper at CVPR 2016 [15]. Concurrently with our work, the second place entry in the MS COCO competition revisited skip connections with a similar architecture [196]. Our ION architecture has inspired similar approaches of combining skip pooling and context to obtain more accurate results [204].

ProductNet. Since presenting our work on visual similarity at SIGGRAPH 2015, Other researchers have shown that the approach presented in ProductNet also works for 3D shapes [109], clothing style [183], and sketches [154]. Buiding on the success of this approach, I am now co-founding a deep learning startup GrokStyle, based on this technology for visual search of decor.

7.2 Future work

The scene understanding problem is still far from being solved. In particular, most methods, including our own, address one specific sub-problem at a time, such as material segmentation, intrinsic images, or object detection. In the future, we would like to explore jointly solving these problems, so that solutions for one problem can inform potentially ambiguous decisions in another problem. Further, it has been shown that for deep learning, jointly training multiple problems raises the accuracy of all of the individual sub-problems.

BIBLIOGRAPHY

[1] Andrew Adams, Jongmin Baek, and Abe Davis. Fast high-dimensional filtering using the permutohedral lattice. *Computer Graphics Forum (Eurographics)*, 29(2), 2010. 95

[2] Edward H. Adelson. On seeing stuff: the perception of materials by humans and machines. *Proc. SPIE Human Vision and Electronic Imaging*, 4299, 2001. 23

[3] Pulkit Agrawal, Ross Girshick, and Jitendra Malik. Analyzing the performance of multilayer neural networks for object recognition. In *ECCV*, 2014. 118

[4] Artem Babenko, Anton Slesarev, Alexander Chigorin, and Victor S. Lempitsky. Neural codes for image retrieval. In *ECCV*, 2014. 143, 148, 162

[5] Jonathan T. Barron and Jitendra Malik. Color constancy, intrinsic images, and shape estimation. In *ECCV*, 2012. 74

[6] Jonathan T. Barron and Jitendra Malik. Shape, albedo, and illumination from a single image of an unknown object. In *CVPR*, 2012. 74

[7] Jonathan T. Barron and Jitendra Malik. Intrinsic scene properties from a single rgb-d image. In *CVPR*, 2013. 75

[8] Jonathan T. Barron and Jitendra Malik. Shape, illumination, and reflectance from shading. Technical report, MIT, 2013. 74, 90, 91, 108

[9] Amy Bearman, Olga Russakovsky, Vittorio Ferrari, and Li Fei-Fei. What's the Point: Semantic Segmentation with Point Supervision. *ECCV*, 2016. 70, 169

[10] Sven Behnke. *Hierarchical Neural Networks for Image Interpretation*. PhD thesis, Freie Universität Berlin, 2003. 116

[11] Sean Bell, Kavita Bala, and Noah Snavely. Intrinsic images in the wild. *SIGGRAPH Conf. Proc.*, 33(4), 2014. 111

[12] Sean Bell, Paul Upchurch, Noah Snavely, and Kavita Bala. OpenSurfaces: A richly annotated catalog of surface appearance. *ACM Trans. on Graphics (SIGGRAPH)*, 32(4), 2013. xiv, 41, 48, 51, 53, 149

[13] Sean Bell, Paul Upchurch, Noah Snavely, and Kavita Bala. OpenSurfaces: A richly annotated catalog of surface appearance. *ACM Trans. on Graphics (SIGGRAPH)*, 32(4), 2013. 72, 75, 78

[14] Sean Bell, Paul Upchurch, Noah Snavely, and Kavita Bala. Material recognition in the wild with the materials in context database. *Computer Vision and Pattern Recognition (CVPR)*, 2015. 50, 70

[15] Sean Bell, C. Lawrence Zitnick, Kavita Bala, and Ross Girshick. Inside-outside net: Detecting objects in context with skip pooling and recurrent neural networks. *Computer Vision and Pattern Recognition (CVPR)*, 2016. 137, 170

[16] Aner Ben-Artzi, Ryan Overbeck, and Ravi Ramamoorthi. Real-time BRDF editing in complex lighting. In *SIGGRAPH Conf. Proc.*, 2006. 29

[17] Sai Bi, Xiaoguang Han, and Yizhou Yu. An l1 image transform for edge-preserving smoothing and scene-level intrinsic decomposition. *SIGGRAPH Conf. Proc.*, 2015. 111, 169

[18] Mike Bostock. D3. `http://d3js.org/`, 2013. [Online; accessed 24-Mar-2014]. 82

[19] Adrien Bousseau, Sylvain Paris, and Fredo Durand. User assisted intrinsic images. In *SIGGRAPH Asia Conf. Proc.*, 2009. 75

[20] Ivaylo Boyadzhiev, Sylvain Paris, and Kavita Bala. User-assisted image compositing for photographic lighting. *ACM Trans. Graph.*, 32(4):36:1–36:12, July 2013. 88

[21] David H. Brainard, Wendy Brunt, and Jon Speigle. Color constancy in the nearly natural image. *J. of the Optical Society of America*, 14(9), 1997. 19

[22] Steve Branson, Catherine Wah, Boris Babenko, Florian Schroff, Peter Welinder, Pietro Perona, and Serge Belongie. Visual recognition with humans in the loop. In *Proc. European Conference on Computer Vision*, 2010. 75, 81

[23] Wonmin Byeon, Thomas M. Breuel, Federico Raue, and Marcus Liwicki. Scene labeling with LSTM recurrent neural networks. In *CVPR*, 2015. 114, 116

[24] Barbara Caputo, Eric Hayman, and P. Mallikarjuna. Class-specific material categorisation. In *ICCV*, pages 1597–1604, 2005. 51

[25] Robert Carroll, Ravi Ramamoorthi, and Maneesh Agrawala. Illumination decomposition for material recoloring with consistent interreflections. *ACM Trans. on Graphics (SIGGRAPH)*, 2011. 75

[26] CGAL, Computational Geometry Algorithms Library. http://www.cgal.org/. 21

[27] K. Chatfield, K. Simonyan, A. Vedaldi, and A. Zisserman. Return of the devil in the details: Delving deep into convolutional nets. In *BMVC*, 2014. 114, 142

[28] Gal Chechik, Varun Sharma, Uri Shalit, and Samy Bengio. Large scale online learning of image similarity through ranking. *JMLR*, 2010. 141

[29] Kang Chen, Kun Xu1, Yizhou Yu, Tian-Yi Wang, and Shi-Min Hu. Magic decorator: Automatic material suggestion for indoor digital scenes. In *SIGGRAPH Asia Conf. Proc.*, 2015. 41, 168

[30] Liang-Chieh Chen, George Papandreou, Iasonas Kokkinos, Kevin Murphy, and Alan L Yuille. Semantic image segmentation with deep convolutional nets and fully connected crfs. In *ICLR*, 2015. 50

[31] Qifeng Chen and Vladlen Koltun. A simple model for intrinsic image decomposition with depth cues. In *Proc. International Conference on Computer Vision*, 2013. 75, 76

[32] Xiaobai Chen, Aleksey Golovinskiy, and Thomas Funkhouser. A benchmark for 3D mesh segmentation. In *SIGGRAPH Conf. Proc.*, 2009. 11

[33] K. Cho, B. van Merrienboer, D. Bahdanau, and Y. Bengio. On the properties of neural machine translation: Encoder-decoder approaches. *arXiv preprint arXiv:1409.1259*, 2014. 119

[34] Sumit Chopra, Raia Hadsell, and Yann LeCun. Learning a similarity metric discriminatively, with application to face verification. In *CVPR*. IEEE Press, 2005. 146

[35] Mircea Cimpoi, Subhransu Maji, Iasonas Kokkinos, Sammy Mohamed,

and Andrea Vedaldi. Describing textures in the wild. In *CVPR*, pages 3606–3613. IEEE, 2014. 51, 52, 68, 69

[36] Mircea Cimpoi, Subhransu Maji, Iasonas Kokkinos, and Andrea Vedaldi. Deep filter banks for texture recognition, description, and segmentation. *IJCV*, 2016. 41, 168

[37] Mircea Cimpoi, Subhransu Maji, and Andrea Vedaldi. Deep filter banks for texture recognition and segmentation. In *CVPR*, 2015. 40, 41, 168

[38] Forrester Cole, Kevin Sanik, Doug DeCarlo, Adam Finkelstein, Thomas Funkhouser, Szymon Rusinkiewicz, and Manish Singh. How well do line drawings depict shape? In *SIGGRAPH Conf. Proc.*, 2009. 11, 26, 75

[39] K.J. Dana, B. Van-Ginneken, S.K. Nayar, and J.J. Koenderink. Reflectance and texture of real world surfaces. *ACM Transactions on Graphics*, 18(1), 1999. 12

[40] Kristin J Dana, Bram Van Ginneken, Shree K Nayar, and Jan J Koenderink. Reflectance and texture of real-world surfaces. *ACM Transactions on Graphics (TOG)*, 18(1):1–34, 1999. 51

[41] A. P. Dawid and A. M. Skene. Maximum likelihood estimation of observer error-rates using the EM algorithm. In *J. Roy. Statistical Society*, 1979. 75

[42] Paul Debevec. Rendering synthetic objects into real scenes: bridging traditional and image-based graphics with global illumination and high dynamic range photography. In *SIGGRAPH Conf. Proc.*, 1998. 27, 39

[43] J. Deng, W. Dong, R. Socher, L.-J. Li, K. Li, and L. Fei-Fei. ImageNet: A large-scale hierarchical image database. In *Proc. Comp. Vision and Pattern Recognition*, 2009. 7, 10, 19

[44] Shouhong Ding, Bin Sheng, Zhifeng Xie, and Lizhuang Ma. Intrinsic image estimation using near-l0 sparse optimization. 111, 169

[45] S.K. Divvala, D. Hoiem, J.H. Hays, A.A. Efros, and M. Hebert. An empirical study of context in object detection. In *CVPR*, 2009. 113

[46] R.O. Dror, E. H. Adelson, and A. Willsky. Estimating surface reflectance properties from images under unknown illumination. In *Proc. SPIE Human Vision and Electronic Imaging*, 2001. 14, 41

[47] Ian Endres, Ali Farhadi, Derek Hoiem, and David Forsyth. The benefits and challenges of collecting richer object annotations. In *Workshop on Advancing Computer Vision with Humans in the Loop*, 2010. 11

[48] M. Everingham, L. Van Gool, C. K. I. Williams, J. Winn, and A. Zisserman. The PASCAL Visual Object Classes (VOC) Challenge. *IJCV*, 2010. 114, 122

[49] M. Everingham, L. Van Gool, C. K. I. Williams, J. Winn, and A. Zisserman. The Pascal Visual Object Classes (VOC) Challenge. *IJCV*, 88(2):303–338, June 2010. 54

[50] Clément Farabet, Camille Couprie, Laurent Najman, and Yann LeCun. Learning hierarchical features for scene labeling. *PAMI*, 35(8):1915–1929, 2013. 52

[51] Pedro Felzenszwalb, David McAllester, and Deva Ramanan. A discriminatively trained, multiscale, deformable part model. In *Proc. Computer Vision and Pattern Recognition*, 2008. 86

[52] Chen Feng, Fei Deng, and Vineet R. Kamat. Semi-automatic 3D reconstruction of piecewise planar building models from single image. In *Int. Conf. on Construction Appl. of Virtual Reality*, 2010. 26

[53] Roland W. Fleming, Ron O. Dror, and Edward H. Adelson. Real-world illumination and the perception of surface reflectance properties. *J. of Vision*, 3(5), 2003. 14, 33

[54] Roland W. Fleming, Antonio Torralba, and Edward H. Adelson. Specular reflections and the perception of shape. *Journal of Vision*, 4(9):798–820, 2004. 27

[55] Raghudeep Gadde, Varun Jampani, Martin Kiefel, Daniel Kappler, and Peter Gehler. Superpixel convolutional networks using bilateral inceptions. In *ECCV*, 2016. 70, 169

[56] Elena Garces, Aseem Agarwala, Diego Gutierrez, and Aaron Hertzmann. A similarity measure for illustration style. *ACM Trans. Graph.*, 33(4), July 2014. 141

[57] Elena Garces, Adolfo Munoz, Jorge Lopez-Moreno, and Diego Gutierrez. Intrinsic images by clustering. *Computer Graphics Forum (Eurographics Symposium on Rendering)*, 31(4), 2012. 74, 91, 92, 100, 104, 105, 106

[58] P. Gehler, C. Rother, M. Kiefel, L. Zhang, and B. Scholkopf. Recovering intrinsic images with a global sparsity prior on reflectance. In *NIPS*, 2011. 74, 91, 105

[59] David Geisler-Moroder and Arne Dür. A new Ward BRDF model with bounded albedo. In *Proc. Eurographics Symp. on Rendering*, 2010. 28

[60] Spyros Gidaris and Nikos Komodakis. Object detection via a multi-region & semantic segmentation-aware CNN model. In *ICCV*, 2015. xi, 112, 123, 124, 125, 127, 129

[61] Yotam Gingold, Ariel Shamir, and Daniel Cohen-Or. Micro perceptual human computation. *ACM Transactions on Graphics*, 31(5), 2012. 11, 36

[62] Yotam Gingold, Ariel Shamir, and Daniel Cohen-Or. Micro perceptual human computation. *ACM Trans. on Graphics*, 31(5), 2012. 75, 84

[63] Yotam Gingold, Ariel Shamir, and Daniel Cohen-Or. Micro perceptual human computation. *TOG*, 31(5), 2012. 151

[64] Bernd Girod, Vijay Chandrasekhar, David M. Chen, Ngai-Man Cheung, Radek Grzeszczuk, Yuriy Reznik, Gabriel Takacs, Sam S. Tsai, and Ramakrishna Vedantham. Mobile visual search, 2011. 142

[65] Ross Girshick. Fast R-CNN. In *ICCV*, 2015. xi, xvi, 112, 113, 115, 122, 123, 124, 125, 126, 129, 131

[66] Ross Girshick, Jeff Donahue, Trevor Darrell, and Jitendra Malik. Rich feature hierarchies for accurate object detection and semantic segmentation. In *CVPR*, 2014. 52, 114, 115

[67] S. Gould, R. Fulton, and D. Koller. Decomposing a scene into geometric and semantically consistent regions. In *Proceedings of the International Conference on Computer Vision (ICCV)*, 2009. 54

[68] Alex Graves and Jürgen Schmidhuber. Offline handwriting recognition with multidimensional recurrent neural networks. In *NIPS*, 2009. 114, 116

[69] Roger Grosse, Micah K. Johnson, Edward H. Adelson, and William T. Freeman. Ground truth dataset and baseline evaluations for intrinsic image algorithms. In *Proc. International Conference on Computer Vision*, 2009. 72, 74, 75, 104, 106, 108

[70] Tom Haber, Christian Fuchs, Philippe Bekaer, H-P Seidel, Michael Goesele, and Hendrik PA Lensch. Relighting objects from image collections. In *CVPR*, 2009. 75

[71] Raia Hadsell, Sumit Chopra, and Yann LeCun. Dimensionality reduction by learning an invariant mapping. In *CVPR*. IEEE Press, 2006. 144, 145, 146

[72] Bharath Hariharan, Pablo Arbelaez, Lubomir Bourdev, Subhransu Maji, and Jitendra Malik. Semantic contours from inverse detectors. In *ICCV*, 2011. xi, 123, 124

[73] Bharath Hariharan, Pablo Arbeláez, Ross Girshick, and Jitendra Malik. Hypercolumns for object segmentation and fine-grained localization. In *CVPR*, 2015. 112, 114, 116

[74] Daniel Hauagge, Scott Wehrwein, Kavita Bala, and Noah Snavely. Photometric ambient occlusion. *CVPR*, 2013. 75

[75] Eric Hayman, Barbara Caputo, Mario Fritz, and Jan olof Eklundh. On the significance of real-world conditions for material classification. In *ECCV*, 2004. 51

[76] James Hays and Alexei A Efros. Scene completion using millions of photographs. In *SIGGRAPH Conf. Proc.*, pages 4:1–4:7, 2007. 9

[77] Kaiming He, Xiangyu Zhang, Shaoqing Ren, and Jian Sun. Spatial pyramid pooling in deep convolutional networks for visual recognition. In *ECCV*, 2014. 114, 115

[78] S. Hochreiter and J. Schmidhuber. Long short-term memory. *Neural Computation*, 1997. 119

[79] Derek Hoiem, Yodsawalai Chodpathumwan, and Qieyun Dai. Diagnosing error in object detectors. In *ECCV*, 2012. xvi, 127, 130

[80] Jan Hendrik Hosang, Rodrigo Benenson, Piotr Dollár, and Bernt Schiele. What makes for effective detection proposals? *arXiv preprint arXiv:1502.05082*, 2015. 114, 126

[81] Diane Hu, Liefeng Bo, and Xiaofeng Ren. Toward robust material recog-

nition for everyday objects. In *Proc. British Machine Vision Conf.*, 2011. 11

[82] Diane Hu, Liefeng Bo, and Xiaofeng Ren. Toward robust material recognition for everyday objects. In *BMVC*, pages 1–11. Citeseer, 2011. 48, 51, 52, 69

[83] Varun Jampani, Martin Kiefel, and Peter V. Gehler. Learning sparse high dimensional filters: Image filtering, dense crfs and bilateral neural networks. In *CVPR*, 2016. 70, 169

[84] H. Jegou, F. Perronnin, M. Douze, J. Sanchez, P. Perez, and C. Schmid. Aggregating local image descriptors into compact codes. *PAMI*, 34(9), 2012. 142

[85] Yangqing Jia, Evan Shelhamer, Jeff Donahue, Sergey Karayev, Jonathan Long, Ross Girshick, Sergio Guadarrama, and Trevor Darrell. Caffe: Convolutional architecture for fast feature embedding. *arXiv:1408.5093*, 2014. 62, 144, 145, 155

[86] Yangqing Jia, Evan Shelhamer, Jeff Donahue, Sergey Karayev, Jonathan Long, Ross Girshick, Sergio Guadarrama, and Trevor Darrell. Caffe: Convolutional architecture for fast feature embedding. *arXiv preprint arXiv:1408.5093*, 2014. 122

[87] J.A. Juracek. *Surfaces: Visual Research for Artists and Designers*. Norton, 1996. 23

[88] Sergey Karayev, Matthew Trentacoste, Helen Han, Aseem Agarwala, Trevor Darrell, Aaron Hertzmann, and Holger Winnemoeller. Recognizing image style. In *BMVC*, 2014. 143

[89] Andrej Karpathy, Justin Johnson, and Fei-Fei Li. Visualizing and understanding recurrent networks. *arXiv preprint arXiv:1506.02078*, 2015. 136

[90] Kevin Karsch, Varsha Hedau, David Forsyth, and Derek Hoiem. Rendering synthetic objects into legacy photographs. In *SIGGRAPH Asia Conf. Proc.*, 2011. 27, 39

[91] W. B. Kerr and F. Pellacini. Toward evaluating material design interface paradigms for novice users. *ACM Transactions on Graphics*, 29(4), 2010. 28, 29

[92] J. J. Koenderink and A. J. van Doorn. Representation of local geometry in the visual system. *Bio. cybernetics*, 1987. 112

[93] Jan J. Koenderink, Andrea J. Van Doorn, and Astrid M. L. Kappers. Surface perception in pictures. *Perception & Psychophysics*, 1992. 26

[94] Tao Kong, Anbang Yao, Yurong Chen, and Fuchun Sun. HyperNet: towards accurate region proposal generation and joint object detection. In *CVPR*, 2016. 124

[95] Adriana Kovashka, Devi Parikh, and Kristen Grauman. Whittlesearch: Image search with relative attribute feedback. In *CVPR*, 2012. 141

[96] Philipp Krähenbühl and Vladlen Koltun. Efficient inference in fully connected CRFs with gaussian edge potentials. In *Neural Information Processing Systems*, 2011. 91, 94

[97] Philipp Krähenbühl and Vladlen Koltun. Parameter learning and convergent inference for dense random fields. In *Proceedings of the 30th International Conference on Machine Learning (ICML-13)*, pages 513–521, 2013. 49, 58, 60

[98] Philipp Krähenbühl and Vladlen Koltun. Parameter learning and convergent inference for dense random fields. In *Proc. International Conference on Machine Learning*, 2013. 70, 73, 91, 94, 99, 169

[99] Alex Krizhevsky, Ilya Sutskever, and Geoffrey E Hinton. Imagenet classification with deep convolutional neural networks. In *NIPS*, 2012. xvii, 52, 59, 61, 62, 68, 114, 115, 140, 141, 142, 143, 145, 148

[100] Brian Kulis. Metric learning: A survey. *Foundations and Trends in Machine Learning*, 5(4), 2012. 141

[101] P. Laffont, A. Bousseau, and G. Drettakis. Rich intrinsic image decomposition of outdoor scenes from multiple views. *IEEE Trans. on Visualization and Computer Graphics*, 19(2), 2013. 75

[102] Pierre-Yves Laffont, Adrien Bousseau, Sylvain Paris, Frédo Durand, and George Drettakis. Coherent intrinsic images from photo collections. *ACM Trans. Graph.*, 31(6), 2012. 75

[103] Jean-François Lalonde, Derek Hoiem, Alexei A. Efros, Carsten Rother, John

Winn, and Antonio Criminisi. Photo clip art. In *SIGGRAPH Conf. Proc.*, 2007. 9, 39

[104] Edwin H. Land and John J. McCann. Lightness and retinex theory. *J. Opt. Soc. Am.*, 61(1), 1971. 71, 74, 90

[105] Quoc V. Le, Navdeep Jaitly, and Geoffrey E. Hinton. A simple way to initialize recurrent networks of rectified linear units. *arXiv preprint arXiv:1504.00941*, 2015. xvi, 117, 119

[106] Yann LeCun, Bernhard Boser, John S Denker, Donnie Henderson, Richard E Howard, Wayne Hubbard, and Lawrence D Jackel. Backpropagation applied to handwritten zip code recognition. *Neural computation*, 1(4), 1989. 52, 142

[107] Thomas Leung and Jitendra Malik. Representing and recognizing the visual appearance of materials using three-dimensional textons. *IJCV*, 43(1):29–44, June 2001. 51

[108] Wenbin Li and Mario Fritz. Recognizing materials from virtual examples. In *Computer Vision–ECCV 2012*, pages 345–358. Springer, 2012. 51

[109] Yangyan Li, Hao Su1, Charles R. Qi, Noa Fish, Daniel Cohen-Or, and Leonidas J. Guibas. Joint embeddings of shapes and images via cnn image purification. *SIGGRAPH Asia Conf. Proc.*, 2015. 166, 170

[110] Zicheng Liao, Jason Rock, Yang Wang, and David Forsyth. Non-parametric filtering for geometric detail extraction and material representation. In *Proc. Computer Vision and Pattern Recognition*, 2013. 74, 90

[111] Tsung-Yi Lin, Michael Maire, Serge Belongie, James Hays, Pietro Perona, Deva Ramanan, Piotr Dollár, and C. Lawrence Zitnick. Microsoft COCO: common objects in context. *ECCV*, 2014. 149

[112] Tsung-Yi Lin, Michael Maire, Serge Belongie, James Hays, Pietro Perona, Deva Ramanan, Piotr Dollr, and C. Lawrence Zitnick. Microsoft coco: Common objects in context. In *European Conference on Computer Vision*, 2014. 114, 122

[113] Tsung-Yi Lin, Michael Maire, Serge J. Belongie, Lubomir D. Bourdev, Ross B. Girshick, James Hays, Pietro Perona, Deva Ramanan, Piotr Dollár,

and C. Lawrence Zitnick. Microsoft COCO: common objects in context. *arXiv:1412.6574*, 2014. 41, 169

[114] Ce Liu, L. Sharan, E.H. Adelson, and R. Rosenholtz. Exploring features in a Bayesian framework for material recognition. In *Proc. Comp. Vision and Pattern Recognition*, 2010. 11, 14, 41

[115] Ce Liu, Lavanya Sharan, Edward H Adelson, and Ruth Rosenholtz. Exploring features in a bayesian framework for material recognition. In *Computer Vision and Pattern Recognition (CVPR), 2010 IEEE Conference on*, pages 239–246. IEEE, 2010. 48, 51

[116] Wei Liu, Andrew Rabinovich, and Alexander C. Berg. ParseNet: Looking wider to see better. *arXiv e-prints*, arXiv:1506.04579 [cs.CV], 2015. 112, 114, 116, 132, 134

[117] Xiaopei Liu, Lei Jiang, Tien-Tsin Wong, and Chi-Wing Fu. Statistical invariance for texture synthesis. *Visualization and Computer Graphics, IEEE Transactions on*, 2012. 74

[118] Yanxi Liu, Wen-Chieh Lin, and James Hays. Near regular texture analysis and manipulation. In *SIGGRAPH Conf. Proc.*, 2004. 11

[119] Jonathan Long, Evan Shelhamer, and Trevor Darrell. Fully convolutional networks for semantic segmentation. In *CVPR*, 2015. 112, 114, 116, 120

[120] Matthew Marge, Satanjeev Banerjee, and Alexander I. Rudnicky. Using the Amazon Mechanical Turk for transcription of spoken language. In *Int. Conf. on Acoustics, Speech, and Signal Processing*, 2010. 36

[121] Wojciech Matusik, Hanspeter Pfister, Matt Brand, and Leonard McMillan. A data-driven reflectance model. *ACM Transactions on Graphics*, 22(3), 2003. 12

[122] Marius Muja and David G. Lowe. Scalable nearest neighbor algorithms for high dimensional data. *PAMI*, 2014. 164

[123] Takuya Narihira, Michael Maire, and Stella X. Yu. Learning lightness from human judgement on relative reflectance. In *CVPR*, 2015. 111, 169

[124] Addy Ngan, Frédo Durand, and Wojciech Matusik. Experimental analysis

of brdf models. In *Proceedings of the Sixteenth Eurographics conference on Rendering Techniques*, EGSR'05, 2005. 12

[125] Peter O'Donovan, Jānis Lībeks, Aseem Agarwala, and Aaron Hertzmann. Exploratory font selection using crowdsourced attributes. *ACM Trans. Graph.*, 33(4), 2014. 141

[126] Byong Mok Oh, Max Chen, Julie Dorsey, and Frédo Durand. Image-based modeling and photo editing. In *Proceedings of the 28th annual conference on Computer graphics and interactive techniques*, SIGGRAPH '01, 2001. 74

[127] Aude Oliva and Antonio Torralba. Modeling the shape of the scene: a holistic representation of the spatial envelope. In *IJCV*, 2001. 114

[128] I. Omer and M. Werman. Color lines: image specific color representation. In *CVPR*, 2004. 74, 91, 93

[129] M. Oquab, L. Bottou, I. Laptev, and J. Sivic. Learning and transferring mid-level image representations using convolutional neural networks. In *CVPR*, 2014. 52

[130] V. Ordonez, V. Jagadeesh, Wei Di, A. Bhardwaj, and R. Piramuthu. Furniture-geek: Understanding fine-grained furniture attributes from freely associated text and tags. In *WACV*, pages 317–324, March 2014. 142

[131] Yuri Ostrovsky, Patrick Cavanagh, and Pawan Sinha. Perceiving illumination inconsistencies in scenes. *Perception*, 34(11):1301–1314, 2005. 77

[132] Devi Parikh and Kristen Grauman. Relative attributes. In *ICCV*, pages 503–510, 2011. 141

[133] Devi Parikh, C. Lawrence Zitnick, and Tsuhan Chen. Exploring tiny images: The roles of appearance and contextual information for machine and human object recognition. *PAMI*, 2011. 113

[134] Genevieve Patterson, Chen Xu, Hang Su, and James Hays. The SUN Attribute Database: Beyond Categories for Deeper Scene Understanding. *IJCV*, 108(1-2):59–81, 2014. 47

[135] Fabio Pellacini, James A. Ferwerda, and Donald P. Greenberg. Toward

a psychophysically-based light reflection model for image synthesis. In *SIGGRAPH Conf. Proc.*, 2000. 28

[136] F. Perronnin and C. Dance. Fisher kernels on visual vocabularies for image categorization. In *CVPR*, June 2007. 142

[137] Pedro O. Pinheiro, Ronan Collobert, and Piotr Dollár. Learning to segment object candidates. In *NIPS*, 2015. 130

[138] J. Pont-Tuset, P. Arbeláez, J. Barron, F. Marques, and J. Malik. Multiscale combinatorial grouping for image segmentation and object proposal generation. In *arXiv:1503.00848*, March 2015. xi, 125

[139] Xianbiao Qi, Rong Xiao, Jun Guo, and Lei Zhang. Pairwise rotation invariant co-occurrence local binary pattern. In *Computer Vision–ECCV 2012*, pages 158–171. Springer, 2012. 48, 51

[140] G. Ramanarayanan, J. Ferwerda, B. Walter, and K. Bala. Visual equivalence: Towards a new standard for image fidelity. In *SIGGRAPH Conf. Proc.*, New York, NY, USA, 2007. 27

[141] Ali Sharif Razavian, Hossein Azizpour, Josephine Sullivan, and Stefan Carlsson. CNN features off-the-shelf: an astounding baseline for recognition. *Deep Vision (CVPR Workshop)*, 2014. 155

[142] Ali Sharif Razavian, Josephine Sullivan, Atsuto Maki, and Stefan Carlsson. Visual instance retrieval with deep convolutional networks. *arXiv:1412.6574*, 2014. 143, 146, 162

[143] Joseph Redmon, Santosh Divvala, Ross Girshick, and Ali Farhadi. You only look once: Unified, real-time object detection. *arXiv preprint arXiv:1506.02640*, 2015. 124

[144] Erik Reinhard, Michael Stark, Peter Shirley, and James Ferwerda. Photographic tone reproduction for digital images. In *SIGGRAPH Conf. Proc.*, 2002. 29

[145] Peiran Ren, Jiaping Wang, John Snyder, Xin Tong, and Baining Guo. Pocket reflectometry. In *SIGGRAPH Conf. Proc.*, 2011. 12

[146] Shaoqing Ren, Kaiming He, Ross Girshick, and Jian Sun. Faster R-CNN:

Towards real-time object detection with region proposal networks. In *NIPS*, 2015. xi, 112, 118, 123, 124, 125

[147] Fabiano Romeiro and Todd Zickler. Blind reflectometry. In *Proc. European Conf. on Comp. Vision*, 2010. 9, 14

[148] Michael Rubinstein, Diego Gutierrez, Olga Sorkine, and Ariel Shamir. A comparative study of image retargeting. In *SIGGRAPH Asia Conf. Proc.*, 2010. 11, 75

[149] David E Rumelhart, Geoffrey E Hinton, and Ronald J Williams. Learning internal representations by error-propagation. *Parallel Distributed Processing*, 1, 1986. 145

[150] Olga Russakovsky, Jia Deng, Hao Su, Jonathan Krause, Sanjeev Satheesh, Sean Ma, Zhiheng Huang, Andrej Karpathy, Aditya Khosla, Michael Bernstein, Alexander C. Berg, and Li Fei-Fei. ImageNet Large Scale Visual Recognition Challenge, 2014. 47, 52

[151] Olga Russakovsky, Jia Deng, Hao Su, Jonathan Krause, Sanjeev Satheesh, Sean Ma, Zhiheng Huang, Andrej Karpathy, Aditya Khosla, Michael Bernstein, Alexander C. Berg, and Li Fei-Fei. ImageNet Large Scale Visual Recognition Challenge. *arXiv preprint arXiv:1409.0575*, 2014. 122

[152] Bryan C. Russell, Antonio Torralba, Kevin P. Murphy, and William T. Freeman. LabelMe: A database and web-based tool for image annotation. *Int. J. of Computer Vision*, 77(1-3), 2008. 7, 9, 10, 14, 23

[153] Bryan C. Russell, Antonio Torralba, Kevin P. Murphy, and William T. Freeman. LabelMe: A database and web-based tool for image annotation. *IJCV*, 77(1-3):157–173, May 2008. 54

[154] Patsorn Sangkloy, Nathan Burnell, Cusuh Ham, and James Hays. The sketchy database: Learning to retrieve badly drawn bunnies. *SIGGRAPH Conf. Proc.*, 2016. 166, 170

[155] M. Schuster and K. K. Paliwal. Bidirectional recurrent neural networks. *IEEE Transactions on Signal Processing*, 1997. 116

[156] Gabriel Schwartz and Ko Nishino. Visual material traits: Recognizing per-pixel material context. In *Proceedings of the International Conference on Computer Vision Workshops (ICCVW)*, pages 883–890. IEEE, 2013. 52

[157] Pierre Sermanet, David Eigen, Xiang Zhang, Michaël Mathieu, Rob Fergus, and Yann LeCun. Overfeat: Integrated recognition, localization and detection using convolutional networks. *arXiv*, 2013. 49, 52, 60, 115

[158] Pierre Sermanet, Koray Kavukcuoglu, Soumith Chintala, and Yann LeCun. Pedestrian detection with unsupervised multi-stage feature learning. In *CVPR*, 2013. 112, 114, 115, 116

[159] Lavanya Sharan, Ce Liu, Ruth Rosenholtz, and Edward Adelson. Recognizing materials using perceptually inspired features. *IJCV*, 2013. 48, 68

[160] Lavanya Sharan, Ruth Rosenholtz, and Edward Adelson. Material perception: What can you see in a brief glance? *Journal of Vision*, 9(8):784–784, 2009. 48, 51, 70, 169

[161] Lavanya Sharan, Ruth Rosenholtz, and Edward H. Adelson. Material perception: What can you see in a brief glance? *J. of Vision*, 9(8), 2009. 20

[162] Jianbing Shen, Xiaoshan Yang, Yunde Jia, and Xuelong Li. Intrinsic images using optimization. In *Proc. Computer Vision and Pattern Recognition*, 2011. 104, 105, 107

[163] Li Shen, Ping Tan, and S. Lin. Intrinsic image decomposition with non-local texture cues. In *CVPR*, 2008. 74

[164] Li Shen and Chuohao Yeo. Intrinsic images decomposition using a local and global sparse representation of reflectance. In *CVPR*, 2011. 74, 91

[165] Karen Simonyan and Andrew Zisserman. Very deep convolutional networks for large-scale image recognition. *arXiv*, 2014. 52, 61, 62

[166] Karen Simonyan and Andrew Zisserman. Very deep convolutional networks for large-scale image recognition. In *ICLR*, 2015. xvi, 112, 113, 118, 122

[167] Christian Szegedy, Wei Liu, Yangqing Jia, Pierre Sermanet, Scott Reed, Dragomir Anguelov, Dumitru Erhan, Vincent Vanhoucke, and Andrew Rabinovich. Going deeper with convolutions. *CVPR*, 2015. xvii, 52, 61, 62, 140, 141, 143, 159

[168] Yaniv Taigman, Ming Yang, Marc Aurelio Ranzato, and Lior Wolf. Deepface: Closing the gap to human-level performance in face verification. In *CVPR*, 2014. 143

[169] Marshall F. Tappen, Edward H. Adelson, and William T. Freeman. Estimating intrinsic component images using non-linear regression. In *Proc. Comp. Vision and Pattern Recognition*, pages 1992–1999, 2006. 74

[170] M.F. Tappen, W.T. Freeman, and E.H. Adelson. Recovering intrinsic images from a single image. *Pattern Analysis and Machine Intelligence, IEEE Transactions on*, 2005. 74

[171] Jean-Philippe Tardif. Non-iterative approach for fast and accurate vanishing point detection. In *Proc. Int. Conf. on Comp. Vision*, 2009. 26

[172] Understanding the difficulty of training deep feedforward neural networks. Xavier glorot and yoshua bengio. In *AISTATS*, 2010. 119

[173] Radu Timofte and Luc J Van Gool. A training-free classification framework for textures, writers, and materials. In *BMVC*, pages 1–12, 2012. 51

[174] Roberto Toldo and Andrea Fusiello. Robust multiple structures estimation with J-linkage. In *Proc. European Conf. on Comp. Vision*, 2008. 26

[175] Antonio Torralba. Contextual priming for object detection. *IJCV*, 2003. 113

[176] Antonio Torralba, Rob Fergus, and William T. Freeman. 80 million tiny images: A large data set for nonparametric object and scene recognition. *Trans. on Pattern Analysis and Machine Intelligence*, 30(11), 2008. 7, 10

[177] J. Uijlings, K. van de Sande, T. Gevers, and A. Smeulders. Selective search for object recognition. *IJCV*, 2013. xi, 114, 123, 124, 125, 128, 130

[178] R. Vaillant, C. Monrocq, and Y. LeCun. Original approach for the localisation of objects in images. *IEE Proc. on Vision, Image, and Signal Processing*, 1994. 115

[179] L. Van Der Maaten and G Hinton. Visualizing data using t-SNE. In *Journal of Machine Learning*, 2008. xviii, 155, 156

[180] Jarke J. van Wijk and Wim A.A. Nuij. Smooth and efficient zooming and

panning. In *Proc. IEEE Conference on Information Visualization (INFOVIS)*, 2003. 82

[181] P. Vangorp, J. Laurijssen, and P. Dutré. The influence of shape on the perception of material reflectance. *ACM Transactions on Graphics*, 26(3), 2007. 27, 33

[182] Manik Varma and Andrew Zisserman. A statistical approach to texture classification from single images. *IJCV*, 62(1-2):61–81, April 2005. 51

[183] Andreas Veit, Balazs Kovacs, Sean Bell, Julian McAuley, Kavita Bala, and Serge Belongie. Learning visual clothing style with heterogeneous dyadic co-occurrences. In *The IEEE International Conference on Computer Vision (ICCV)*, December 2015. 166, 170

[184] Francesco Visin, Kyle Kastner, Kyunghyun Cho, Matteo Matteucci, Aaron Courville, and Yoshua Bengio. ReNet: A recurrent neural network based alternative to convolutional networks. *arXiv e-prints*, arXiv:1505.00393 [cs.CV], 2015. 114, 116, 136

[185] Rafael Grompone von Gioi, Jeremie Jakubowicz, Jean-Michel Morel, and Gregory Randall. LSD: A fast line segment detector with a false detection control. *Trans. on Pattern Analysis and Machine Intelligence*, 32(4), 2010. 26

[186] Bruce Walter, Pramook Khungurn, and Kavita Bala. Bidirectional lightcuts. In *SIGGRAPH Conf. Proc.*, 2012. 33

[187] Jiang Wang, Yang Song, Thomas Leung, Chuck Rosenberg, Jingbin Wang, James Philbin, Bo Chen, and Ying Wu. Learning fine-grained image similarity with deep ranking. In *CVPR*, 2014. 143, 146

[188] G.J. Ward. Measuring and modeling anisotropic reflection. In *SIGGRAPH Conf. Proc.*, 1992. 28

[189] Y. Weiss. Deriving intrinsic images from image sequences. In *ICCV*, 2001. 75

[190] P. Welinder, S. Branson, S. Belongie, and P. Perona. The multidimensional wisdom of crowds. In *NIPS*, 2010. 75, 83, 84

[191] Peter Welinder, Steve Branson, Serge Belongie, and Pietro Perona. The

multidimensional wisdom of crowds. In *Proc. Neural Information Processing Systems*, 2010. 15

[192] Jason Weston, Frederic Ratle, and Ronan Collobert. Deep learning via semi-supervised embedding. In *ICML*, 2008. 146

[193] Tim Weyrich, Jason Lawrence, Hendrik P. A. Lensch, Szymon Rusinkiewicz, and Todd Zickler. Principles of appearance acquisition and representation. *Found. Trends. Comput. Graph. Vis.*, 4(2), 2009. 9, 11

[194] Jianxiong Xiao, Krista A. Ehinger, James Hays, Antonio Torralba, and Aude Oliva. SUN Database: Exploring a large collection of scene categories. *IJCV*, 2014. 47, 54

[195] Jianxiong Xiao, James Hays, Krista A. Ehinger, Aude Oliva, and Antonio Torralba. SUN database: Large-scale scene recognition from abbey to zoo. In *Proc. Comp. Vision and Pattern Recognition*, 2010. 7, 10, 13

[196] S. Zagoruyko, A. Lerer, T.-Y. Lin, P. Pinheiro, S. Gross, S. Chintala, and P. Dollár. A multipath network for object detection. 2016. 137, 170

[197] Matthew D Zeiler and Rob Fergus. Visualizing and understanding convolutional networks. In *Computer Vision–ECCV 2014*, pages 818–833. Springer, 2014. 52

[198] Yan Zhang, Mete Ozay, Xing Liu, and Takayuki Okatani. Integrating deep features for material recognition. *https://arxiv.org/abs/1511.06522*, 2015. 70, 169

[199] Qi Zhao, Ping Tan, Qiang Dai, Li Shen, Enhua Wu, and Stephen Lin. A closed-form solution to retinex with nonlocal texture constraints. *IEEE Trans. on Pattern Analysis and Machine Intelligence*, 34(7), 2012. 74, 91, 104, 105, 106

[200] Shuai Zheng, Ming-Ming Cheng, Jonathan Warrell, Paul Sturgess, Vibhav Vineet, Carsten Rother, and Philip HS Torr. Dense semantic image segmentation with objects and attributes. In *CVPR*, pages 3214–3221. IEEE, 2014. 52

[201] Shuai Zheng, Sadeep Jayasumana, Bernardino Romera-Paredes, Vibhav Vineet, Zhizhong Su adn Dalong Du, Chang Huang, and Philip

H. S. Torr. Conditional random fields as recurrent neural networks. *https://arxiv.org/abs/1502.03240*, 2015. 50

[202] B. Zhou, A. Lapedriza, J. Xiao, A. Torralba, and A. Oliva. Learning deep features for scene recognition using Places database. *NIPS*, 2014. 47, 54

[203] Tinghui Zhou, Philipp Krahenbuhl, and Alexei A. Efros. Learning data-driven reflectance priors for intrinsic image decomposition. In *ICCV*, 2015. 111, 169

[204] Chenchen Zhu, Yutong Zheng, Khoa Luu, and Marios Savvides. Cms-rcnn: Contextual multi-scale region-based cnn for unconstrained face detection. 2016. 137, 170

[205] C. Lawrence Zitnick and Piotr Dollár. Edge boxes: Locating object proposals from edges. In *ECCV*, 2014. xi, 114, 123, 124, 128

[206] Daniel Zoran, Phillip Isola, Dilip Krishnan, and William T. Freeman. Learning ordinal relationships for mid-level vision. In *ICCV*, 2015. 111, 169